UNIVERSIDAD SAN FRANCISCO DE QUITO USFQ

Colegio de Ciencias e Ingenierías

Broadband ferromagnetic resonance characterization for CoFeB, Py, YIG thin films and Py/YIG bilayer system

Proyecto de investigación

José Nicolás Solano Córdova

Licenciatura en Física

Trabajo de titulación presentado como requisito
para la obtención del título de Licenciado en Física

Quito, 20 de diciembre de 2017

UNIVERSIDAD SAN FRANCISCO DE QUITO USFQ

COLEGIO DE CIENCIAS E INGENIERÍAS

HOJA DE CALIFICACIÓN
DE TRABAJO DE TITULACIÓN

Broadband ferromagnetic resonance characterization for CoFeB, Py, YIG thin films and Py/YIG bilayer system

José Nicolás Solano Córdova

Calificación:

Nombre del profesor: Vincent Vlaminck Ph.D.

Firma del profesor: --

Quito, 20 de diciembre de 2017

DERECHOS DE AUTOR

Por medio del presente documento certifico que he leído todas las Políticas y Manuales de la Universidad San Francisco de Quito USFQ, incluyendo la Política de Propiedad Intelectual USFQ, y estoy de acuerdo con su contenido, por lo que los derechos de propiedad intelectual del presente trabajo quedan sujetos a lo dispuesto en esas Políticas.

Asimismo, autorizo a la USFQ para que realice la digitalización y publicación de este trabajo en el repositorio virtual, de conformidad a lo dispuesto en el Art. 144 de la Ley Orgánica de Educación Superior.

Firma del estudiante: ____

Nombres y apellidos: José Nicolás Solano Córdova

Código: 00117121

Cédula de identidad: 010550285-0

Lugar y fecha: Quito, 20 de diciembre de 2017

A mis padres y mi Cami.

Agradecimientos

Aquí agradezco a quienes han estado durante estos 4 años y que de una u otra forma han sido parte de este trabajo. Lo hago en español o inglés para mejor entendimiento de las partes involucradas. No hay un orden de importancia ni nada por el estilo. Ahora, eliminando los formalismos...

Gracias a mi pa y mi ma por haber estado a mi lado, desde Cuenca, todo este tiempo. Gracias a mi pa por haberme seguido en mi locura de estudiar física sin mucha protesta, lo cual me sorprendió de hecho. Gracias a mi ma, a pesar de creer que no fue la mejor decisión, siempre estuvo pendiente de mí. Gracias por estar estos años de U y por apoyarme para viajar y seguir aprendiendo aún más. A mis ñaños por seguirme recibiendo como su ñaño a pesar de que casi 5 años que no estoy en la casa. Hubiese querido no perderme tantas cosas. Perdón por no llamar tanto.

Gracias a la USFQ por haberme dado una beca para estudiar lo que me gusta. Especialmente gracias a Dario por haber creído en mí. Gracias a todos lo profes que me enseñaron tantas cosas. A pesar de las clases buenas y malas, pienso que en la U tanto mi conocimiento como mi manera de ver el mundo crecieron mucho. Gracias también por haberme dado un apoyo económico para viajar a Francia y realizar gran parte de esta tesis. Gracias a Carlos Montufar por encargarse personalmente de agilizar las formalidades para realizarlo.

I would like to thank Mr. Stefan Haacke, director of the IPCMS, for allowing me to do my internship in the institution and all the financial support I have received. I would like to specially thank Matthieu Bailleul for accepting me into his team for approximately two months despite my small experience and sharing with me some of his knowledge and nice personality. Also for having corrections and important input for this manuscript. I want also to thank Damien Louis for correcting my mistakes and sharing with me his scientific experience and Mathematica's tricks.

Gracias a todos los muchachos físicos por estos años de amistad y de compartir experiencias. Al Nico (ya no te digo nada mmv jaja), al Jotita (ratooonciiito), Robertin (yaaa bro, yaaa, mejor bielemos), Joelin (falso jaja), Karencilla (no me odies), Ericksin (que la Dany no te pegue bro), al Jorgito (que presenten a la Alegría), Pabliiito (no te odio bro, Mathematica <3), Felipe (ya no ande muchando en todo lado) y al resto de la tarea de h…s! Gracias a Joaqs por haberme dejado ayudarle en los labs y al Camilo (sol) por haberme acolado tanto en Strasbourg.

I would like to specially thank Vincent Vlaminck. Thanks for teaching me all I know about experimental physics, and for letting me work with you even though I did not have enough knowledge. Thanks for sharing with me your scientific and personal experience. Thanks for introducing me to the field of magnetism, specially FMR. It's been great getting to know you a bit more during this last months. Thanks for sharing your knowledge, all the patience and giving your input and corrections to this manuscript; I think it is in better shape now. Thanks for recommending me at the USFQ and IPCMS for my internship. THANKS A LOT FOR ALL THE SUPPORT!

Gracias Hermosa. Este año y medio (el 2 patitos de julio sí cuenta (Snoopy enojado)) de Madness ha sido la mejor época. Tú sabes todo lo que siento por ti, pero gracias por haber estado a mi lado especialmente estos últimos 6 meses. Gracias por estar ahí cada día mientras estaba en Francia y gracias por haber estado conmigo allá también siendo felices. Gracias por la paciencia y apoyarme para que pase tanto tiempo con ¨la otra¨ (la tesis), pero ya se acabó. No estoy seguro de cuentas ¨otras¨ vengan, pero quiero que estés ahí también apoyándome. Tú Zezé crack.

José Solano Quito, 2 de diciembre del 2017.

Resumen

Se realiza una caracterización por medio de resonancia ferromagnética (FMR) de banda amplia (1-50 GHz), dentro y fuera del plano en una película delgada de CoFeB, dos películas de $Y_3Fe_5O_{12}$ (YIG), una película de referencia de $Ni_{80}Fe_{20}$(Py) y en una bicapa de Py/YIG por medio de un analizador de redes vectorial (VNA). Usando esta técnica de banda amplia, se miden tanto el modo fundamental de precesión uniforme de la magnetización, como el primer modo estacionario de ondas de spin. Se lleva a cabo un estudio teórico completo de los dos modos de precesión de la magnetización. Como resultado se llega a una versión generalizada de la fórmula de Kittel para la relación de dispersión del modo fundamental y para modos estacionario de ondas de spin, con los cuales se obtienen constantes de anisotropía, constantes de intercambio y magnetización de saturación. Se realiza una descripción detallada del equipo experimental junto con las correcciones de microonda sobre las mediciones sin procesar con el objetivo de encontrar la suceptibilidad magnética efectiva. Las mediciones permitieron obtener las constantes de intercambio para la lámina de CoFeB, lo cual es de interés para investigaciones futuras en bicapas de Py/CoFeB. En el caso de las láminas de YIG, se obtuvo su caracterización parcial y se compararon sus parámetros de damping de Gilbert. Se obtuvo la caracterización completa para la lámina de referencia de Py. Esto finalmente fue contrastatdo con la bicapa de Py/YIG, donde se encontró que la interacción entre las capas lleva a la inesperada anulación del modo fundamental de YIG en la configuración en-el- plano, esto entre otras características que también son analizadas.

Key words: resonancia ferromagnetica, modos de onda de spin, bicapa ferromagnetica, YIG.

Abstract

A broadband ferromagnetic resonance (FMR) characterization (1-50 GHz), is conducted both in- and out-of-plane in a CoFeB film, two $Y_3Fe_5O_{12}$ (YIG) films, a $Ni_{80}Fe_{20}$(Py) reference film and in Py/YIG bilayer sample via vector network analyzer (VNA). With this broadband technique, both the fundamental uniform precession mode (FMR) of the magnetization and the first perpendicular standing spin wave mode (PSSW1) are measured. A complete theoretical study of the two precession modes of the magnetization is developed. This leads to a generalized version of Kittel's formula for the dispersion relation of the fundamental mode and for the perpendicular standing spin wave modes which allows to obtain anisotropy constants, exchange constant and saturation magnetization. A detailed description of the used setup is also given together with the microwave corrections to the raw measurements in order to extract the effective magnetic susceptibility. The measurements allowed to extract the exchange constant for the CoFeB film which is of interest for future investigations in Py/CoFeB bilayers. A partial characterization was obtained for the YIG films and their Gilbert damping parameters are compared. For the Py reference film a complete characterization was obtained. Finally this is contrasted with the Py/YIG bilayer where the interaction between the two layers leads to a surprising suppression of the fundamental mode of YIG in the in-plane configuration and other features that are discussed.

Key words: ferromagnetic resonance, spin wave modes, ferromagnetic bilayer, YIG.

Index

1 Introduction 13

2 Basic magnetization dynamics: Uniform precession 17

2.1 Magnetic energies 17
2.1.1 Zeeman energy 17
2.1.2 Exchange energy 17
2.1.3 Demagnetizing field energy 18
2.1.4 Anisotropy energy 19
2.2 Effective field 20
2.3 Equation of motion of the magnetization 20
2.4 Dynamic susceptibility without losses 21
2.5 Shape effects on resonance frequency 24
2.6 Introduction of bulk uniaxial anisotropy term in the Landau Lifshitz equation 26
2.7 Landau Lifshitz Gilbert equation and presence of losses 27

3 Standing spin wave modes: Non-uniform precession 29

3.1 Geometry and systems of coordinates 29
3.2 Variable magnetic field equation 29
3.3 Spin Wave Modes 33
3.4 General dispersion relation: Perturbation theory approach 35
3.5 Dispersion relations for uniform (FMR) and perpendicular standing spin wave modes 38

4 Vector network analyzer ferromagnetic resonance 41

4.1 Experimental set up 41
4.1.1 Microwave network 42
4.1.2 Magnet control 43
4.2 Preliminary VNA notions 43
4.2.1 Scattering parameters 44
4.2.2 Actual device 45
4.3 Two port data evaluation 45
4.3.1 Raw data 46
4.3.2 Sample's position correction 47
4.3.3 De embedding 48
4.3.4 Calculation of Γ and γ 48
4.3.5 Field shielding 49
4.3.6 Obtaining $\tilde{\varepsilon}_r$ and $\tilde{\mu}_r$ 49

5 Results and discussion **51**
5.1 CoFeB 40nm (5864) 51
5.1.1 Spectra 52
5.1.2 Dispersion relations and magnetic parameters 54
5.2 Permalloy 40 nm 55
5.2.1 Spectra 56
5.2.2 Dispersion relations and magnetic parameters 58
5.3 YIG 29nm 59
5.3.1 Spectra 60
5.3.2 Dispersion relations and magnetic parameters 64
5.4 YIG AL5007 64
5.4.1 Spectra 65
5.4.2 Dispersion relations and magnetic parameters 66
5.5 YIG/Py 67
5.5.1 Spectra 68
5.5.2 Dispersion relations and magnetic parameters 70
5.6 Linewidths 72

6 Conclusions **74**

Appendices **77**

7 References **88**

Figure Index

1 Precession of the magnetization around an equilibrium position with cone angle β 21
2 Linear approximation representation for LL equation 22
3 Field linear approximation configuration for a general ellipsoid 24
4 Relaxation process of the magnetization due to Damping 27
5 Calculated Susceptibility for typical values of Permalloy 28
6 Systems of coodinates of the sample and the magnetization related by θ and φ 30
7 Spin wave modes sketched across the film thickness 35
8 Setup's components representation 41
9 Brass box with waveguide board and connectors 42
10 Sample fixation: a) Using the podium (inserted in box), b) Fixating directly on the board 42
11 VNA connected to board for in-plane field configuration 43
12 2-port generic component 44
13 Board's division for microwave corrections 46
14 CoFeB: Resonance profiles for different frequencies in the in-plane configuration: a) FMR mode, b) PSSW1 52
15 CoFeB: FMR mode resonance profiles for different frequencies in the out-of-plane configuration 53
16 CoFeB: Fitted dispersion relations for FMR and PSSW1 modes in- and out-of-plane configurations 54
17 Py: Resonance profiles for different frequencies in the in-plane configuration: a) FMR mode, b) PSSW1 mode 56
18 Py: Resonance profiles for different frequencies in the out-of-plane configuration: a) FMR mode, b) PSSW1 mode 57
19 Py: Fitted dispersion relations for FMR and PSSW1 modes in in and out-of-plane configurations 58
20 YIG 29 nm: Resonance profiles for different frequencies in the in-plane configuration: a) FMR mode with sample oriented in a arbitrary direction (Orientation 1), b) FMR mode with sample rotated by 90^o in the plane (Orientation 2). 60
21 YIG 29 nm: Resonance profiles for different frequencies in the out-of-plane configuration: a) FMR mode with sample oriented in a arbitrary direction, b) FMR mode with sample rotated by 90^o in the plane. 62
22 YIG 29 nm: Progression of additional wide resonance attributed to GGG. 63
23 YIG 29 nm: Fitted dispersion relations for FMR mode in in and out-of-plane configurations 64

24 YIG AL5007: Progression of additional wide resonance attributed to GGG. 65
25 YIG AL5007: Progression of additional wide resonance attributed to GGG. 66
26 YIG AL5007: Fitted dispersion relations for FMR mode in in- and out-of-plane configurations 67
27 YIG/Py: Resonance profiles for the bilayer in the in-plane configuration. 68
28 YIG/Py: Resonance profiles for the bilayer in the out-of-plane configuration. 69
29 YIG/Py: Fitted dispersion relations for FMR mode in in- and out-of-plane configurations 71
30 Linewidths for in-plane configuration 72
31 Linewidths for out-of-plane configuration 73

1 Introduction

State of the art

A ferromagnetic material is characterized by a spontaneous magnetization caused by the alignment of the magnetic moments in the atomic lattice. The main reason for the ordering in ferromagnetic materials is the exchange interaction between neighboring spins that at the quantum scale can be modeled by the Heisenberg Hamiltonian $-\sum\limits_{ij} \Im_{ij} \hat{\vec{S}}_i \cdot \hat{\vec{S}}_j$. This energy tends to align the spins parallel to each other since the exchange integral $\Im_{ij}$ is positive. The magnetic moments align along preferred directions given by the structure of the lattice itself. A ferrimagnet has unequal oppositely directed sub-lattices which create an spontaneous magnetization.

Nowadays magnetic materials are of great importance in technological applications. More specifically, the field of spintronics, which uses the spin dependent transport properties of ferromagnetic materials, have allowed to expand capacities and speed for information processing. This is contrasted with conventional electronics where it is the charge of particles that is used. In parallel, the field of magnonics have made advances on the generation and manipulation of spin waves as a potential alternative for information technology. A spin wave is a collective excitation (quasi-particle of spin 1 called magnon) of spins that can, as their name suggest, propagate and depend strongly on the damping factor of the propagation media which is normally ferromagnetic material. In order to study these excitations, the ferromagnetic transition elements (Fe, Co and Ni) together with their alloys of low damping factor are of common use. Other very commonly used material, in this case a ferrimagnet, is yttrium iron garnet (YIG) which has the lowest known damping factor. Recently it has been shown that spin waves propagating along edges of magnetic structures allow for a better manipulation of the propagation direction and transmission of information at higher frequencies, which are problematic found with previous technology [1]. Investigation in this fields of research has generated a great number of applications where one of the most important is the development of logic devices. Some work has been done implementing non-reciprocity effects in this direction of research [2].

Overview of the materials to be studied

Three different materials have been studied: $Y_3Fe_5O_{12}$ (YIG), $Ni_{80}Fe_{20}$(Py) and CoFeB.

YIG is a ferrimagnet insulator which has been used repeatedly in numerous spintronics studies and applications due to its remarkable propagation properties resulting from a very low damping factor that has been found to be even in the 10^{-5} order of magnitude [3]. It has a relatively low saturation magnetization which is 140 $emu \cdot cm^{-3}$($\mu_o M_s$=176.0 mT) at 295 K [4]. It is very difficult to fabricate a good quality YIG thin film, since it would need to be epitaxially grown to have interesting properties. Unfortunately, epitaxial techniques just allow to obtain bulk samples. Recent progress in thin films growth have permitted the elaboration of films comparable to the conventional liquid phase epitaxy μm thick samples [5].

Permalloy is magnetically very homogeneous and its easy deposition process by magnetron sputtering makes it very used in different applications. The name Permalloy refers to alloys of Ni and Fe with different concentrations, but the better magnetic behavior has been found for the $Ni_{80}Fe_{20}$ Permalloy [6]. It has a well known saturation magnetization of approximately 725.8 $emu \cdot cm^{-3}$ ($\mu_o M_s$= 1 T) and damping factor of 0.006-0.009 has been reported [7].

CoFeB is an alloy for which an effective magnetization of approximately 1432 $emu \cdot cm^{-3}$ ($\mu_o M_{eff}$= 1.8 T) has been measured [8]. Normally in this alloy a significant uniaxial anisotropy is present which is included in the value of M_{eff}. In particular for thickness $\leq 2nm$ the anisotropy causes the magnetization to point out-of-plane [8]. Damping factors have been obtained in the range 0.004-0.006 [8, 9]. Thin films are normally grown by ion-beam deposition or magnetron sputtering.

Frecuency non-reciporcity

The amplitudes and profile of counter-propagating spinwaves can differ importantly [2]. Namely, in the case of the so-called magnetostatic surface wave (MSSW), when $\vec{M}$ and $\vec{k}$ are perpendicular and both are in-plane, spinwave amplitude non-reciprocity effects have been observed. More recently, frequency non-reciprocity for spinwaves, where the frequencies of two counter-propagating waves differ, is also achievable when the conditions on the top and bottom surfaces of the film are different. A way of braking the symmetry between the two surfaces is by having different surface anisotropy at the top and bottom of the film (surface anisotropy is related to the lack of symmetry in the vicinity of a film surfaces) [10]. This inspires an interest in manipulating the surface anisotropy of thin films in order to enhance the frequency non-reciprocity to be implemented in the design of logic devices. One possible application would be a ”spinwave diode”, where the propagating spin waves in a ferromagnetic material are forced to propagate in a specific direction by exploiting the non-reciprocity effects. This would be the parallel to the electric diode where the electric current can flow just in one direction.

Magnetic bilayers are a hot topic nowadays in the spintronics field. Although a theoretical background about the coupling of the two layers is not yet well-established and the magnetization dynamics at the interface is still unexplored, they are of great interest due to their potential to generate logic devices. Different combinations of materials are under investigation because of their good magnetic properties; both Py/CoFeB and YIG/Py are candidates. In the present study, a characterization of the magnetic properties of YIG/Py is performed and an approach to the conditions at the interface and the interaction between the layers is addressed.

Measurements techniques to probe the magnetization dynamics

The present interest on ferromagnetic materials materials and their technological applications requires a better understanding of their magnetic properties. There exist several techniques that allow to study the magnetic properties of a specif material. Thin film geometry is of special interest due to its applicability in electronic devices.

One of these techniques is the commonly known Ferromagnetic Resonance (FMR). It is based on monitoring the power absorption of the ferromagnetic sample due to the precession of the magnetization when a resonance condition is achieved. The sample is subjected to an static external applied field, created by an electromagnet, and exited at microwave frequencies (where the resonance dynamics of $\vec{M}$ occurs) by different methods. Historically, the first methods of of excitation consist in the creation of standing microwave field inside a cavity where the sample is placed. The frequency of the resonance is given by the cavity, and different cavities are needed to probe different frequencies.

A more commonly used excitation technique is the inductive permeameter where a microwave signal is conducted by a strip line or coplanar waveguide (CPW) over which the sample is placed. This waveguide excites the sample, and the magnetic response can be probed by a change of inductance on the waveguide. For this study, phase sensible measurements are performed with a vector network analyzer (VNA). This allows to measure the real an imaginary part of the reflection an transmission of power in the microwave network. This technique allows to extract about all the magnetic information of the sample by the use of the independent dispersion relations of the different modes of oscillation of the magnetization.

Another technique is Propagating Spin Wave Spectroscopy where magnetostatic wave modes are measured. The main difference with FMR is the excitation of modes with non-zero propagating wave number k. To achieve this, a non-uniform excitation field is created by an antenna that excites the wave that is measured by other receiving antenna. The propagation typically reaches the mm length in bulk YIG and tens of μm in Py due to the increased damping in conducting films [11].

Manuscript Organization and Objectives

The text has been organized in 5 Chapters whose contents is summarized now.

In Chapter 2, the main contributions to the magnetic energy in the ferromagnetic films are introduced together with the effective magnetic field. Landau Lifshitz Gilbert equation is introduced, from which the fundamental mode dispersion relation is obtained in a linear response regime with simple uniaxial anisotropy.

In Chapter 3 the main calculation for spin wave modes is performed. This chapter tackles the case where exchange interaction becomes important. The dispersion relations for perpendicular standing spinwave modes are obtained up to first order approximation following Kalinikos and Slavin's approach [12]. This model is used since the experimental frequency and field ranges allow to probe higher order modes. The calculations, where the most general conditions of applied field and direction of propagation were considered, are fully developed in the Appendices. This was done since the only reference to the calculation is extremely summarized and skips many important and instructive steps that are presented in this manuscript.

In Chapter 4 a full description of the experimental setup is given together with explanations of the microwave corrections that are needed in order to extract the magnetic response of the samples by eliminating any contribution due to the network itself. This is done with the intention of presenting a summary of a correct measurement procedure in the case of CPW-FMR.

In Chapter 5 the results for the five samples measured are presented with their respective discussion about the peculiarities found. Spectra, dispersion relations and linewidths are presented. In this chapter the objective is to compare the different response of the samples and give an estimation of their magnetic properties.

2 Basic magnetization dynamics: Uniform precession

In order to describe the magnetic properties of the systems presented in this manuscript, the continuum model will be used. In other words, the macroscopic magnetization is the quantity of interest

$$\vec{M}=\frac{\sum_V \vec{\mathfrak{m}}}{V} \tag{1}$$

where $\sum_V \vec{\mathfrak{m}}$ is the magnetic moment of the small but still macroscopic volume V of ferromagnet to be studied.

Now, the micromagnetic energies that will be considered in a ferromagnet are presented, and each term will contribute to the total internal magnetic effective field.

2.1 Magnetic energies

The total energy of a ferromagnet consist of various terms each accounting for different types of interactions. In this particular case, four main terms are of interest and will be modeled:

$$E_T = E_{ze} + E_{ex} + E_{de} + E_k \tag{2}$$

where E_{ze} is the Zeeman Energy, E_{ex} is the energy of exchange interaction, E_{de} is the energy term due to the demagnetizing field and E_k contains all the energy terms related to anisotropy.

2.1.1 Zeeman energy

This is the energy due to the interaction of the magnetization with the external magnetic field. Its density is given by [13]:

$$\varepsilon_{ze} = -\frac{\mu_o}{V}\int_V \vec{H_{ext}} \cdot \vec{M}\, dV \tag{3}$$

It clearly minimizes when the magnetization is aligned with the external field.

2.1.2 Exchange energy

This interaction is the one responsible for the magnetic order of ferromagnets. The exchange interaction has a quantum mechanical origin given by the Coulomb interaction of electrons and Pauli's exclusion principle. The Heisenberg Hamiltonian for a spin system can be written as

$$\hat{H} = -\sum_{ij} \Im_{ij} \hat{\vec{S}}_i \cdot \hat{\vec{S}}_j \tag{4}$$

where $\Im_{ij}$ is the exchange integral between the spins S_i and S_j and quantifies their interaction. Usually, in a discrete model, this interaction is just considered to first neighbors.

In the continum model the exchange energy density,due to non-uniform magnetization, can be expressed as

$$\varepsilon_{Ex}=\frac{A}{V}\int_V \left(\nabla|\vec{M}|\right)^2 dV \tag{5}$$

which describes an energy penalty by any deviation of the magnetization from a constant equilibrium direction. The exchange constant A with units J/m depends on the material and can be related to $\Im_{ij}$. This energy is isotropic, since it does not depend on the direction of change relative to the direction of the magnetization [13]. There are several types of exchange interaction and equation (5) accounts for the balance of most of them.

2.1.3 Demagnetizing field energy

This is a contribution due to the magnetic field created by the solid itself. This is given by the dipolar interactiton between magnetic moments in the material. This interaction creates a field that opposes the magnetization, reason why it is called demagnetizing field. In the case there is not other magnetic field, the demagnetizing field is obtained from Maxwell's equation $\nabla \cdot \vec{B} = \mu_o \nabla \cdot (\vec{H_{de}} + \vec{M})$ as

$$\nabla \cdot \vec{H_{de}} = -\nabla \cdot \vec{M} \tag{6}$$

From this, the expression for the energy density can be given by [13]:

$$\varepsilon_{de} = -\frac{\mu_o}{2V} \int_{sample} \vec{H_{de}} \cdot \vec{M}\, dV \tag{7}$$

It was found by Kittel [14] that the demagnetizing field depends on the samples shape and in the case of an uniform magnetized ellipsoid the field is given by:

$$\vec{H_{de}} = -\hat{N}_{de}\vec{M} \tag{8}$$

where $\overline{N}$ is the demagnetizing tensor. When the system of reference is oriented along the principal axis of the ellipsoid, the demagnetizing tensor takes the form [13]:

$$\hat{N_{de}}=\begin{bmatrix} N_{de}^{xx} & 0 & 0 \\ 0 & N_{de}^{yy} & 0 \\ 0 & 0 & N_{de}^{zz} \end{bmatrix} \tag{9}$$

where the trace satisfies $N_{de}^{xx} + N_{de}^{yy} + N_{de}^{zz}$=1.

For the special case of a ferromagnet in the shape of a infinitely extended thin film (limiting case of a disc shaped ellipsoid), it can be shown that the demagnetizing field and the energy density are given by (x-axis perpendidular to the film, $N_{de}^{xx} = 1$, $N_{de}^{yy,zz} = 0$) [13, 11]:

$$\vec{H_{de}} = -(\hat{x} \cdot \vec{M})\hat{x} \tag{10}$$

$$\varepsilon_{de} = \frac{\mu_o}{2}(\hat{x} \cdot \vec{M})^2 \tag{11}$$

2.1.4 Anisotropy energy

This contribution to the energy depends on the direction of the magnetization with respect to the structural axis of the material. In the case of the cubic anisotropy its origin is in the spin-orbit interactions which are dependent of the orientation with respect to the solid lattice structure. The energy density for the cubic magnetic anisotropy is given up to second order by [13]:

$$\varepsilon_{Kc} = K_{c1}((m^x)^2 (m^y)^2 + (m^x)^2 (m^z)^2 + (m^y)^2 (m^z)^2) + K_{c2} (m^x)^2 (m^y)^2 (m^z)^2 \tag{12}$$

where the m$_i$ are the components of the normalized magnetization $\vec{m} = \vec{M}/M_s$ along the cubic axes of the solid lattice. K_{c1} and K_2 are the anisotropy constants of first and second order. Usually the later and other higher-order constants can be neglected. K_{c1} have units J/m^3.

It can be the case that a bulk uniaxial anisotropy exist:

$$\varepsilon_{Ku} = -K_1(\hat{n} \cdot \vec{m})^2 \tag{13}$$

where K_1 is called the uniaxial anisotropy constant. If $K_1 > 0$ the n-axis (perpendicular to the film) is called the easy axis, and if $K_1 < 0$ it is called the hard axis since it requires more energy for the magnetization to be parallel to it. Then, it is clear that the magnetization tends to align along the easy axis and perpendicular to the hard axis [13]. This type of anisotropy is the one that will be attributed to the bulk in the analysis.

For thin films another type of anisotropy is important. The surface anisotropy density (to be integrated over the surface) is given by [13]:

$$\varepsilon_{Ks} = K_{s1}(1 - (m^x)^2 (n^x)^2 - (m^y)^2 (n^y)^2 - (m^z)^2 (n^z)^2)$$

$$- 2K_{s2} (m^x m^y n^x n^y + m^x m^z n^x n^z + m^y m^z n^y n^z) \tag{14}$$

where the n$_i$ are the components of the surface normal vector $\vec{n}$ projected along the cubic axes of the solid lattice. K_{s1} and K_{s1} have units J/m^2. In this case, it is called surface anisotropy and is attributed to the loss of symmetry in the environment of atoms near the surface of a sample. This is why this effect is not important for bulk samples, since for such case the surface magnetization gets coupled with the magnetization from the rest of the solid [13].

A phenomenological uniaxial surface anisotropy density will be considered for the analysis:

$$\varepsilon_{Ks} = \begin{cases} -\frac{K_{Stop}(M^x)^2}{M_s^2}\delta(x - l/2) & x = l/2\,(top\,surface) \\ -\frac{K_{Sbot}(M^x)^2}{M_s^2}\delta(x + l/2) & x = -l/2\,(bottom\,surface) \end{cases} \tag{15}$$

where l is the film thickness (assuming x-axis is perpendicular to film sample) and K_s^{top}, K_s^{bot} are the phenomenological surface anisotropy constants at the top and bottom of the film respectively [10]. The form of the energy density of surface anisotropy (delta function) is justified by the fact that this contribution becomes important just at a very thin boundary layer at the top and bottom surfaces of the ferromagnetic films.

2.2 Effective field

At a fixed temperature T, the local minima of the total energy E_T (integral of the sum of energy densities) correspond to the different equilibrium configurations of the system's magnetization. By deriving the total energy density with respect to the magnetization components, the effective field can be obtained [15]:

$$\mu_o \vec{H_{eff}} = -\vec{\nabla}_{\vec{M}}\varepsilon_T \tag{16}$$

Considering all the contributing terms presented in equation (2) (expanding the anisotropy contribution), it is clear that:

$$\vec{H_{eff}} = \vec{H_{ze}} + \vec{H_{Ex}} + \vec{H_{de}} + \vec{H_{Ku}} + \vec{H_{Ks}} \tag{17}$$

2.3 Equation of motion of the magnetization

Landau and Lifshitz proposed the equation of motion for the magnetization (LL equation) which comes from the torque equation for a magnetic moment and the quantum relation between the magnetic moment and the angular mometum [16]:

$$\frac{\partial \vec{M}}{\partial t} = -\gamma\mu_o\vec{M} \times \vec{H_{eff}} \tag{18}$$

LL equation describes the precession motion of the magnetization on a cone of constant angle β around H_{eff} as shown in Figure 1. Here the gyromagnetic ratio γ is a quantity characteristic of the collective magnetic moments forming a particular sample. It is not equal to the value of γ for the free ions or γ_e the electron and has to be determined by experimentation [16]. From (18), it can be concluded that:

$$\frac{\partial M^2}{\partial t} = 0 \tag{19}$$

Equation (19) implies that the norm of the magnetization is conserved in time, i.e. the magnetization changes direction with constant magnitude at saturation M_s. This will be considered throughout this manuscript.

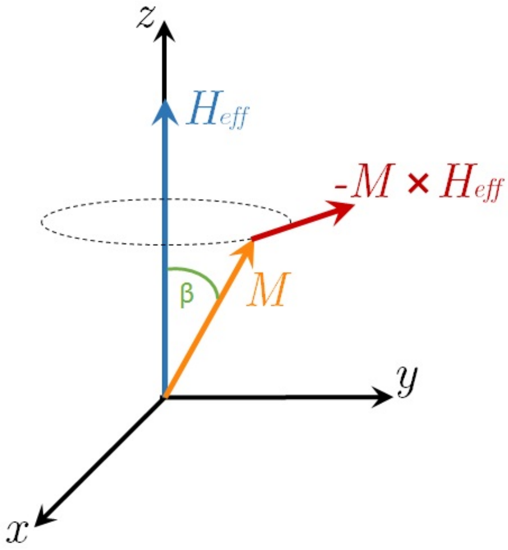

Figure 1: Precession of the magnetization around an equilibrium position with cone angle β

2.4 Dynamic susceptibility without losses

Consider a ferromagnet under the influence of a ac magnetic field $\vec{h}^{\sim}$ and a static magnetic field $\vec{H_{eff}}$ (which is the effective field). The field $\vec{h}^{\sim}$ is perpendicular to the static field. This cause the magnetization to have a variable component ($\vec{m}^{\sim}$) too:

$$\vec{H} = \vec{H_{eff}} + \vec{h}^{\sim} \qquad \vec{M} = \vec{M_s} + \vec{m}^{\sim} \tag{20}$$

where $\vec{M}_s$ is the equilibrium saturation magnetization.

The aim is to solve equation (18) using linear approximation where the oscillating magnetic field $\vec{h}^{\sim}$, and the oscillating part of the magnetization $\vec{m}^{\sim}$ are small according to: $\vec{h}^{\sim} \ll \vec{H_{eff}}$ and $\vec{m}^{\sim} \ll \vec{M}_s$.

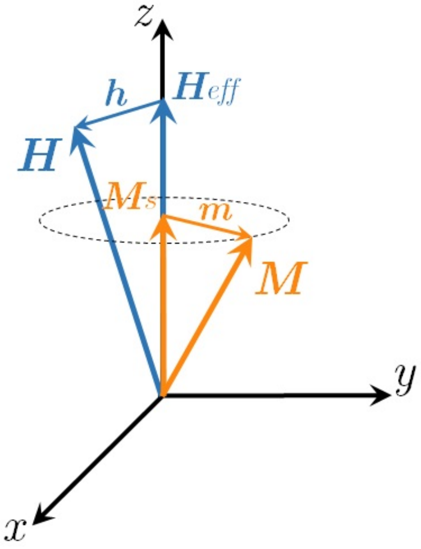

Figure 2: Linear approximation representation for LL equation

Replacing equations (20) into (18) and taking all the terms to the first order (with the condition of equilibrium $\vec{M}_s \times \vec{H_{eff}} = \vec{0}$), the following differential equation is obtained:

$$\frac{\partial \vec{m}^{\sim}(t)}{\partial t} = -\gamma\mu_o \left(\vec{m}^{\sim}(t) \times \vec{H_{eff}} + \vec{M}_s \times \vec{h}^{\sim}(t) \right) \tag{21}$$

The solutions of interest for the equation have the form: $\vec{h}^{\sim}(t) = \vec{h}e^{i\omega t}$ and $\vec{m}^{\sim}(t) = \vec{m}e^{i\omega t}$. Inserting these fields, expressed in their cartesian components, into (21) leads to the following system of equations:

$$i\omega m^x = \gamma\mu_o M_s h^y - \gamma\mu_o H_{eff} m^y \tag{22}$$

$$i\omega m^y = \gamma\mu_o H_{eff} m^x - \gamma\mu_o M_s h^x \tag{23}$$

$$i\omega m^z = 0 \tag{24}$$

the solutions for $\vec{m}$ [16] are:

$$m^x = \chi h^x + i\chi_a h^y \tag{25}$$

$$m^y = -i\chi_a h^x + \chi h^y \tag{26}$$

$$m^z = 0 \tag{27}$$

where

$$\chi = \frac{\omega_M \omega_H}{\omega_H^2 - \omega^2} \qquad \chi_a = \frac{\omega_M \omega}{\omega_H^2 - \omega^2} \tag{28}$$

Clearly, equations (25-27) determine the linear relation between $\vec{m}$ and $\vec{h}$ first obtained by Polder [17]. In the above relations:

$$\omega_H = \gamma \mu_o H_{eff} \tag{29}$$

$$\omega_M = \gamma \mu_o M_s \tag{30}$$

Equations (25-27) can also be written in tensor form:

$$\vec{m} = \overline{\chi}\vec{h} \tag{31}$$

where $\overline{\chi}$ is the high-frequency magnetic susceptibility tensor or also called Polder tensor defined by [16]:

$$\overline{\chi} = \begin{bmatrix} \chi & i\chi_a & 0 \\ -i\chi_a & \chi & 0 \\ 0 & 0 & 0 \end{bmatrix} \tag{32}$$

It is clear from (28) that the tensor definition implies a resonance condition for $\omega = \omega_H$.

Other important observation is that such resonant behavior occurs only for ac fields circular component with right-hand rotation with respect to M_s [16]. The circular components are defined as:

$$h_\pm = h^{x\sim} \pm i h^{y\sim} \qquad m_\pm = m^{x\sim} \pm i m^{y\sim} \tag{33}$$

and from (31) it can be obtained that:

$$m_\pm = \chi_\pm h_\pm \tag{34}$$

where $\chi_\pm$ is defined by

$$\chi_\pm = \chi \pm \chi_a = \frac{\gamma \mu_o M_s}{\omega_H \mp \omega} \tag{35}$$

Therefore, just χ_+ present a resonance behavior. It is obvious too that this cannot model a real ferromagnet. These equations would imply a divergence of the susceptibility at the resonance frequency. The experiments does not agree with such behavior and the problem is solved by introducing a damping parameter into LL equation which will be explained later.

Note that equation (25-27) can also be written in the inverse way

$$\vec{h} = \begin{bmatrix} \frac{\omega_H}{\omega_M} & -i\frac{\omega}{\omega_M} \\ i\frac{\omega}{\omega_M} & \frac{\omega_H}{\omega_M} \end{bmatrix} \vec{m} \tag{36}$$

2.5 Shape effects on resonance frequency

It has been shown by Kittel that the shape of the ferromagnet influence importantly the resonance frequency via the demagnetizing factors that have already been introduced [14].

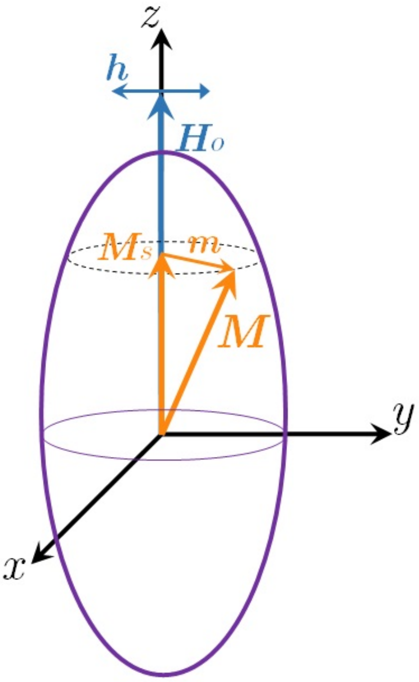

Figure 3: Field linear approximation configuration for a general ellipsoid

For the case of an ellipsoid, whose principal axis are parallel to the x, y, z-axis as shown in Figure 3, the demagnetizing field of equation (8) can be included into the total magnetic field:

$$\vec{H} = \vec{H_{ext}} + -\overline{N}\vec{M} + \vec{h}^{\sim} \tag{37}$$

to obtain:

$$H^x = h^{x\sim} - N^{xx}m^{x\sim} \tag{38}$$

$$H^y = h^{y\sim} - N^{yy}m^{y\sim} \tag{39}$$

$$H^z = H_{ext} - N^{zz}M_s \tag{40}$$

Solving for $\vec{h}$ (similarly to equation (36)) leads to:

$$\vec{h} = \overline{\chi}_K^{-1}\vec{m} = \frac{1}{\gamma\mu_o M_s}\begin{pmatrix} \omega_x & -i\omega \\ i\omega & \omega_y \end{pmatrix}\vec{m} \tag{41}$$

where $\overline{\chi}_K^{-1}$ is the Kittel inverse susceptibility tensor [17] defined using:

$$\omega_x = \gamma\mu_o\left[H_{ext} + (N^{xx} - N^{zz})M_s\right] \tag{42}$$

$$\omega_y = \gamma\mu_o\left[H_{ext} + (N^{yy} - N^{zz})M_s\right] \tag{43}$$

Since the components of the susceptibility tensor $\overline{\chi}_K$ diverge at resonance, then $det(\overline{\chi}_K) \to \infty$ and $det\left(\overline{\chi}_K^{-1}\right) \to 0$. From equation (41) the resonance condition leads to :

$$\omega = \sqrt{\omega_x\omega_y} = \gamma\mu_o\left(\left[H_{ext} + (N^{xx} - N^{zz})M_s\right]\left[H_{ext} + (N^{yy} - N^{zz})M_s\right]\right)^{\frac{1}{2}} \tag{44}$$

recovering the famous Kittel formula for the resonance frequency [14]. Going back to Figure 3 and recalling that an infinite film is a limiting case of an ellipsoid, it can be calculated that for a film magnetized in the yz-plane $N^{yy} = N^{zz} = 0$ and $N^{xx} = 1$, then:

$$f = \frac{\gamma}{2\pi}\mu_o\left(H_{ext}\left[H_{ext} + M_s\right]\right)^{\frac{1}{2}} \tag{45}$$

and for a film magnetized out-of-plane (along the z-axis) $N^{xx} = N^{yy} = 0$ and $N^{zz} = 1$:

$$f = \frac{\gamma}{2\pi}\mu_o\left[H_{ext} - M_s\right] \tag{46}$$

This are not the more general resonance frequency functions since it just accounts for the demagnetizing field. The introduction of the bulk uniaxial anisotropy field is treated simply in the next section, while a more general derivation of the oscillation modes of the magnetization where all interactions are considered is performed in Chapter 3.

2.6 Introduction of bulk uniaxial anisotropy term in the Landau Lifshitz equation

When the energy term of a uniaxial bulk anisotropy is taken into account for the total energy density (equation (13)), there is a new field term to be considered resulting of the application of (16) [20]:

$$\vec{H}_{Ku}{=}\frac{2K_1}{\mu_0 M_s^2}M^n\hat{n} \tag{47}$$

Now, if the external steady field $\vec{H}_{ext}$ is applied in the z-axis and the ac field $\vec{h}^{\sim}$ is in the xy-plane, the magnetization takes the form: $\vec{M}=(m^{x\sim},\, m^{y\sim},\, M_s)$.

For the case when the magnetization is parallel to the film (say the x-axis is perpendicular to the film):

$$\vec{H}_{Ku}{=}-\begin{bmatrix} -\frac{2K_1}{\mu_0 M_s^2} & 0 & 0 \\ 0 & 0 & 0 \\ 0 & 0 & 0 \end{bmatrix}\begin{pmatrix} m_x^{x\sim} \\ m_x^{y\sim} \\ M_s \end{pmatrix} \tag{48}$$

On the other hand, when the magnetization is parallel to the film (say the z-axis is perpendicular to the film):

$$\vec{H}_{Ku}{=}-\begin{bmatrix} 0 & 0 & 0 \\ 0 & 0 & 0 \\ 0 & 0 & -\frac{2K_1}{\mu_0 M_s^2} \end{bmatrix}\begin{pmatrix} m_x^{x\sim} \\ m_x^{y\sim} \\ M_s \end{pmatrix} \tag{49}$$

From this, a compact expression is obtained for a effective demagnetizing field $\vec{H}'_{de}$ in the case of an ellipsoid (see Figure 3):

From these addition of anisotropy to the energy equation, the following replacements have to be done to equation (44) to correctly describe the resonance frequency dependence with the field:

$$\begin{gathered} N^{xx}\rightarrow N^{xx}-\frac{2K_1}{\mu_0 M_s^2}\ \ (magnetized\,in-plane) \\ N^{zz}\rightarrow N^{zz}-\frac{2K_1}{\mu_0 M_s^2}\ \ (magnetized\,out-of-plane) \end{gathered} \tag{50}$$

The two previous sections have shown how to easily include field terms that can be expressed in a constant demagnetizing tensor form $\vec{H}_{other}{=}-\hat{N}_{other}\vec{M}$. For this, $\hat{N}_{other}$ needs to be defined in the whole film and has to be constant on it. This approach is useful when simple terms like a uniaxial anisotropy are considered, but when other interactions like exchange or surface anisotropy enter the field equation a more complete theory is needed. Chapter 3 develops a theory around this problem.

2.7 Landau Lifshitz Gilbert equation and presence of losses

In a real ferromagnet, the magnetization tends to align with the direction of minimal energy after some time through a relaxation process. This presents a exponential decay in amplitude while describing a spiral as shown in Figure 4.

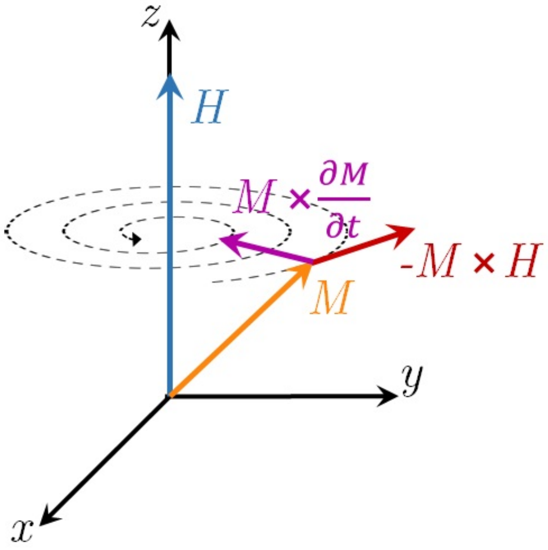

Figure 4: Relaxation process of the magnetization due to Damping

Such process was modeled by the introduction of a phenomenological dissipation term by Gilbert [18], leading to the well known Landau Lifshitz Gilbert equation (LLG):

$$\frac{\partial \vec{M}}{\partial t} = -\gamma\mu_o \vec{M} \times \vec{H_{eff}} + \frac{\alpha}{|\vec{M}|}\vec{M} \times \frac{\partial \vec{M}}{\partial t} \tag{51}$$

Here α is the dimensionless damping parameter to be obtained experimentally. It should be clear that equation (51) stills agree with the conservation of the magnetization's magnitude (equation (19)).

To solve LLG equation, a similar linearization approach to the one used in LL equation can be performed. The linearised form of (51) is:

$$i\omega\vec{m} + \gamma\mu_o\vec{m} \times \vec{H_{eff}} - \frac{i\alpha\omega}{M_s}\vec{m} \times \vec{M_s} = -\gamma\mu_o\vec{M_s} \times \vec{h} \tag{52}$$

Nevertheless, expressions for the susceptibility χ_+ can be obtained just by the replacement of

$$\omega_H \to \omega_H + i\alpha\omega \tag{53}$$

into equation (35) [16]. This leads to the new complex susceptibility $\chi_c = \chi_c^{'} - i\chi_c^{''}$, in presence of damping, given by the components:

$$\chi_c^{'} = Re\left(\chi_+\right) = \frac{\gamma\mu_o M_s\left(\gamma\mu_o H_{eff} - \omega\right)}{(\gamma\mu_o H_{eff} - \omega)^2 + (\alpha\omega)^2} \tag{54}$$

$$\chi_c^{''} = Im\left(\chi_+\right) = \frac{-\alpha\gamma\mu_o M_s\omega}{(\gamma\mu_o H_{eff} - \omega)^2 + (\alpha\omega)^2} \tag{55}$$

The imaginary part of the complex susceptibility corresponds to the energy absorption of the system. The complex susceptibility components, for values of $\mu_o M_s = 1$ [T], $\gamma/2\pi = 29.31[GHzT^{-1}]$, $\alpha = 0.03$ and $\omega/2\pi = 20$ [GHz], are plotted in Figure 5.

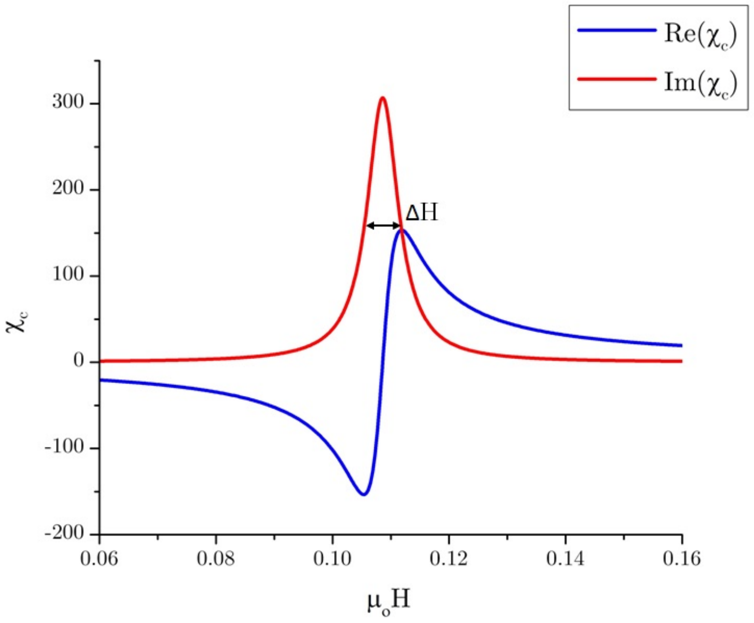

Figure 5: Calculated Susceptibility for typical values of Permalloy

Experimentally the damping parameter α is determined by sweeping the field at some fixed frequency and measuring the linewidth of the resonance ΔH at half-maximum. The relation between these two quantities is given by [16]:

$$\Delta H = \frac{2\alpha\omega}{\gamma\mu_o} + \Delta H_o \tag{56}$$

Here ΔH_o is the linewidth at zero frecuency.

3 Standing spin wave modes: Non-uniform precession

The non-uniform modes of precession of the magnetization receive the name of spin waves. In these modes the spins oscillate with the same frequency but with different phases. The term spin wave is used to refer to two types of waves: magneto-static waves and dipole-exchange spin waves. The former present an overcome of the dipolar interaction over the exchange interaction since the wavelength λ is much larger than the exchange length Λ. In the case of dipolar-exchange spin waves the exchange interaction becomes important and should be taken into account.

The objective of this section is to obtain a general form for the dispersion relation of non-uniform precession modes where the dipole and exchange interaction are both important in thin films. The spin wave modes approach developed by Kalinikos and Slavin [12] is followed and modified to include surface anisotropy (equation (15)) in the dispersion relation for the perpendicular standing spin wave (PSSW) modes [20].

3.1 Geometry and systems of coordinates

Consider a infinite ferromagnetic film of thickness l magnetized to saturation by an external field H. The system of coordinates $\xi\eta\zeta$ is such that ξ=0 is located at half thickness and the η and ζ-axis are in the plane of the film. Now consider the system of coordinates xyz such that the saturation magnetization M_s is along the z-axis as well as the internal magnetic field H_i. The internal field in this case contains all the static contributions to the magnetic field, i.e. external field, dipolar static field, and anisotropy static field. The two systems are related by the angles θ (angle between the ξ and z-axis) and φ (angle between the xz-plane cut on the $\eta\zeta$-plane and the ζ-axis). This treatment, in comparison with the previous chapter, allows to obtain more general angle dependent dispersion relations than the one obtained in equation (44) and consider non-uniformities of the dynamics.

3.2 Variable magnetic field equation

Without loss of generality, consider the spin wave propagating in the ζ direction given by equation (6)[12]

$$\vec{m}^{\sim} = \vec{m}^{\sim}(\xi,\zeta,t) = \vec{m}(\xi)e^{i(\omega t - k_\zeta \zeta)} \tag{57}$$

where the magnetization vector $\vec{m}(\xi)$ can be decomposed in two components

$$\vec{m}(\xi) = m^x(\xi)\hat{x} + m^y(\xi)\hat{y} \tag{58}$$

The variable magnetic field inside the film is given by:

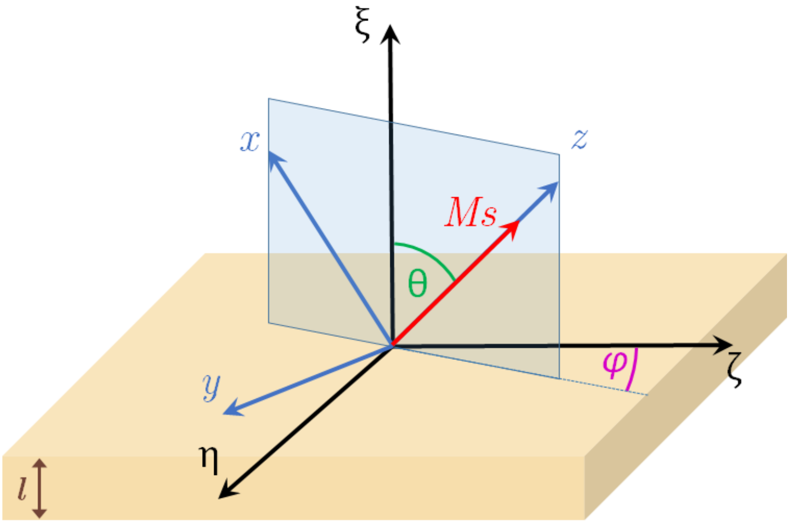

Figure 6: Systems of coodinates of the sample and the magnetization related by θ and φ

$$\vec{h}^{\sim}=\vec{h}_d+\vec{h}_K+\vec{h}_{Ex} \tag{59}$$

Where the field contributions are the dipolar field $\vec{h}_d$, the anisotropy field $\vec{h}$ and the exchange field $\vec{h}_{Ex}$[12, 21].

- **Dipolar Field**

The dipolar field is expected to have a plane wave behavior too

$$\vec{h}_d=\vec{h}(\xi)e^{i(\omega t-k_\zeta \zeta)} \tag{60}$$

where the field $\vec{h}(\xi)$ inside the film can be expressed in terms of the tensorial Green's function $\hat{G}(\xi,\xi')$ as [22]:

$$\vec{h}(\xi)=\int_{-l/2}^{l/2}\hat{G}(\xi,\xi')\vec{m}(\xi')d\xi' \tag{61}$$

where the Green's function $\hat{G}(\xi,\xi')$ is the xy part of the $\hat{G}_{xyz}(\xi,\xi')$ function obtained from a change of coordinates applied to the Green's function defined in the $\xi\eta\zeta$ coordinate system as [12, 22]:

$$\hat{G}_{\xi\eta\zeta}(\xi,\xi')=\begin{bmatrix} G_P-\delta(\xi-\xi') & 0 & iG_Q \\ 0 & 0 & 0 \\ iG_Q & 0 & -G_P \end{bmatrix} \tag{62}$$

and

$$G_P = \frac{k_\zeta}{2} e^{-k_\zeta |\xi - \xi'|} \tag{63}$$

$$G_Q = G_P sing(\xi - \xi') \tag{64}$$

To obtain $\hat{G}_{xyz}(\xi, \xi')$, the rotation matrices easily obtained from Figure 6 are used:

$$\hat{C} = \begin{bmatrix} Sin\theta & -Cos\theta Sin\varphi & -Cos\theta Cos\varphi \\ 0 & Cos\varphi & -Sin\varphi \\ Cos\theta & Sin\theta Sin\varphi & Sin\theta Cos\varphi \end{bmatrix} \tag{65}$$

$$\hat{C}^{-1} = \begin{bmatrix} Sin\theta & 0 & Cos\theta \\ -Cos\theta Sin\varphi & Cos\varphi & Sin\theta Sin\varphi \\ -Cos\theta Cos\varphi & -Sin\varphi & Sin\theta Cos\varphi \end{bmatrix} \tag{66}$$

Therefore

$$\hat{G}_{xyz}(\xi, \xi') = \hat{C}\hat{G}(\xi, \xi')\hat{C}^{-1} \tag{67}$$

Once the transformation is performed, the following 2 by 2 matrix can be obtained

$$\hat{G}(\xi, \xi') = \begin{bmatrix} \left(Sin^2\theta - Cos^2\theta Cos^2\varphi\right) G_P & -Cos\theta Sin\varphi Cos\varphi G_P \\ -2iSin2\theta Cos\varphi G_Q - \delta(\xi - \xi') Sin^2\theta & -iSin\theta Sin\varphi G_Q \\ & \\ -Cos\theta Sin\varphi Cos\varphi G_P - iSin\theta Sin\varphi G_Q & -Sin^2 G_P \end{bmatrix} \tag{68}$$

- **Anisotropy field**

The anisotropy field is calculated as

$$\vec{h}_K = -\hat{N}_A^{xy}\vec{m}^{\sim}\text{=-}\begin{bmatrix} N^{xx} & N^{xy} \\ N^{yx} & N^{yy} \end{bmatrix} \vec{m}(\xi) e^{i(\omega t - k_\zeta \zeta)} \tag{69}$$

where $\hat{N}_A^{xy}$ is the xy-part of the anisotropy tensor defined by

$$\hat{N}_A^{xyz} = -\begin{bmatrix} N^{xx} & N^{xy} & N^{xz} \\ N^{yx} & N^{yy} & N^{yz} \\ N^{zx} & N^{zy} & N^{zz} \end{bmatrix} \tag{70}$$

Of course, the anisotropy tensor will be easily defined first in the $\xi\eta\zeta$ coordinate system as $\hat{N}_A^{\xi\eta\zeta}$, and then transformed to the xyz system to obtain $\hat{N}_A^{xyz}$. This transformation is performed in the same way as was already done for the dipolar field.

- **Exchange field**

The exchange field, easily calculated from equation (5), is

$$\vec{h}_{Ex} = \Lambda^2 \nabla^2_{\xi\eta\zeta} \vec{m}^{\sim} = \Lambda^2 (\frac{\partial^2}{\partial \xi^2} - k_\zeta^2) \vec{m}(\xi) e^{i(\omega t - k_\zeta \zeta)} \tag{71}$$

where the exchange length $\Lambda = \left(\frac{2A}{\mu_o M_s^2}\right)^{1/2}$ is defined as the length to which the exchange interaction is comparable with the dipolar interaction [20].

- **LL equation**

Replacing the fields $\vec{m}^{\sim} + \vec{M}_s$ and $\vec{h}^{\sim} + \vec{H}_i$ in the LL equation (18) leads to:

$$i\omega \vec{m}^{\sim} = -\gamma \mu_o \left[-H_i \hat{z} \times \vec{m}^{\sim} + M_s \hat{z} \times (\vec{h}_d + \vec{h}_K + \vec{h}_{Ex}) \right] \tag{72}$$

Equation (72) can be written as[1]

$$i\omega \begin{pmatrix} 0 & -1 \\ 1 & 0 \end{pmatrix} \begin{pmatrix} 0 & 1 \\ -1 & 0 \end{pmatrix} \vec{m}(\xi) = \gamma \mu_o H_i \begin{pmatrix} 0 & -1 \\ 1 & 0 \end{pmatrix} \vec{m}(\xi)$$

$$-\gamma \mu_o M_s \begin{pmatrix} 0 & -1 \\ 1 & 0 \end{pmatrix} \left[\vec{h}(\xi) + \Lambda^2 (\frac{\partial^2}{\partial \xi^2} - k_\zeta^2) \vec{m}(\xi) - \begin{bmatrix} N^{xx} & N^{xy} \\ N^{yx} & N^{yy} \end{bmatrix} \vec{m}(\xi) \right] \tag{73}$$

Isolating $\vec{h}(\xi)$ in equation (73) and considering that $\omega_H = \gamma \mu_o H_i$ and $\omega_M = \gamma \mu_o M_s$ the following expression is obtained for $\vec{h}(\xi)$

$$\vec{h}(\xi) = \hat{F} \vec{m}(\xi) = \begin{bmatrix} \frac{\omega_H}{\omega_M} - \Lambda^2 (\frac{\partial^2}{\partial \xi^2} - k_\zeta^2) + N^{xx} & -i \frac{\omega}{\omega_M} + N^{xy} \\ i \frac{\omega}{\omega_M} + N^{yx} & \frac{\omega_H}{\omega_M} - \Lambda^2 (\frac{\partial^2}{\partial \xi^2} - k_\zeta^2) + N^{yy} \end{bmatrix} \vec{m}(\xi) \tag{74}$$

Following Kalinikos et al. idea [12, 21], the operator $\hat{F}$ (equation (74)) is separated in the part $\hat{R}$ that contains the exchange and diagonal dipole part, and the part $\hat{T}$ with anisotropy and non-diagonal dipole part. After equating expressions (74) and (61)

$$\hat{R} \vec{m}(\xi) = -\hat{T} \vec{m}(\xi) + \int_{-l/2}^{l/2} \hat{G}(\xi, \xi') \vec{m}(\xi') d\xi' \tag{75}$$

---

[1] Note that the cross product can be expressed like $\hat{z} \times \begin{pmatrix} v_x \\ v_y \end{pmatrix} = \begin{pmatrix} -v_y \\ v_x \end{pmatrix} = \begin{pmatrix} 0 & -1 \\ 1 & 0 \end{pmatrix} \begin{pmatrix} v_x \\ v_y \end{pmatrix}$, and the identity as $I = \begin{pmatrix} 0 & -1 \\ 1 & 0 \end{pmatrix} \begin{pmatrix} 0 & 1 \\ -1 & 0 \end{pmatrix}$.

where the above operators are given by:

$$\hat{R} = \begin{bmatrix} \frac{\omega_H}{\omega_M} - \Lambda^2(\frac{\partial^2}{\partial\xi^2} - k_\zeta^2) & 0 \\ 0 & \frac{\omega_H}{\omega_M} - \Lambda^2(\frac{\partial^2}{\partial\xi^2} - k_\zeta^2) \end{bmatrix} \tag{76}$$

$$\hat{T} = \begin{bmatrix} N^{xx} & -i\frac{\omega}{\omega_M} + N^{xy} \\ i\frac{\omega}{\omega_M} + N^{yx} & N^{yy} \end{bmatrix} \tag{77}$$

This last equation is the variable magnetic field equation which is made from various transformation applied to the variable magnetization. This equation therefore determines the variable magnetization amplitude $\vec{m}(\xi)$. This is no longer a linear problem, like in Chapter 2, due to the differential operators in $\hat{R}$. A second order differential equation problem has to be solved, which implies some boundary conditions are needed. The following section tackles this problematic.

3.3 Spin Wave Modes

To solve equation (75), $\vec{m}(\xi)$ is expanded in a infinite series of complete orthonormal functions [12]:

$$\vec{m}(\xi) = M_s \sum_{n=0}^{\infty} \left[m_n^x \vec{S}_n^x(\xi) + m_n^y \vec{S}_n^y(\xi) \right] \tag{78}$$

Here, the functions $\vec{S}_n^x(\xi)$, $\vec{S}_n^y(\xi)$ are called spin wave modes (SWM). They are given by

$$\vec{S}_n^x(\xi) = (\Phi_n^x(\xi), 0) \;\; \vec{S}_n^y(\xi) = (0, \Phi_n^y(\xi)) \tag{79}$$

Then, refering to the field equation (75), the following eigen value problem is considered [12, 21]:

$$\hat{R}\vec{S}_n(\xi) = R\vec{S}_n(\xi) \tag{80}$$

$$\hat{B}_1\vec{S}_n(\xi) = 0 \;\; \xi = \frac{l}{2} \tag{81}$$

$$\hat{B}_2\vec{S}_n(\xi) = 0 \;\; \xi = -\frac{l}{2} \tag{82}$$

where $\hat{B}_j$ (j=1,2) are the boundary condition matrices for top (j=1) and bottom surfaces of the film (j=2). These are obtained from integrating the LL equation, considering the external, the exchange and surface anisotropy fields, in a thin boundary layer at the top and bottom of the film where the surface anisotropy takes effect [16]. They are given by:

$$\hat{B}_j = \left[\begin{array}{cc} (-1)^{j+1}\frac{\partial}{\partial\xi} + d_j^x & 0 \\ 0 & (-1)^{j+1}\frac{\partial}{\partial\xi} + d_j^y \end{array} \right] \tag{83}$$

$$d_j^x{=}d_j Cos2\theta,\ d_j^y{=}d_j Cos^2\theta \tag{84}$$

Here the d_j are the pinning parameters which quantifies how pinned or unpinned are the magnetic moments at the surface. When the moments are perfectly pinned at the surface ($\frac{\partial m^p}{\partial\xi} = \infty$), the variable magnetization is zero, while unpinned moments ($\frac{\partial m^p}{\partial\xi} = 0$) means that they are free to move. Note that the effective pinning d_j^p $(p = x,\, y)$ depends also on the direction of the saturation magnetization. Namely, when $\theta = \pi/2$ the component m_y is always free, but for $\theta = 0$ the two variable components can be pinned.

The solutions for the problem of equation (80) are the functions $\mathit{\Phi}_n^p(\xi)$ of the form:

$$\mathit{\Phi}_n^p(\xi) = A_n^p\left(Cos(\kappa_n^p\xi) + B_n^p Sin(\kappa_n^p\xi)\right) \tag{85}$$

Where the constants A_n^p and B_n^p have to be determined by the boundary conditions. The application of boundary conditions leads to the following equation defining the standing wave number κ_n^p (See Appendix A):

$$(\kappa_n^p - d_1^p d_2^p)\,Tan(\kappa_n^p l) = \kappa_n^p(d_1^p + d_2^p) \tag{86}$$

Equation (86) determines κ_n^p depending on the effective pinning parameters d_j^p. It is possible to have multiple solutions for κ_n^p. The κ_n^p are the standing wave numbers for the standing spin waves modes (85). Note that in general, each function $\mathit{\Phi}_n^x(\xi)$ and $\mathit{\Phi}_n^y(\xi)$ can have different κ_n^x, κ_n^y since they depend on the d_j^x and d_j^y parameters respectively.

For the present analysis, a simplified model of unpinned spins will be considered, then $d_j = d_j^p = 0$. Note this is always true, even if $d_2 \neq 0$, when the film is magnetized in-plane ($\theta = 0$) for the y direction. Considering this unpinned simplification, the condition for κ_n^p is

$$Sin(\kappa_n^p l) = 0 \Rightarrow \kappa_n^p = n\frac{\pi}{l} \tag{87}$$

Replacing this result in equation (152, see Appendix A) determines that $B_n^p{=}Tan(\kappa_n^p l/2)$. Therefore the solution for (85) is

$$\mathit{\Phi}_n^p(\xi) = \sqrt{2}Cos\left(\kappa_n^p(\xi - l/2)\right) \tag{88}$$

For this final expression $a_n^p = \sqrt{2}$ can be obtained from the orthonormality condition [12]:

$$\int_{-l/2}^{l/2} \varPhi_n^p(\xi)\varPhi_{n'}^q(\xi)d\xi = l\delta_{nn'} \tag{89}$$

The first 3 modes of oscillation are presented bellow:

$$\varPhi_0^p(\xi) = 1 \tag{90}$$

$$\varPhi_1^p(\xi) = \sqrt{2}Cos\left(\frac{\pi}{l}(\xi - l/2)\right) \tag{91}$$

$$\varPhi_2^p(\xi) = \sqrt{2}Cos\left(\frac{2\pi}{l}(\xi - l/2)\right) \tag{92}$$

The uniform mode $n = 0$ will be referred as the ferromagnetic resonance mode (FMR), while the modes $n = 1, 2, ...$ will be referred as the perpendicular standing wave modes n (PSSWn). Their profiles are sketched in Figure 7.

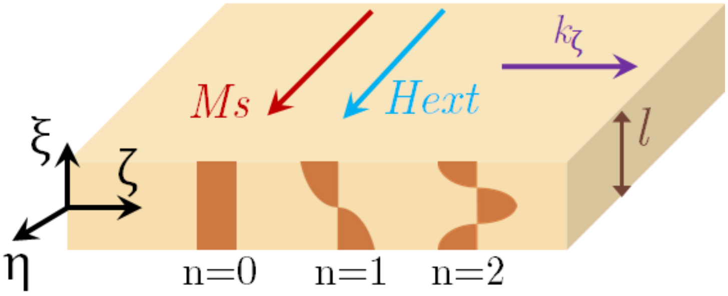

Figure 7: Spin wave modes sketched across the film thickness

3.4 General dispersion relation: Perturbation theory approach

To determine the dispersion relation for the spin wave in equation (57), the infinite series expression (78) for the variable magnetization is replaced in equation (75).

$$\sum_{n=0}^{\infty}\left\{\left[\hat{R}+\hat{T}\right]\left[m_n^x\vec{S}_n^x(\xi)+m_n^y\vec{S}_n^y(\xi)\right] - \int_{-l/2}^{l/2}\hat{G}_{xy}(\xi,\xi')\left[m_n^x\vec{S}_n^x(\xi')+m_n^y\vec{S}_n^y(\xi')\right]d\xi'\right\} = 0 \tag{93}$$

After applying the matrix operators to the series expansion, they are projected over the SWM to obtain the operators in this base [12]. After this projection, the field equation (75) can be written in the base of the SWM, and therefore one obtain a more compact form:

$$\sum_{n=0}^{\infty}\left[\bar{\hat{R}}+\bar{\hat{T}}+\bar{\hat{G}}\right]\vec{m}_n=0 \tag{94}$$

This projection reflects the effect that each operator has on the different modes due to their non-uniformity, and as will be seen, leads to interaction between different modes. The development of the projection is presented in Appendix C. The bar over the operators denote that they are expressed in the SMW base, and the amplitude vector for the mode n in the SWM base is:

$$\vec{m}_n=(m_n^x,m_n^y) \tag{95}$$

After grouping the corresponding terms in (94), because of the orthogonality of the SMW, for each mode n it can be written as (see Appendix C for a explicit form):

$$\hat{D}_{nn}\vec{m}_n+\sum_{n'\neq n}^{\infty}\hat{J}_{nn'}\vec{m}_{n'}=0 \tag{96}$$

To obtain a diagonal matrix for equation (96), the transformation $\left(det\hat{D}_{nn}\right)\hat{D}_{nn}^{-1}$ is applied, leading to:

$$\hat{H}_{nn}\vec{m}_n+\sum_{n'\neq n}^{\infty}\hat{W}_{nn'}\vec{m}_{n'}=0 \tag{97}$$

With the matrices defined by

$$\hat{H}_{nn}=\left(det\hat{D}_{nn}\right)\hat{D}_{nn}^{-1}\hat{D}_{nn} \tag{98}$$

$$\hat{W}_{nn'}=\left(det\hat{D}_{nn}\right)\hat{D}_{nn}^{-1}\hat{J}_{nn'} \tag{99}$$

Now an infinite system is constructed with all the n systems in (97).

$$\hat{\mathfrak{L}}\vec{m}_{\infty}=0 \tag{100}$$

The operator $\hat{\mathfrak{L}}$ acts on the infinite vector of amplitudes $\vec{m}_{\infty}$. Their respective expressions are:

$$\overline{\mathfrak{L}} = \begin{bmatrix} \overline{H}_{00} & & & & \\ & \overline{H}_{11} & & 0 & \\ & & \cdot & & \\ & & & \cdot & \\ & & & & \cdot \\ & 0 & & & \overline{H}_{nn} \\ & & & & & \cdot \end{bmatrix} + \begin{bmatrix} 0 & & & & \\ & 0 & & & \overline{W}_{nn'} \\ & & \cdot & & \\ & & & \cdot & \\ & & & & \cdot \\ & \overline{W}_{n'n} & & & 0 \\ & & & & & \cdot \end{bmatrix} \tag{101}$$

$$\vec{m}_{\infty} = (\vec{m}_0, \vec{m}_1, ..., \vec{m}_n, ...) \tag{102}$$

From (101), finding the dispersion relations for the spin wave modes implies finding the "eigenvalues" matrices blocks $\overline{\lambda}_n$, i.e. diagonalizing $\hat{\mathfrak{L}}$

$$\hat{\mathfrak{L}} = \begin{bmatrix} \overline{\lambda}_0 & & & & \\ & \overline{\lambda}_1 & & 0 & \\ & & \cdot & & \\ & & & \cdot & \\ & & & & \cdot \\ & 0 & & & \overline{\lambda}_n \\ & & & & & \cdot \end{bmatrix} \tag{103}$$

which implies that the dispersion equation for the spin wave mode n is found by solving:

$$det\left(\overline{\lambda}_n\right) = 0 \tag{104}$$

Now, since$\overline{\mathfrak{L}}$ is separated as a sum of a diagonal and a non-diagonal blocks, the diagonal part can be considered as an unperturbed operator while the non-diagonal one is considered as a perturbation [12]. As it will be seen, the diagonal part gives the approximate dispersion relations (without interaction), while the non-diagonal part contains corrections to the dispersion relations which are given by interactions between the different modes [12].

Following perturbation theory approach, the eigenvalue matrices of $\overline{\mathfrak{L}}$ can be expressed as a sum of different order corrections

$$\overline{\lambda}_n = {}^{(0)}\overline{\lambda}_n + {}^{(1)}\overline{\lambda}_n + {}^{(2)}\overline{\lambda}_n + ... \tag{105}$$

From perturbation theory formalism, the first order approximation gives the same result than the zero order one because of the form of the perturbation operator in equation (101), i.e. ${}^{(1)}\overline{\lambda}_n = \overline{0}$. For the present analysis corrections up to first order will be considered (no interactions), implying the dispersion relation for the mode n can be calculated as:

$$ {}^{(0)}\overline{\lambda}_n = det\left(\overline{H}_{nn}\right) = det(\overline{D}_{nn}) = 0 \tag{106} $$

Expanding this equation with the calculation performed in Appendix B, one obtains:

$$ 0 = \left[R^{xx}_{nn} + \bar{T}^{xx}_{nn} + AP^{xx}_{nn} + Sin^2\theta\right]\left[R^{yy}_{nn} + \bar{T}^{yy}_{nn} + EP^{yy}_{nn}\right] $$

$$ -\left[i\left(\frac{\omega}{\omega_M}\bar{T}^{yx*}_{nn} + DQ^{yx}_{nn}\right) + \bar{T}^{yx}_{nn} + CP^{yx}_{nn}\right]\left[-i\left(\frac{\omega}{\omega_M}\bar{T}^{xy*}_{nn} - DQ^{xy}_{nn}\right) + \bar{T}^{xy}_{nn} + CP^{xy}_{nn}\right] \tag{107} $$

From the definition of $\overline{H}_{nn}$, it is also clear that the amplitude vector, up to zero order, is

$$ {}^{(0)}\vec{m}_n = (1, 1) \tag{108} $$

Therefore, recalling equation (78), the the variable magnetization up to zero order is:

$$ \vec{m}(\xi) = M_s \sum_{n=0}^{\infty} \left(\varPhi^x_n(\xi), \varPhi^y_n(\xi)\right) \tag{109} $$

3.5 Dispersion relations for uniform (FMR) and perpendicular standing spin wave modes

The derivation of (107) was performed as an instructive procedure and as a future reference for other applications. Now, the very general expression for the SWM dispersion relation (107) has to be adapted for the experimental measurements to be performed. For the particular experimentation, that is described later in this manuscript, the following is considered:

- No propagation of spin waves is produced, therefore $k_\zeta = 0$.
- The magnetic moments are unpinned at the surfaces of the film.
- There are no interaction between different modes of oscillation.
- There are two types of anisotropies: bulk uniaxial anisotropy and uniaxial surface anisotropy.

The fact that $k_\zeta = 0$ automatically implies that the Green's tensor components become zero $G_P = G_Q = 0$, and therefore $P^{pq}_{nn} = P^{pq}_{nn'} = Q^{pq}_{nn} = Q^{pq}_{nn'} = 0$ (see Appendix B). The unpinned condition for the moments was already applied in equation (86), it allowed to determine the standing spin wave numbers $\kappa_n^p = n\frac{\pi}{l}$. Note the form of the dispersion relation (107) is independent of the pinning conditions, and therefore is the same for different κ_n^p. The condition for no interaction between two different modes was also already considered when the dispersion relation was obtained up to first order in equation (106). This simplifications leads to a more simplified expression for (107):

$$f_n = \frac{\omega_M}{2\pi}\left[\left(R_{nn}^{xx} + Sin^2\theta + \bar{T}_{nn}^{xx}\right)\left(R_{nn}^{yy} + \bar{T}_{nn}^{yy}\right)\right]^{1/2} \tag{110}$$

The last condition implies that the general form of the anisotropy tensor (70) needs to be replaced by a specific form accounting just these two types of anisotropies. From Appendix C, the only surviving component of matrix $\bar{\bar{T}}$ is $\bar{T}_{nn}^{xx}$. The coefficients R_{nn}^{pp} are explicitly calculated in Appendix C for each mode..

The following fields are defined to simplify the notation in Appendix D:

$$H_{Ex}^{'} = \frac{2A\pi^2}{\mu_o M_s l^2}, \quad H_{Ku}^{'} = \frac{2K_u}{\mu_o M_s}, \quad H_S^{'} = \frac{2K_S}{\mu_o M_s l} \tag{111}$$

Now, the measurements were performed with the external static field in- and out-of-plane of the film. The configurations of interest are then: θ=$\frac{\pi}{2}$ for the in-plane M_s (denoted by the symbol $||$) and θ=0 for the out-of-plane M_s (denoted by the symbol $\perp$).

- When $\theta = \varphi$=$\frac{\pi}{2}$:

M_s is in the plane, because of equation (10) there is no demagnetizing field, and from equations (197-198) (see Appendix C) there is no static anisotropy field either. The only static field is the externally applied field (see Appendix D):

$$H_i = H_{ext} \tag{112}$$

For the uniform $n = 0$ (FMR) mode (see Appendix C for $\bar{T}_{00}^{xx}$):

$$f_{0||} = \frac{\gamma\mu_o}{2\pi}\left[(H_{ext})\left(H_{ext} + M_s - H_{Ku}^{'} - H_S^{'}\right)\right]^{1/2} \tag{113}$$

For the non-uniform $n = 1$ (PSSW1) mode:

$$f_{1||} = \frac{\gamma\mu_o}{2\pi}\left[\left(H_{ext} + H_{Ex}^{'}\right)\left(H_{ext} + H_{Ex}^{'} + M_s - H_{Ku}^{'} - 2H_S^{'}\right)\right]^{1/2} \tag{114}$$

- When θ=0:

M_s is out of the plane, because of equation (10) the demagnetizing field is $\vec{H_{de}}$= $-\vec{M_s}$, and from equations (197-198) (see Appendix C) there is a static anisotropy field too. The internal static field is

$$H_i = H_{ext} - M_s + H^{'}_{Ku} + H^{'}_{S} \tag{115}$$

In equation (115) the surface anisotropy term is included after an average of the $\vec{H}_S$ field along the thickness of the film.

For the uniform $n = 0$ (FMR) mode (see Appendix C for $\bar{T}^{xx}_{00}$):

$$f_{0\perp} = \frac{\gamma\mu_o}{2\pi}\left(H_{ext} - M_s + H^{'}_{Ku} + H^{'}_{S}\right) \tag{116}$$

For the non-uniform $n = 1$ (PSSW1) mode (see Appendix C for $\bar{T}^{xx}_{11}$):

$$f_{1\perp} = \frac{\gamma\mu_o}{2\pi}\left(H_{ext} - M_s + H^{'}_{Ex} + H^{'}_{Ku} + 2H^{'}_{S}\right) \tag{117}$$

Equations (113,114,116,117) are the dispersion relations for the modes of oscillation that will be measured via network analyzer FMR which will be explained in the next chapter.

Higher modes, e.g. n=2, cannot be measured because they are out of the working frequency and field ranges of the experimental set up. Nevertheless, note that for higher modes the only change needs to be done in the exchange contribution. The dispersion relations for any $n \neq 0$ are:

$$f_{n\|} = \frac{\gamma\mu_o}{2\pi}\left[\left(H_{ext} + n^2 H^{'}_{Ex}\right)\left(H_{ext} + n^2 H^{'}_{Ex} + M_s - H^{'}_{Ku} - 2H^{'}_{S}\right)\right]^{1/2} \tag{118}$$

$$f_{n\perp} = \frac{\gamma\mu_o}{2\pi}\left(H_{ext} - M_s + n^2 H^{'}_{Ex} + H^{'}_{Ku} + 2H^{'}_{S}\right) \tag{119}$$

One thing to be remarked from Appendix D is that the internal static field has a different effect on the different modes of oscillation since it has a non-uniform component (surface anisotropy) across the thickness.

4 Vector network analyzer ferromagnetic resonance

In order to probe the magnetization dynamics of different ferromagnetic samples, the technique of Vector Network Analyzer Ferromagnetic Resonance was used. In this technique, the sample is subjected to a high frequency field, created by a microwave source in a Vector Network Analyzer, while an electromagnet sweeps a external magnetic field. During this process, the magnitude and phase of the power reflected and transmitted in the circuit (waveguide with ferromagnetic sample on top) are measured. From this power absorption, information on the magnetic properties of the sample can be derived by the model presented in the previous section. The complete system is set to a usual characteristic impedance of 50 Ω.

4.1 Experimental set up

The experimental setup consist of a microwave network that allows to measure the response of the samples under study via VNA and a electromagnet with a Hall probe connected to a gaussmeter to produce the desired external magnetic field and measure it. All the parts of the setup are connected to a computer that controls them via virtual interface. An air conditioning system controls the temperature of the room which was set to 25 °C. The setup is represented on Figure 8.

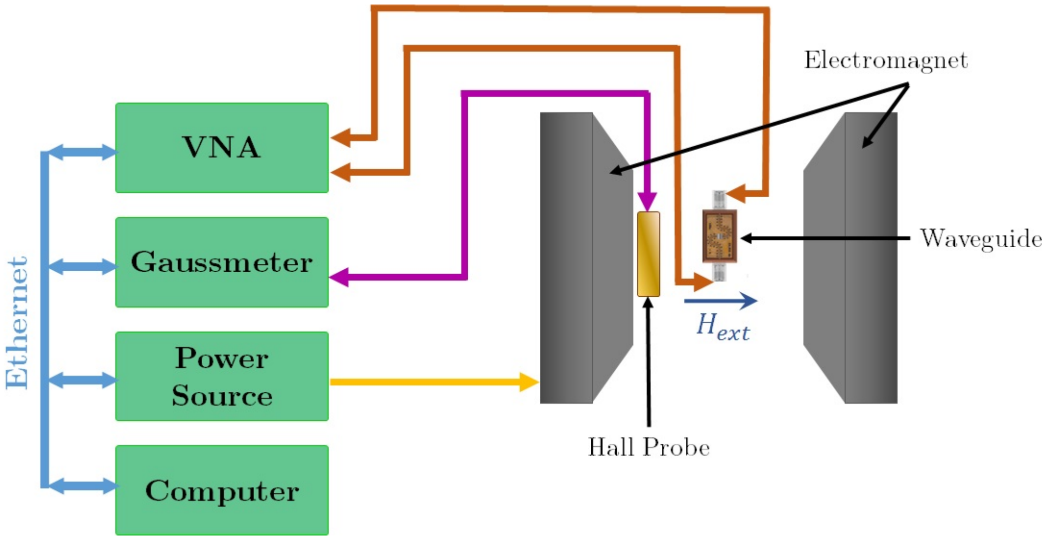

Figure 8: Setup's components representation

4.1.1 Microwave network

The VNA is connected to a brass box with 2.9 mm connectors through flexible and semi rigid cables specified to high frequency (air as dielectric). The cables allow to reach the box that is fixed to a pole which hangs from a tunable angle support. The waveguide is inserted in this box so that the signal track is in contact with the microwave probes of the connectors and the rest of the board in contact to the grounded box (see Figure 9). Once the waveguide is in position inside the box, it is closed by two brass pieces and non-magnetic bolts. The box has a conduct to reach the central part of the track from the exterior. The central track consist of a 200 μm width constriction.

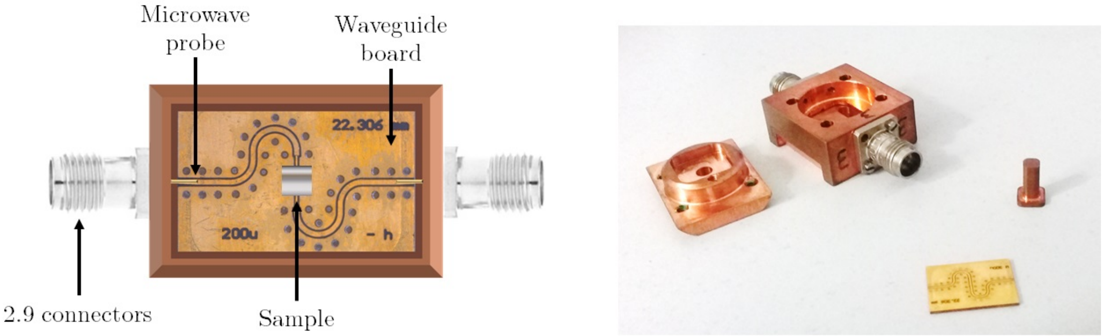

Figure 9: Brass box with waveguide board and connectors

A brass podium with a 3×3 mm head is inserted in this conduct with the sample on top so it can reaches the excitation track. The samples are normally cut in 2×2 mm squares and attached to the podium with adhesive. In special cases the samples could be fastened directly to the board before closing the box (see Figure 10).

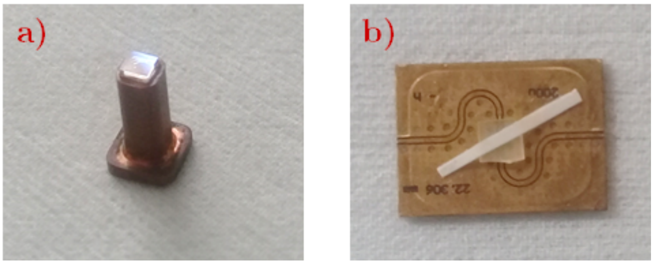

Figure 10: Sample fixation: a) Using the podium (inserted in box), b) Fixating directly on the board

4.1.2 Magnet control

The electromagnet used to create the external field, that was considered in Chapters 2 and 3, has a resistance around 3 Ω. The gap between the two poles of the magnet is variable with a maximum of 42 mm. It is connected to a power supply which can produce a field of 2.3 T with the 42 mm gap (used for in-plane measurements) and a field of 2.7 T with a gap of 22 mm (used for out-of-plane measurements). The magnet is on a bearing support with 360^o rotation that allows to perform in- and out-of-plane measurements around the pole and fixed box. A Hall probe measures the magnetic field and is connected to a gaussmeter and power source for control. The Hall probe has also two possible positions depending on the type of measurement being done. This change of position is accounted in the final measured value of the field. For temperature control the electromagnet receives a constant flow of water driven by a pump located in a separate room.

4.2 Preliminary VNA notions

The power absorption of the ferromagnetic resonance is obtained by measuring the S-parameters of the waveguide board with the ferromagnetic samples. A sketch of the network (VNA, waveguide, connectors and cables) is shown in Figure 11.

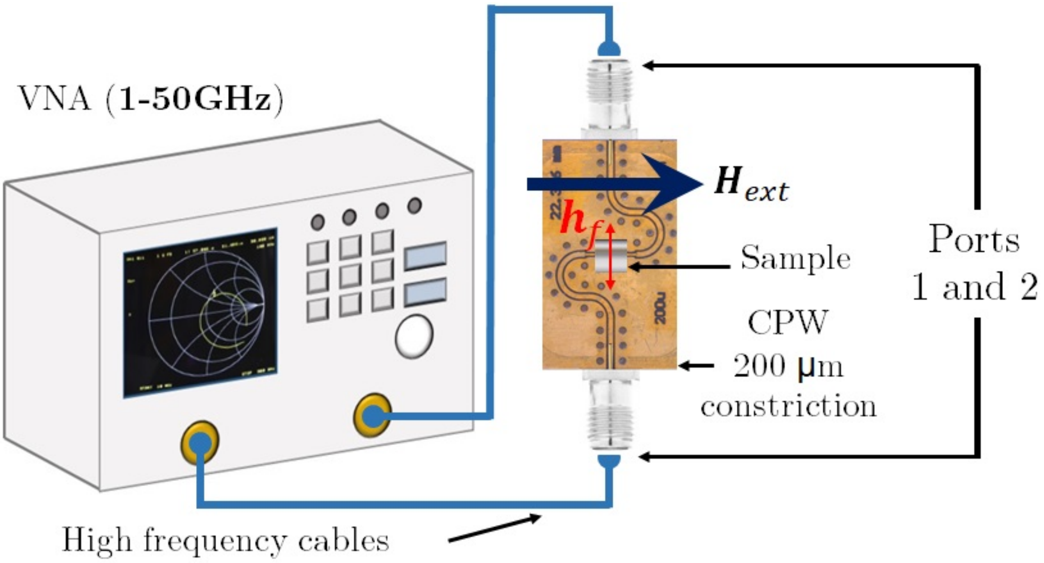

Figure 11: VNA connected to board for in-plane field configuration

4.2.1 Scattering parameters

These quantities, also called S-parameters, relate the incident and reflected electromagnetic waves in linear electrical networks. In general, it is possible to determine the scattering matrix for a n-port device, but the network components that are used in this case just have two terminals, therefore the 2-port treatment will be implemented. A sketch of a 2 port component is presented in Figure 12.

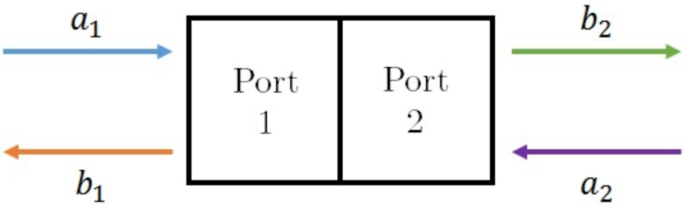

Figure 12: 2-port generic component

The complex normalized waves for i=1, 2 are given by:

$$a_i = \frac{V_i + Z_{ci} I_i}{2\sqrt{Z_{ci}}} \qquad b_i = \frac{V_i - Z_{ci} I_i}{2\sqrt{Z_{ci}}} \tag{120}$$

where a$_i$ is the incident wave, b_i is the outgoing wave and Z_{ci} is the characteristic impedance on the port i. This is clear after replacing the following solutions for the telegrapher's equations [11]:

$$V(x) = Ae^{-\gamma x} + Be^{\gamma x} \tag{121}$$

$$I(x) = Ce^{-\gamma x} + De^{\gamma x} \tag{122}$$

into (120). Here A, B, C, D are constants and γ is called the propagation constant (different from the γ introduced in Chapters 2 and 3). By doing this, the following expressions can be obtained for the incident and outgoing waves:

$$a_i = \frac{A}{Z_{ci}} e^{-\gamma x} \qquad b_i = \frac{B}{Z_{ci}} e^{\gamma x} \tag{123}$$

The scattering matrix S is defined by the following equation relating the outgoing waves to the incident ones

$$\begin{pmatrix} b_1 \\ b_2 \end{pmatrix} = \hat{S} \begin{pmatrix} a_1 \\ a_2 \end{pmatrix} = \begin{bmatrix} S_{11} & S_{12} \\ S_{21} & S_{22} \end{bmatrix} \begin{pmatrix} a_1 \\ a_2 \end{pmatrix} \tag{124}$$

where each scattering parameter S_{ij} is the ratio between the outgoing wave at port i and the incident wave at port j when no other port receives signal. A device is reciprocal if $S_{12} = S_{21}$ and is symmetric if $S_{11} = S_{22}$.

In a real network multiple devices need to be connected after each other. This can be accounted by the multiplication of their transmission matrices $\hat{T}$ [11]:

$$\hat{T} = \begin{bmatrix} T_{11} & T_{12} \\ T_{21} & T_{22} \end{bmatrix} = \begin{bmatrix} \frac{S_{12}S_{21}-S_{11}S_{22}}{S_{21}} & \frac{S_{11}}{S_{21}} \\ -\frac{S_{22}}{S_{21}} & \frac{1}{S_{21}} \end{bmatrix} \tag{125}$$

Obviously the matrix $\hat{S}$ can be also be obtained from $\hat{T}$:

$$\hat{S} = \begin{bmatrix} \frac{T_{12}}{T_{22}} & \frac{T_{11}T_{22}-T_{12}T_{21}}{T_{22}} \\ \frac{1}{T_{22}} & -\frac{T_{12}}{T_{22}} \end{bmatrix} \tag{126}$$

4.2.2 Actual device

The used VNA was an Agilent PNA N5225A-201 with a working frequency range of 10 MHz-50 GHz. Its internal microwave source can provide a signal fixed at some frequency f between the mentioned range. This type of device is different to spectrum analyzer in the sense that it is able to produce phase sensible measurements. It allows to obtain the real and imaginary part of the S-parameters, and as it will be shown, the complex magnetic susceptibility.

To obtain sensible and precise results, the VNA must go through a calibration process. On one hand, any contribution from cables, connectors and probes that connect the VNA to the actual waveguide (device being measured) have to be eliminated. Also errors on the device itself need to be accounted in order to have a cleaner signal from the waveguide. All these errors, called systematic, are assumed to be invariant with time and therefore can be corrected by a calibration process [19]. Other errors that occur during the operation time, manly because of instrument noise, are called random and cannot be corrected by calibration.

In this particular case, a customized TRL (Thru, Reflect, Line) calibration kit with five standard circuits was used: a thru, a short or reflect, and 3 lines with different lengths. Normally the thru standard is the shortest of the lines, but in this case it was not. Each circuit is connected to the VNA and measured in both directions. The calibration data is saved to be used before each measurement. It is important to perform usual calibrations since the state of the set up can change appreciably with time. Fortunately, the used set up temperature was controlled by air conditioning system which prevents the introduction of important drift errors (errors after calibration).

4.3 Two port data evaluation

The VNA provides raw data of the already explained microwave network (S-parameters). This data has to be treated in order to obtain the necessary information about the sample under study that allows one to use the theory on Chapter 3 to get access to its magnetic properties. This subsection is based on Bilzer's data evaluation method [11].

4.3.1 Raw data

After calibration, the VNA measures the matrix S_N for the network between the two microwave probes (Figure 9) where several parts of it need to be taken into account separately. The parts to be considered are (see Figure 13): length d_1 from microwave probe to constriction (200 μm), change of impedance from Z_o to Z_1 at plane P_1, length d_2 from constriction to sample, change of impedance at plane P_2 from to Z_1 to Z (impedance under sample), sample's length d_3, change of impedance at plane P_3 back to Z_1, length d_4 from sample to end of constriction, change of impedance at plane P_4 back to Z_o, and length d_5 from end of constriction to probe.

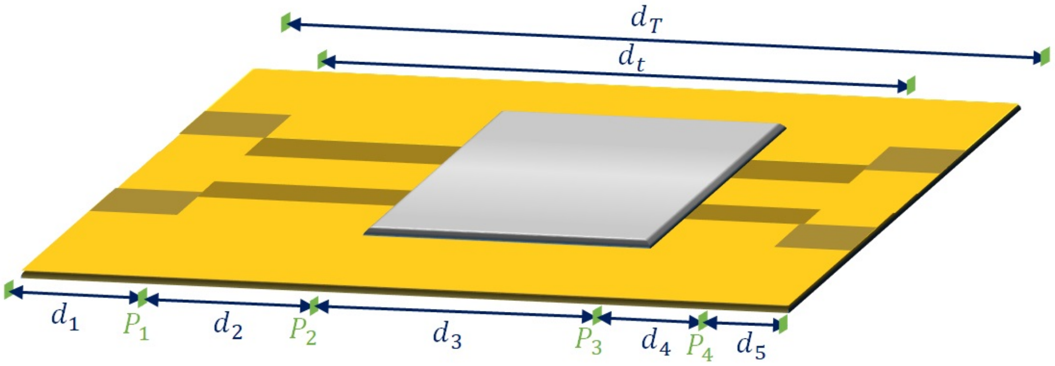

Figure 13: Board's division for microwave corrections

To get the matrix $\hat{S}$ for the network, the transmission matrices for each part in Figure 13 are multiplied (from left to right) and the total matrix $\hat{T}$ is obtained [11]:

$$\hat{T} = \begin{bmatrix} e^{-\gamma_o d_1} & 0 \\ 0 & e^{\gamma_o d_1} \end{bmatrix} \begin{bmatrix} \frac{1}{\sqrt{1-\varGamma_1^2}} & \frac{\Gamma_1}{\sqrt{1-\varGamma_1^2}} \\ \frac{\Gamma_1}{\sqrt{1-\varGamma_1^2}} & \frac{1}{\sqrt{1-\varGamma_1^2}} \end{bmatrix} \begin{bmatrix} e^{-\gamma_1 d_2} & 0 \\ 0 & e^{\gamma_1 d_2} \end{bmatrix}$$

$$\times \begin{bmatrix} \frac{1}{\sqrt{1-\varGamma^2}} & \frac{\Gamma}{\sqrt{1-\varGamma^2}} \\ \frac{\Gamma}{\sqrt{1-\varGamma^2}} & \frac{1}{\sqrt{1-\varGamma^2}} \end{bmatrix} \begin{bmatrix} e^{-\gamma d_3} & 0 \\ 0 & e^{\gamma d_3} \end{bmatrix} \begin{bmatrix} \frac{1}{\sqrt{1-\varGamma^2}} & \frac{-\Gamma}{\sqrt{1-\varGamma^2}} \\ \frac{-\Gamma}{\sqrt{1-\varGamma^2}} & \frac{1}{\sqrt{1-\varGamma^2}} \end{bmatrix} \begin{bmatrix} e^{-\gamma_1 d_4} & 0 \\ 0 & e^{\gamma_1 d_4} \end{bmatrix}$$

$$\times \begin{bmatrix} e^{-\gamma_1 d_4} & 0 \\ 0 & e^{\gamma_1 d_4} \end{bmatrix} \begin{bmatrix} \frac{1}{\sqrt{1-\varGamma_1^2}} & \frac{-\Gamma_1}{\sqrt{1-\varGamma_1^2}} \\ \frac{-\Gamma_1}{\sqrt{1-\varGamma_1^2}} & \frac{1}{\sqrt{1-\varGamma_1^2}} \end{bmatrix} \begin{bmatrix} e^{-\gamma_o d_5} & 0 \\ 0 & e^{\gamma_o d_5} \end{bmatrix} \tag{127}$$

where

$$\Gamma_1 = \frac{Z_1 - Z_o}{Z_1 + Z_o}, \quad \Gamma = \frac{Z - Z_1}{Z + Z_1} \tag{128}$$

are the complex reflection coefficients for the planes P_1 and P_2 respectively.

γ_o is the propagation constant on the waveguide in the unconstricted part, $\gamma_1$is the propagating constant in the free constricted part, and γ is the propagation constant on the portion covered by the sample.

From (127), it is clear that the transmission matrix for the constricted part between planes $P_1$and P_4 is

$$\hat{T}^{1\bar{4}} = \begin{bmatrix} e^{-\gamma_1 d_2} & 0 \\ 0 & e^{\gamma_1 d_2} \end{bmatrix} \begin{bmatrix} \frac{1}{\sqrt{1-\varGamma^2}} & \frac{\Gamma}{\sqrt{1-\varGamma^2}} \\ \frac{\Gamma}{\sqrt{1-\varGamma^2}} & \frac{1}{\sqrt{1-\varGamma^2}} \end{bmatrix} \begin{bmatrix} e^{-\gamma d_3} & 0 \\ 0 & e^{\gamma d_3} \end{bmatrix}$$
$$\times \begin{bmatrix} \frac{1}{\sqrt{1-\varGamma^2}} & \frac{-\Gamma}{\sqrt{1-\varGamma^2}} \\ \frac{-\Gamma}{\sqrt{1-\varGamma^2}} & \frac{1}{\sqrt{1-\varGamma^2}} \end{bmatrix} \begin{bmatrix} e^{-\gamma_1 d_4} & 0 \\ 0 & e^{\gamma_1 d_4} \end{bmatrix} \tag{129}$$

Then, this transmision matrix can be transformed into $\hat{S}_{\overline{14}}$ by equation (126) obtaining [11]:

$$\hat{S}^{\overline{14}} = \begin{bmatrix} e^{-\gamma_1 2 d_2} \frac{\Gamma(1-P^2)}{1-P^2\Gamma^2} & e^{-\gamma_1 (d_2+d_4)} \frac{P(1-\Gamma^2)}{1-P^2\Gamma^2} \\ e^{-\gamma_1 (d_2+d_4)} \frac{P(1-\Gamma^2)}{1-P^2\Gamma^2} & e^{-\gamma_1 2 d_4} \frac{\Gamma(1-P^2)}{1-P^2\Gamma^2} \end{bmatrix} \tag{130}$$

where the P coefficient is defined as

$$P = e^{-\gamma d_3} \tag{131}$$

The following subsections explain corrections to be performed to the matrix $\hat{S}_{\overline{14}}$ to isolate the real response from the ferromagnetic material. Note that this requires the S-parameters to be known at the planes P_1 and P_2, but the VNA measure them at both ends of the unconstricted track (Figure 11). These measured S-parameters can be obtained by transforming $\hat{T}$, of equation (127), into $\hat{S}$. This is a intricate calculation that is performed in the program that controls the virtual interface and isn't shown in this manuscript.

4.3.2 Sample's position correction

From equation (130), it is clear that $S_{12}^{\overline{14}} = S_{21}^{\overline{14}}$ (reciprocal device) are both independent of the sample's position, but $S_{11}^{\overline{14}}$ and $S_{22}^{\overline{14}}$ are not. Since the sample cannot be placed exactly in the middle of the track and d_2 and d_4 are not easy to measure, a mathematical correction is introduced in order to solve the problem. A geometric mean of the two problematic parameters is used instead:

$$S_{11}^{\overline{14}*} = S_{22}^{\overline{14}*} = \sqrt{S_{11}^{\overline{14}} S_{22}^{\overline{14}}} = e^{-\gamma_1(d_2+d_4)} \frac{\Gamma(1-P^2)}{1-P^2\Gamma^2} \tag{132}$$

In this way the scattering matrix becomes symmetrical and $d_2 + d_4 = d_t - d_3$ is just the constricted track length minus the sample length, a well known quantity.

4.3.3 De embedding

Now, the data needs to be corrected so the portion of waveguide without sample does not contribute to the measurements and the spectra represents just the sample alone. To do this, $S_{12}^{\overline{14}} = S_{21}^{\overline{14}}$ and $S_{11}^{\overline{14}*} = S_{22}^{\overline{14}*}$ needs to be multiplied by the inverse of the factor $e^{-\gamma_1(d_2+d_4)}$ [11]. Here, γ_1 is still unknown but can be obtained by measuring $S_{21_o}^{\overline{14}}$ (without sample). This is just a line of length d_t and impedance Z$_1$. Since $S_{21_o}^{\overline{14}} = e^{-\gamma_1 d_t}$ all the quantities are known, and the needed factor can be calculated by:

$$\left(e^{-\gamma_1(d_2+d_4)}\right)^{-1} = e^{-\frac{d_2+d_4}{d_t} ln\left(S_{21_o}^{\overline{14}}\right)} \tag{133}$$

After the multiplication of the S-parameters by the previous factor, one has access to the quantities:

$$S_{11}^{\overline{14}*B} = S_{22}^{\overline{14}*B} = \frac{\Gamma(1-P^2)}{1-P^2\Gamma^2} \tag{134}$$

$$S_{12}^{\overline{14}B} = S_{21}^{\overline{14}B} = \frac{P(1-\Gamma^2)}{1-P^2\Gamma^2} \tag{135}$$

4.3.4 Calculation of Γ and γ

Analytically, the following expression can be obtained for Γ [11]:

$$\Gamma = D \pm \sqrt{D^2 - 1} \tag{136}$$

The sign for equation (127) is chosen in order to have $|\Gamma| < 1$. D can be calculated like:

$$D = \frac{1 + \left(S_{11}^{\overline{14}*B}\right)^2 - \left(S_{21}^{\overline{14}B}\right)^2}{2S_{11}^{\overline{14}*B}} \tag{137}$$

P, from equation (131), is also equal to:

$$P = \frac{S_{11}^{\overline{14}*B} + S_{21}^{\overline{14}B} - \Gamma}{1 - (S_{11}^{\overline{14}*B} + S_{21}^{\overline{14}B})\Gamma} \tag{138}$$

which allows to calculate the propagation constant γ by:

$$Re(\gamma) = -\frac{ln(|P|)}{d_3} \qquad Im(\gamma) = -\frac{arg(P)}{d_3} \tag{139}$$

Here caution is recommended in order to evaluate P because, being a complex number, its logarithm can be multivalued.

4.3.5 Field shielding

Normally the films to be characterized by CPW-FMR are made of conducting material. The interaction of the microwave field with the conductor film can induce some electromagnetic field on it that would modify the total field near the sample. The concentration of the electromagnetic field between the CPW track and the film itself is called shielding. This is produced by the conducting film trying to cancel the field on top of it by creating an opposite field to the one in the CPW. This is the phenomena responsible for the creation of eddy currents on the conducting ferromagnetic film which lead to non-uniform oscillation of the magnetization. In this way the standing spin wave modes, obtained in Chapter 3, are exited.

It has been shown that less resistive films (closer to a perfect grounded conductor) are better at shielding the electromagnetic field between the CPW track and the film itself [23]. The more resistive a film is, the less important its effect is, and the less shielded the electromagnetic field. This implies that the shielding effect allows to excite PSSW modes instead of just the uniform mode (see Chapter 3)[23].

The shielding modifies also the measured FMR signal by a change of inductance δL which is inversely proportional to the width w of the CPW's track [23]. Therefore, this can be corrected by contracting the portion of the track under the film in order to reduce δL. This is the reason why the experimental CPW has a 200 μm constriction. These type of CPW engineering and de embedding procedures has to be used in order to extract via inductive VNA-FMR the actual magnetic response of conductive films.

4.3.6 Obtaining $\tilde{\varepsilon}_r$ and $\tilde{\mu}_r$

The waveguide will be considered to be in a effective material with effective relative permittivity $\tilde{\varepsilon}_r$ and effective relative permeability $\tilde{\mu}_r$. This is considered since there are several different media that contribute to these parameters: air, sample, waveguide itself, etc.. The two can be extracted from the following equations:

$$\frac{\gamma}{\gamma_{\text{fs}}} = \frac{\gamma}{i2\pi f\sqrt{\mu_o\varepsilon_o}} \tag{140}$$

$$\frac{1+\Gamma}{1-\Gamma} = \frac{Z}{Z_o} = G\sqrt{\frac{\tilde{\mu}_r}{\tilde{\varepsilon}_r}} \tag{141}$$

where $\gamma_{\mathrm{f}s}$ is the propagation constant of free space and G is a constant that depends on the air space between the sample and the waveguide. Since G is difficult to estimate, just proportional quantities are calculated:

$$\tilde{\mu}_r \propto \frac{\gamma}{\gamma_{\mathrm{f}s}} \frac{1+\Gamma}{1-\Gamma} \tag{142}$$

$$\tilde{\varepsilon}_r \propto \frac{\gamma}{\gamma_{\mathrm{f}s}} \frac{1-\Gamma}{1+\Gamma} \tag{143}$$

Now, $\tilde{\varepsilon}_r$ is considered a constant since it does not change importantly over the frequency range. Then the permeability is accessible by considering equation (143) with $\tilde{\varepsilon}_r$ as a constant, i.e. $\frac{\gamma}{\gamma_{\mathrm{f}s}} \propto \frac{1+\Gamma}{1-\Gamma}$. With this the permeability can be calculated in two independent ways:

$$\tilde{\mu}_r \propto \left(\frac{1+\Gamma}{1-\Gamma}\right)^2 \qquad \tilde{\mu}_r \propto \left(\frac{\gamma}{\gamma_{\mathrm{f}s}}\right)^2 \tag{144}$$

Now considering that the magnetic susceptibility for the sample is:

$$\chi = \mu_r - 1 \tag{145}$$

where μ_r is the relative permeability for the sample alone, a proportional quantity to χ can be extracted by subtracting a reference from $\tilde{\mu}_r$. To do this, in the reference measurement the sample must not be exited. Such data can be obtained by applying the external field parallel to the excitation one. Finally a quantity proportional to the permeability of the sample alone, and therefore to its susceptibility, is obtained:

$$\chi \propto \tilde{\mu}_r - \tilde{\mu}_{rRef} \tag{146}$$

5 Results and discussion

FMR measurements were conducted on 5 different samples. The peculiarities of each measurements are presented with their corresponding results and discussion. After the treatment given to the raw data, that is explained in Chapter 3, the susceptibility is fitted by a complex Lorentzian (see equations (54-55)) from which one can obtain the resonance field, bandwidth and phase for each frequency. These spectra measurements are presented for each sample showing their FMR response. All the resonance frequency versus magnetic field measurements were fitted with equations (113,114,116,117) and then the magnetic quantities calculated. With measurements in- and out-of-plane, one cannot access directly the saturation magnetization, instead an effective magnetization can be measured:

$$M_{eff} = M_s - H'_{Ku} \tag{147}$$

Recalling the dispersion relations, this also implies that only estimations can be made for the calculations of the exchange and surface anisotropy constants. This quantities will be denoted by a $(^*)$. The constant K_u cannot be directly determined since it cannot be independently extracted from the dispersion relations.

For the line widths, a linear fit were performed and equation (56) used to obtain α.

5.1 CoFeB 40nm (5864)

A cobalt iron boron 40 nm thickness, 2mm×1.9mm surface area sample was measured to obtain a FMR characterization with special interest in its exchange constant. The constant value is to be used on simulations to test its viability as Permalloy's second constituent on a bilayer system aiming to exploit non reciprocity effects. The sample consist of a trilayer Ta(3)/CoFeB(40)/Au(3) grown by magnetron sputtering on a Si substrate (resistivity $> 20000\ \Omega cm$). It was provided by Michel Hehn (Institut Jean Lamour, Nancy, France).

5.1.1 Spectra

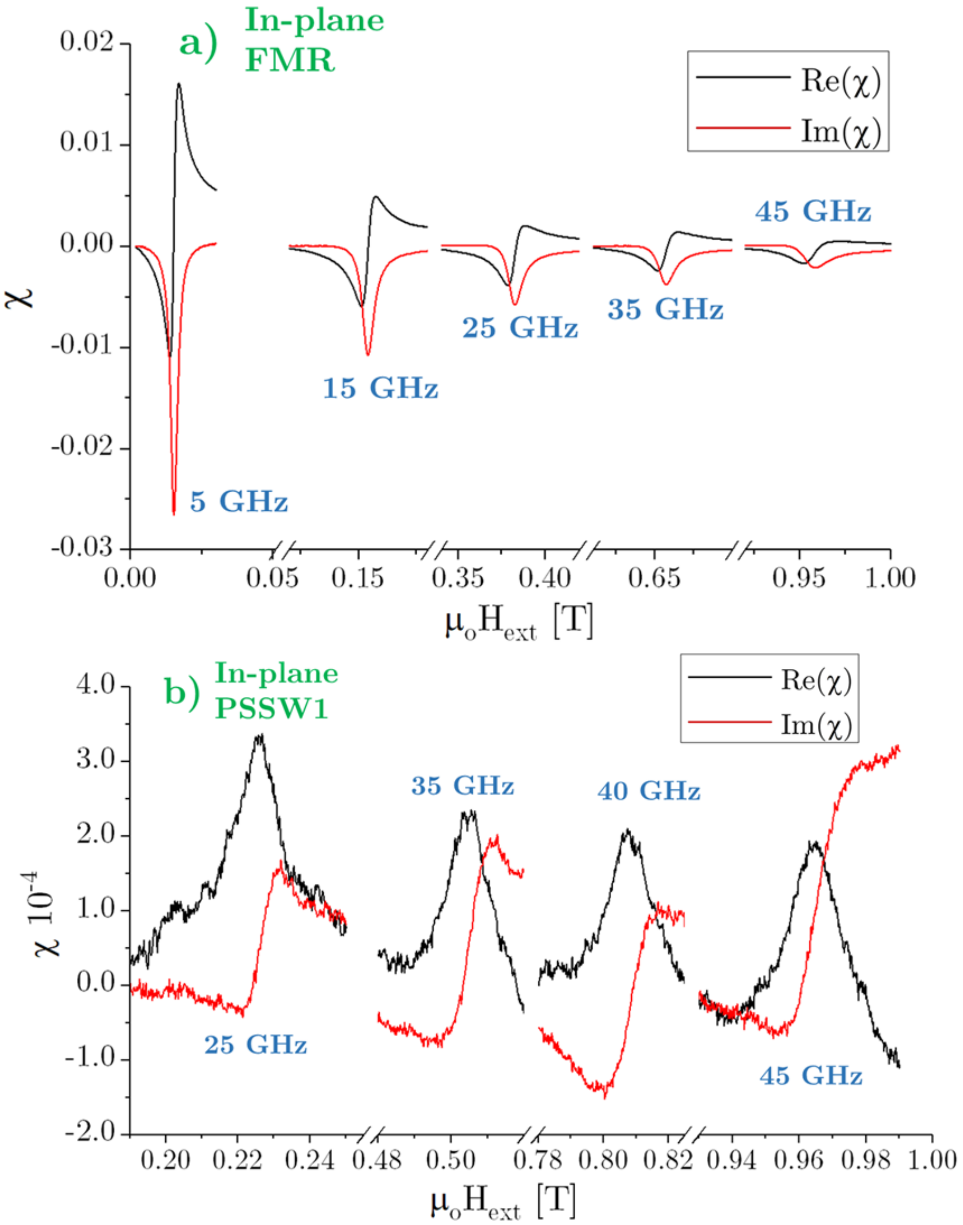

Figure 14: CoFeB: Resonance profiles for different frequencies in the in-plane configuration: a) FMR mode, b) PSSW1

Figure 14 presents resonance spectra for the in-plane configuration of the CoFeB sample. For the in-plane configuration the sample present normal resonance spectra for the

FMR mode ($n = 0$) on the complete frequency range. A progressive widening of the resonance peak is visible together with a reduction of the amplitude of the peak which is common in these types of measurements.

On the other hand, the PSSW1 mode shows an amplitude much smaller than the FMR mode, which is expected since the PSSW are higher order excitations that, for a given field, occur at higher frequency. There is also a phase mixing of $\pi/2$ between the real and imaginary part of the signal. This is produced because, as was explained in Chapter 4, the generation of the PSSW modes is given by eddy currents in the material. These currents have a different sign than the ones in the CPW in order to cancel the field (they have also a phase shift of $\pi/2$). Because of this, the excitation caused by this currents produce a phase shift in the signal measured by the VNA. The resonance field still contains the information of the sample resonance since all this inductive process happens when the resonance condition is achieved.

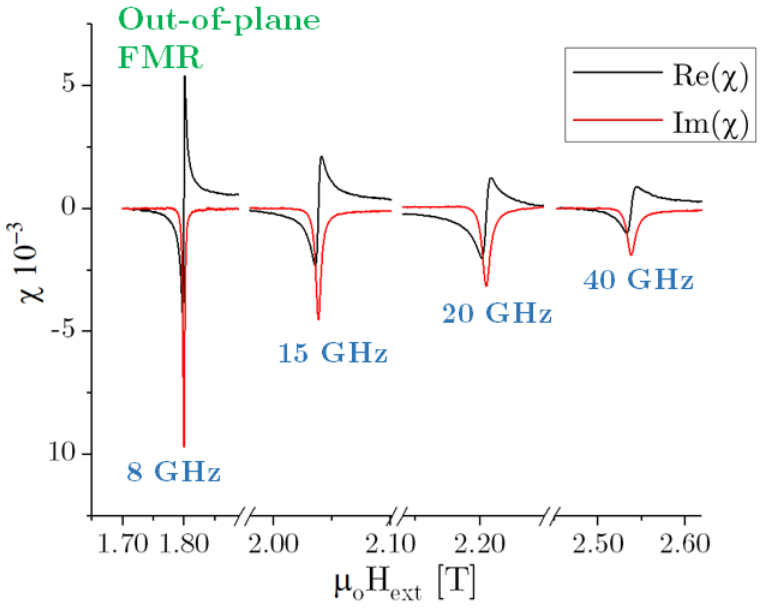

Figure 15: CoFeB: FMR mode resonance profiles for different frequencies in the out-of-plane configuration

In the out-of-plane configuration, the FMR mode has a similar profile to the in-plane one, of course at higher field. To estimate the resonance fields for the out-plane PSSW1 the raw data (S-parameters) had to be checked since the susceptibility did not shown any identifiable resonance profile. This leads to some error introduction since there are not corrections applied to the raw data directly obtained from the VNA.

5.1.2 Dispersion relations and magnetic parameters

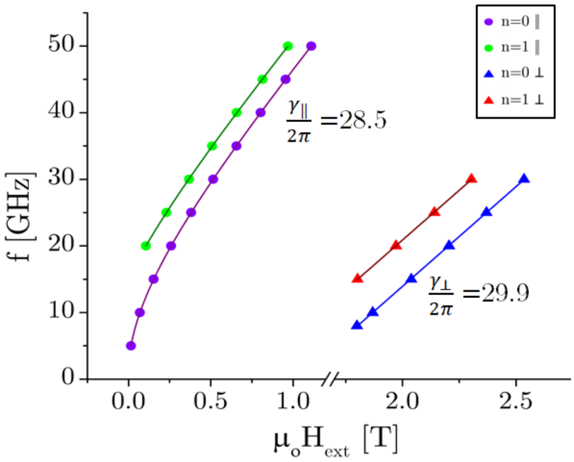

Figure 16: CoFeB: Fitted dispersion relations for FMR and PSSW1 modes in- and out-of-plane configurations

Despite the difficulties found to estimate the resonance fields, the data fits the model with good accuracy and comparing the calculated $\gamma's$ for the PSSW1 modes, both in and out-of-plane, shows that they do not differ significantly from the FMR modes.

From Figure 16 it is more evident that the PSSW1 modes (n=1) occur at higher frequency for a given field, therefore, they start to be measurable also at higher frequency. Other feature that is common, as will be seen, for all the samples is a larger γ measured out-of-plane than in-plane. The ratio between the two is $\frac{\gamma_{\parallel}}{\gamma_{\perp}} = 0.9$. This consistent increment could be related to the loss of symmetry for the oscillating component of the magnetization in the in-plane configuration. While for a film magnetized out-of-plane, the variables components of the magnetization are both in the plane, for the case of a film magnetized in the plane the x component oscillates out of it (see Figure 3). Recalling LL equation (18), γ is the proportionality constant between the actual rate of change of the magnetization and the torque produced by the magnetic field. The measurements indicate that more torque $\mu_o\vec{M} \times \vec{H_{eff}}$ is needed in the in-plane configuration than in the out-of-plane to achieve the same $\frac{\partial\vec{M}}{\partial t}$ rate of change of the magnetization.

From the fitted dispersion relations in Figure 16 the following parameters were obtained.

$\mu_o M_{eff}$ **[T]**	1.814 ±0.002		
$\gamma_{\|\|}$**[GHz**T^{-1}**]**	28.5 ±0.4	$\gamma_{\perp}$**[GHz**T^{-1}**]**	29.9±0.1
$\mu_o H'_{ex}$ **[mT]**	232 ± 3	A^* $[pJ\,m^{-1}]$	22.0±0.3
$\mu_o H'_S$ **[T]**	0.2±0.1	K_s^* $[mJ\,m^{-2}]$	8± 3

Table 1: CoFeB: Magnetic parameters (* Estimation)

The value for $\mu_o M_{eff}$ is in agreement with the values found in a thickness dependence study where uniaxial anisotropy is also considered, while it is known that the saturation magnetization for CoFeB is around $\mu_o M_s$= 1.7 T [8]. Comparing these two values, the uniaxial bulk anisotropy could be estimated to be around 114 mT. Now, since it is found that $M_s < M_{eff}$, therefore $K_1 < 0$ which implies that the hard axis is the perpendicular to the film. The fact that the effective magnetization is larger than the saturation magnetization implies that the real values for A and K_s must be smaller than the obtained ones. The same mentioned study provides reference values for K_s between 1.03-1.8 $mJ\,m^{-2}$ **[8].**

5.2 Permalloy 40 nm

A $Ni_{80}Fe_{20}$ (Py) 40 nm thickness, 2mm×2.2mm surface area sample was characterized prior to a bilayer system consisting of YIG(80)/Py(40). The sample was grown by magnetron sputtering on an unknown substrate, it was provided by Philipp Pirro (University of Kaiserslautern, Germany). Measurements on the sample were conducted in order to obtain a reference for a better understanding of the behavior of the bilayer that is presented later.

5.2.1 Spectra

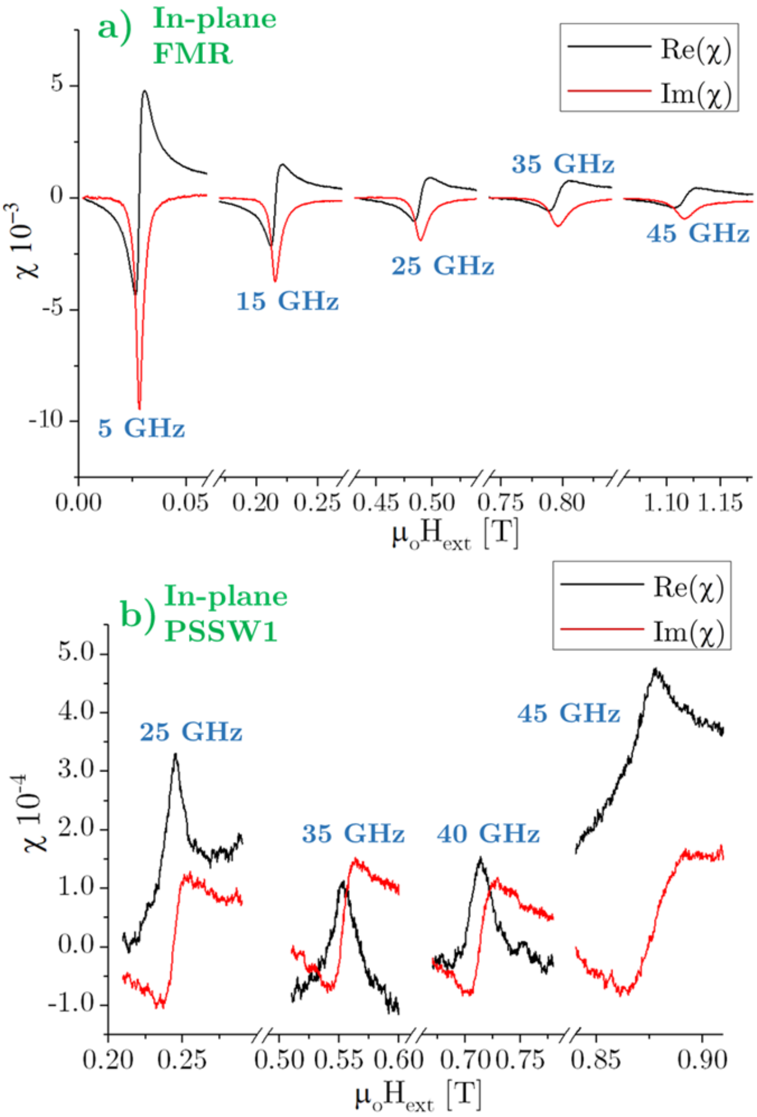

Figure 17: Py: Resonance profiles for different frequencies in the in-plane configuration: a) FMR mode, b) PSSW1 mode

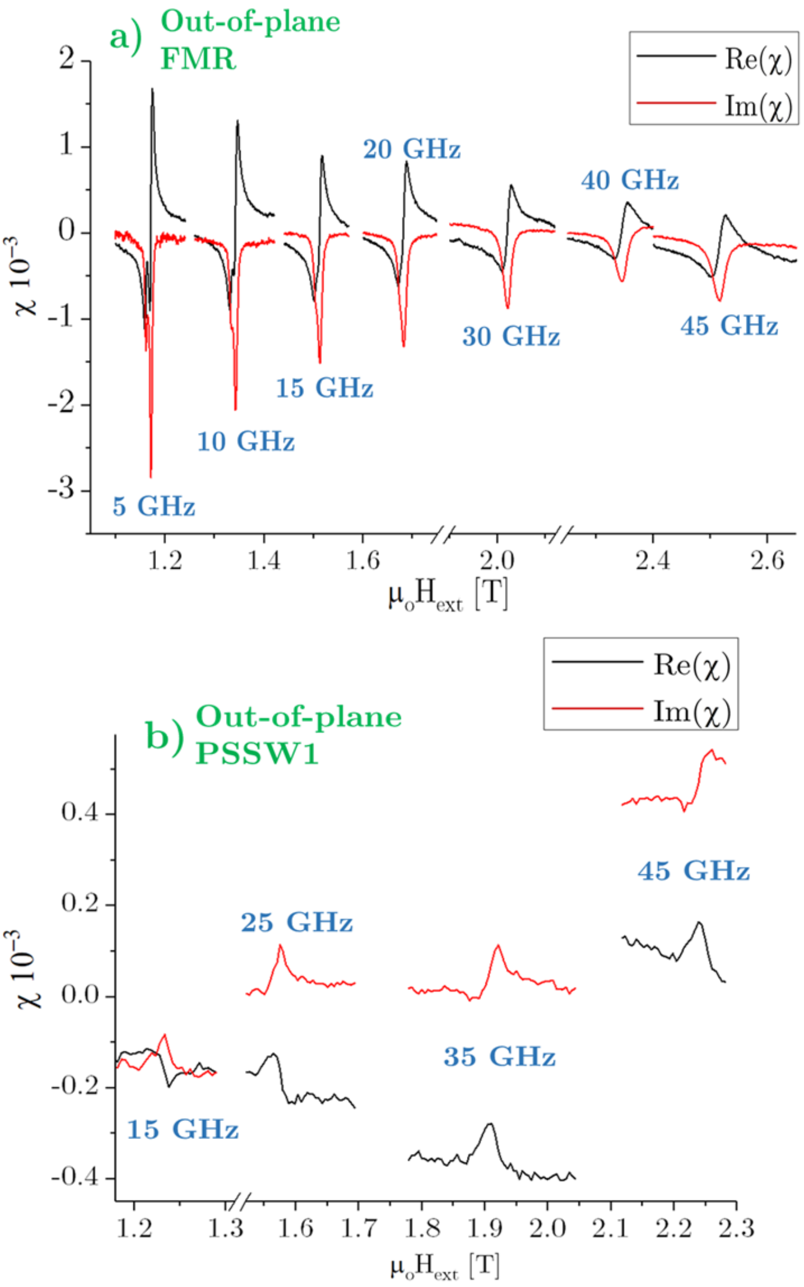

Figure 18: Py: Resonance profiles for different frequencies in the out-of-plane configuration: a) FMR mode, b) PSSW1 mode

From Figure 17 a) it is clear that the in-plane FMR mode presents a normal resonance spectra, and this happens for all the frequency range. Again, a widening of the peaks with field and a reduction of amplitude with frequency is visible. The PSSW1 mode presents some important noise, but the resonance peaks are well defined and their widths do not change much. Some frequencies (e.g. 25 Ghz) present non-symmetrical PSSW1 peaks which is the influence of the FMR mode signal. Once again there is a phase shift for the PSSW1 mode (see discussion for CoFeB).

From the out-of-plane resonance profile of Figure 18, it is clear that the FMR mode presents a peculiarity at low frequencies. For 5 and 10 GHz there are two clear peaks that appear to merge at 15 GHz and become one at 20 GHz. This extra peaks do not belong to PSSW1 modes, since those are higher in frequency (not visible until 15 GHz, see Figure 18 a)). The fact that H_{ext} is larger than M_s ensures that the film's magnetization is saturated. Therefore the extra peaks cannot be a result of a not fully saturated state. These peaks must be created by grains where M_s have a different value than the rest of the material. In the spectra analysis, the higher field is considered as the resonance field, since it appears to be the predominant FMR response (see Figure 18). Higher frequencies follows usual FMR behavior where there is a single peak. The PSSW1 modes present similar profiles to the ones shown for in-plane configuration except that the baseline of the signal is variable. The reason for this varying baseline is unknown, but the resonance conditions can still be obtained.

5.2.2 Dispersion relations and magnetic parameters

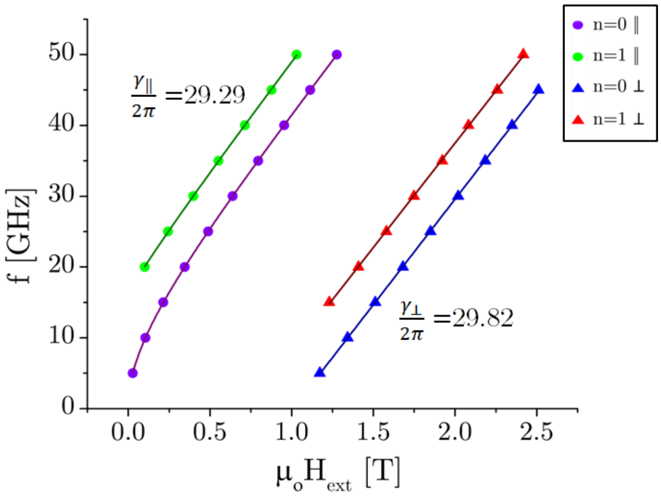

Figure 19: Py: Fitted dispersion relations for FMR and PSSW1 modes in in and out-of-plane configurations

In the case of Py the ratio between the the in and out-of-plane γ's is $\frac{\gamma_{||}}{\gamma_{\perp}} = 0.98$. This ratio is larger than the case of the CoFeB film.

$\mu_o M_{eff}$ **[T]**	1.03 ±0.01		
$\gamma_{\|\|}$**[GHzT^{-1}]**	29.29 ±0.02	$\gamma_{\perp}$**[GHzT^{-1}]**	29.82±0.09
$\mu_o H'_{ex}$ **[mT]**	250 ± 7	A^* [$pJ\,m^{-1}$]	16.5±0.3
$\mu_o H'_S$ **[mT]**	21±0.02	K_s^* [$mJ\,m^{-2}$]	0± 20

Table 2: Py: Magnetic parameters (* Estimation)

The calculated value for M_{eff} is around the expected value for M_s in Permalloy (typically 1 T depending on the composition) [6]. This implies that the uniaxial bulk anisotropy is very small if not negligible. Something similar happens for the surface anisotropy, where the estimated constant should be between $\pm 20\ mJ\,m^{-2}$. Then there is not important anisotropy in this particular Py film as usual for this material. The estimated exchange constant is appreciably larger than values found in the literature for Py (typically 10.5 $\pm 10\%\ pJ\,m^{-1}$) [24]. Since M_{eff} is not too different in comparison with the expected saturation magnetization, the estimation of A should be close to the actual value for the film which, as was already mentioned, is uncommon for Permalloy.

5.3 YIG 29nm

A 3×3 mm $Y_3Fe_5O_{12}$ sample with a thickness of 29 nm is measured in order to obtain its magnetic parameters with special interest in a estimation of M_s. The sample was used as a propagating medium for spin wave beam measurements. This estimation of the saturation magnetization is to be compared with a value obtained by spin wave spectroscopy. The sample was grown by magnetron sputtering on a $Gd_3Ga_5O_{12}$ Gadolinium Gallium garnet (GGG). It was provided by Benjamin Jungfleisch (Argonne Laboratory, USA). In this case the sample could not be cut to fit the podium so it was fastened to the board as can be seen in Figure 10.

5.3.1 Spectra

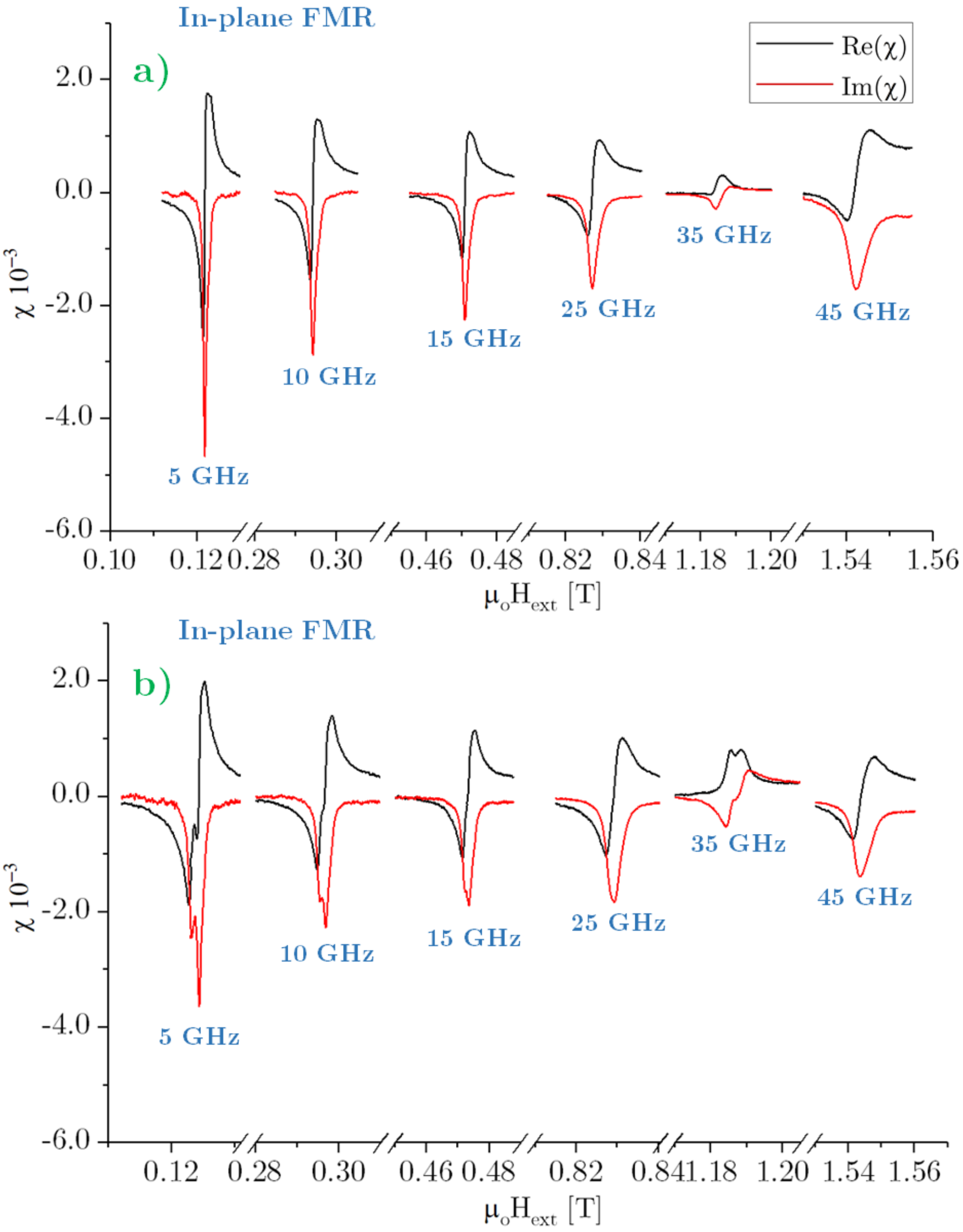

Figure 20: YIG 29 nm: Resonance profiles for different frequencies in the in-plane configuration: a) FMR mode with sample oriented in a arbitrary direction (Orientation 1), b) FMR mode with sample rotated by 90^o in the plane (Orientation 2).

The the most important feature for the 29 nm YIG is that it does not present a PSSW1 mode. From in and out-of-plane measurements just the uniform mode can be identified. Recalling section 4.3.5, this is expected since YIG is not a conductor, then the shielding effect does not take place. There are not eddy currents in the film which could excite the non-uniform mode.

The sample was measured, as was done for the all other samples, first in a arbitrary orientation and later rotating it by 90° in the plane. Only this sample presents important differences in the FMR spectra between the two orientations. Figures 20 a) and 21 a) presents the spectra for orientation 1 in and out-of-plane respectively, while Figures 20 b) and 21 b) present the spectra for orientation 2. From comparing the two orientations, it is obvious the sample present some inhomogeneity. This imply there are macroscopic grains of material for which the magnetic response change appreciably by modifying the position of the CPW with respect to the sample. Since the change is sensitive to a 90° rotation of the complete sample, this grains should not be uniformly distributed in the material.

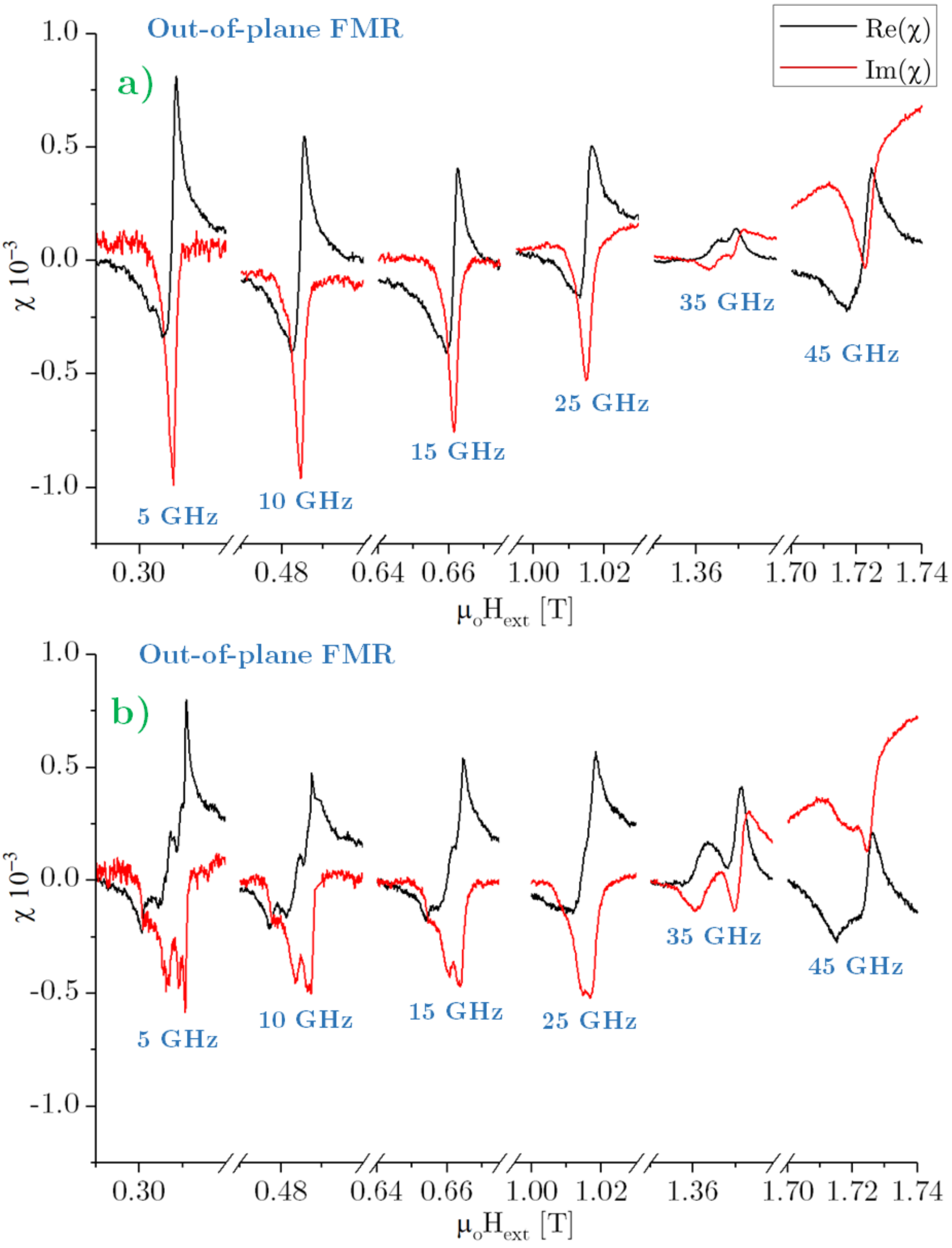

Figure 21: YIG 29 nm: Resonance profiles for different frequencies in the out-of-plane configuration: a) FMR mode with sample oriented in a arbitrary direction, b) FMR mode with sample rotated by 90^o in the plane.

The sample present other magnetic response which appears to be given by the substrate. As can be seen in Figure 22, there is a very wide resonance profile along most of the field range. It starts to be visible at 15 GHz, where the YIG thin peak is clearly identifiable. This wide resonance is magnetic, since it evolves with field and frequency. It does not affect importantly the YIG resonance, then it can be characterized independently as presented before. This resonance can be seen for the in- and out-of-plane configurations with similar profiles. It appears to follows YIG resonance just with a field shift, and if fitted with a linear model it presents basically the same $\gamma's$ that YIG. Measurements were performed with the YIG side of the sample on top and the substrate on the board. This provides the same profiles that can be seen in Figure 22 without YIG's excitation. This allows to attribute this resonance to the substrate alone, although its nature is not understood. Since GGG has not been reported to be magnetic or to have this type of response, a possible explanation is that it can be contaminated with magnetic particles that create a very inhomogeneous media which can be exited in a very large range of field.

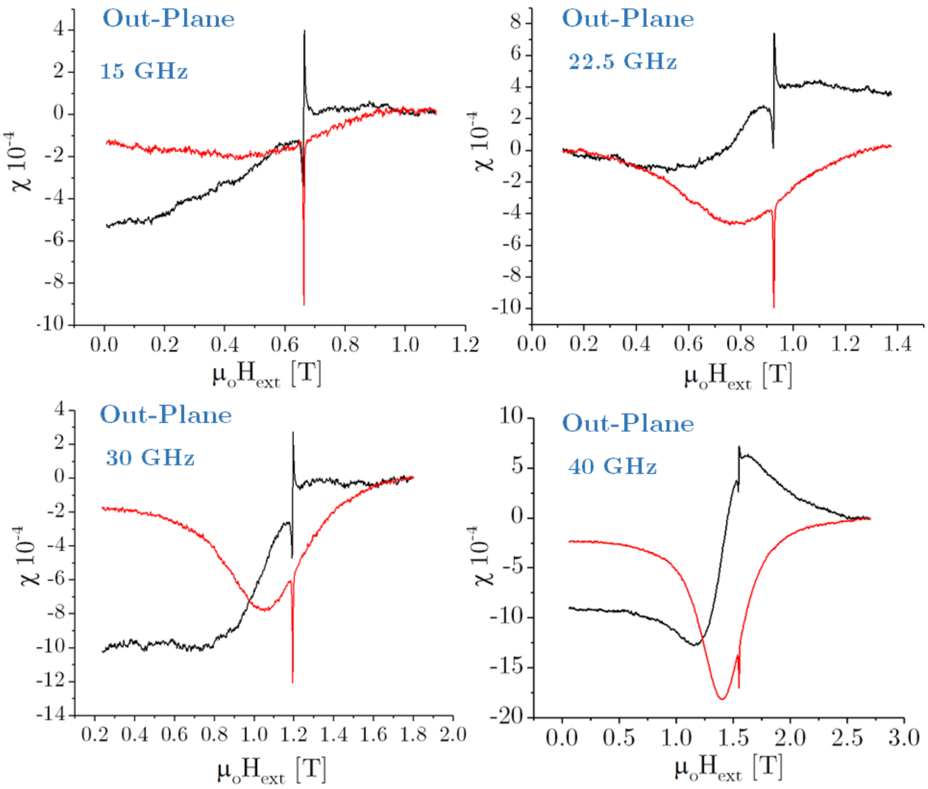

Figure 22: YIG 29 nm: Progression of additional wide resonance attributed to GGG.

5.3.2 Dispersion relations and magnetic parameters

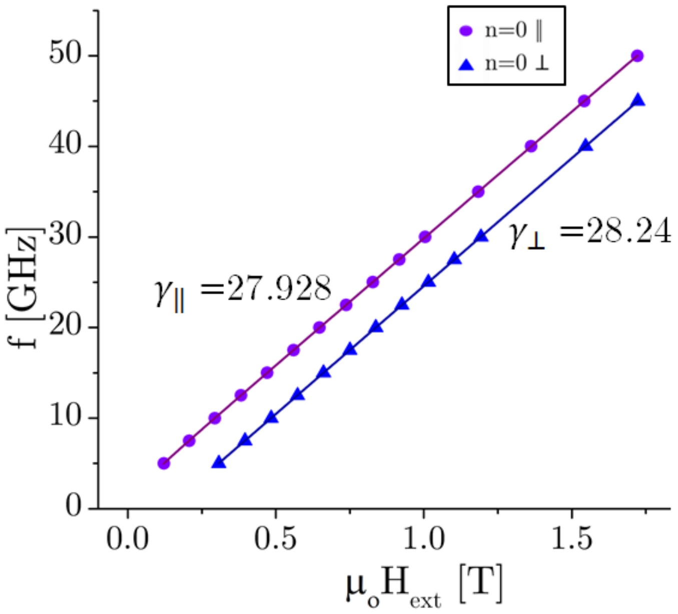

Figure 23: YIG 29 nm: Fitted dispersion relations for FMR mode in in and out-of-plane configurations

Since there is no measurable PSSW1 mode. In this case, the value of the effective magnetization does include the bulk and surface anisotropy.

$\mu_o M_{eff}$ **[mT]**	141.5 ±0.7		
$\gamma_{||}$**[GHz**T^{-1}**]**	27.928 ±0.009	$\gamma_\perp$**[GHz**T^{-1}**]**	28.24±0.01

Table 3: YIG 29 nm: Magnetic parameters

The ratio between the γ's is $\frac{\gamma_{||}}{\gamma_\perp} = 0.99$ which shows not important difference between the in- and out-of-plane configurations.The estimated value for the effective magnetization is lower than the tabulated value of $\mu_o M_s$=176.0 mT [4]. Larger values have been reported for M_{eff} due to strong uniaxial anisotropy, with hard axis out-of-plane [4]. The lower value could be explained by weak uniaxial bulk and surface anisotropies summing up to a approximate value of 34 mT.

5.4 YIG AL5007

A 2×2 mm $Y_3Fe_5O_{12}$ sample with 18.2 nm thickness is measured in order to compare its magnetic properties with the previously presented 29 nm YIG sample. In this case, the YIG was grown by pulsed laser deposition on a GGG substrate and was provided by Abdelmadjid Anane (UMPhys CNRS-Thales, Palaiseau, France). There is special interest in comparing Gilbert's damping parameters between this sample and the 29 nm one which can allow to compare the effectiveness of the two growth techniques in lowering α.

5.4.1 Spectra

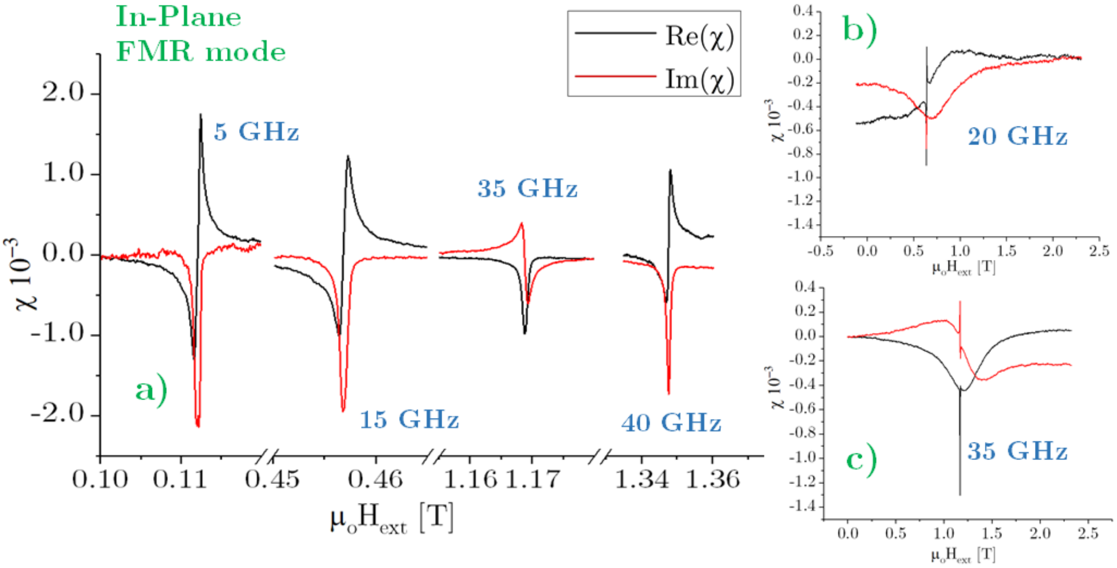

Figure 24: YIG AL5007: Progression of additional wide resonance attributed to GGG.

Again the PSSW1 mode could not be measured since it is not really exited due to the lack of eddy currents. Just the FMR mode is observed and present similar resonance fields to the 29 nm YIG. This YIG sample did not present differences in its spectra by rotating it in the plane. The resonance peaks are clearly defined for all the frequencies and do not show inhomogeneities. The wide resonance, attributed to the GGG substrate, is also present with a very similar behavior to the 29 nm YIG. Also the phase change of approximately 90° happens consistently at 35 GHz for both in- and out-of-plane with a reduction in the amplitude. The fact that two samples with very different fabrication processes present so similar behavior indicates that these are characteristic fro the combination of GGG/YIG. An influence in the FMR response given by the GGG substrate has been observed just for low temperatures (T<10 K) [25]. This therefore indicates that the common process of fabrication of the presented samples introduces some magnetic impurities in the material which affects drastically the magnetic response. The only clear difference between the two YIG samples is the lack of inhomogeneities in the YIG AL5007, which appear to be corrected by the pulsed laser deposition technique. This would imply that the sputtering deposition process facilitates the creation of large grains of material with different magnetic properties. The Permalloy sample, which was grown by magnetron sputtering too, confirms this supposition.

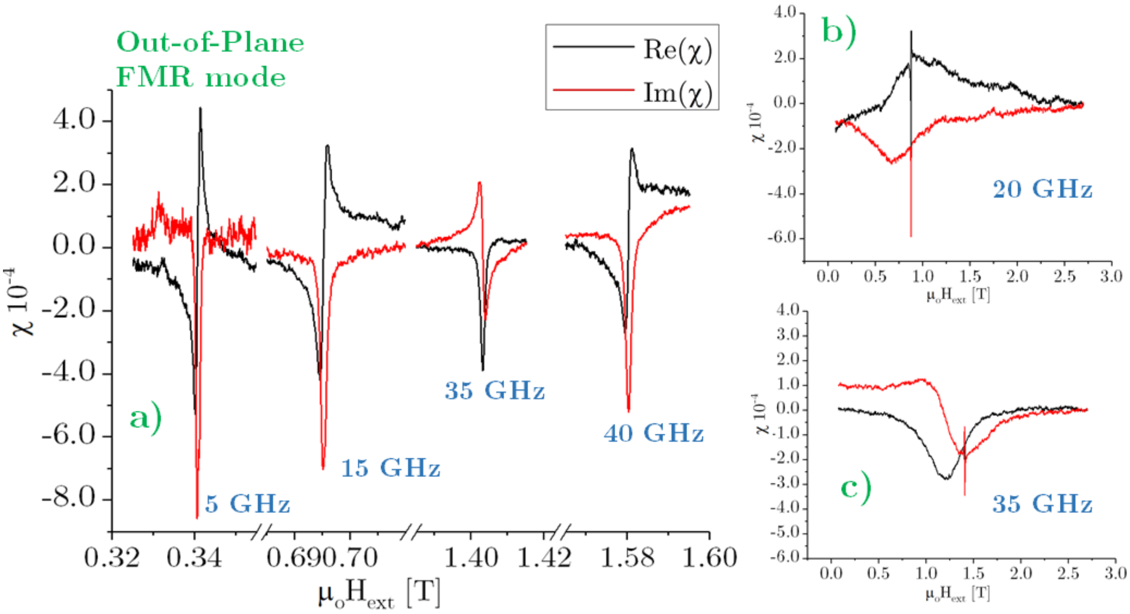

Figure 25: YIG AL5007: Progression of additional wide resonance attributed to GGG.

5.4.2 Dispersion relations and magnetic parameters

As in the case of the 29 nm YIG, the lack of the PSSW1 mode, just estimations can be calculated for the magnetic properties that are presented in Table **??**.

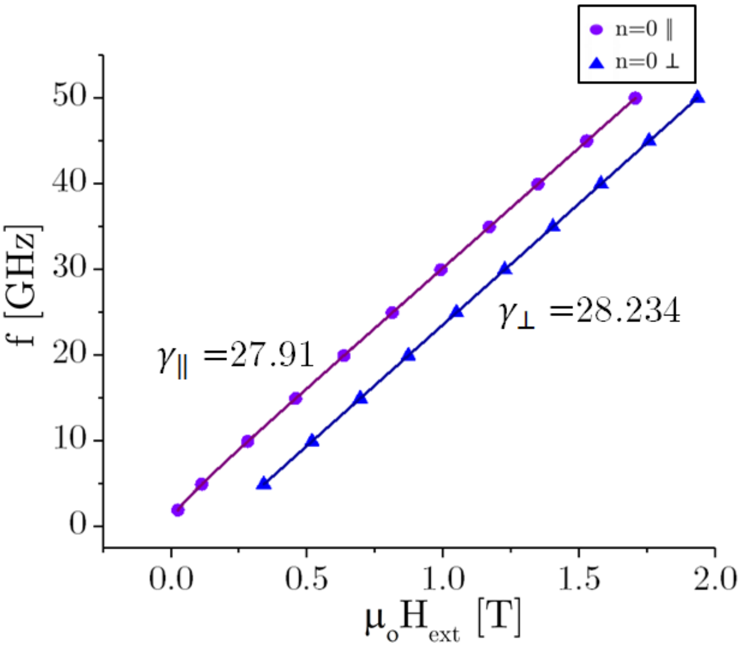

Figure 26: YIG AL5007: Fitted dispersion relations for FMR mode in in- and out-of-plane configurations

In this case the ratio between the γ's is $\frac{\gamma_{||}}{\gamma_{\perp}} = 0.99$, which again shows almost no difference between the two configurations. In this case $\mu_o M_{eff}$ has been found to be larger than the tabulated value for M_s. This imply that there are negligible surface or bulk anisotropies in the sample and that the found estimation is very close to the saturation magnetization.

$\mu_o M_{eff}$ **[mT]**	176.1 ±0.9		
$\gamma_{||}$**[GHzT^{-1}]**	27.91 ±0.01	$\gamma_{\perp}$**[GHzT^{-1}]**	28.234±0.004

Table 4: YIG AL5007: Magnetic parameters

5.5 YIG/Py

The sample consist of a YIG 80nm/Py 40nm bilayer. The YIG was grown by liquid phase epitaxy on a GGG substrate, and the Py was grown by magnetron sputtering on the YIG. The was no special treatment between the two layers. The sample was provided by Philipp Pirro (University of Kaiserslautern, Germany). This sample is studied as a possible candidate for bilayer systems where non-reciprocity effects are exploited. The magnetic response is to be studied in order to be able to understand how the dynamics of each of the components is affected by the presence of the other. A estimation on the magnetic properties is also performed.

5.5.1 Spectra

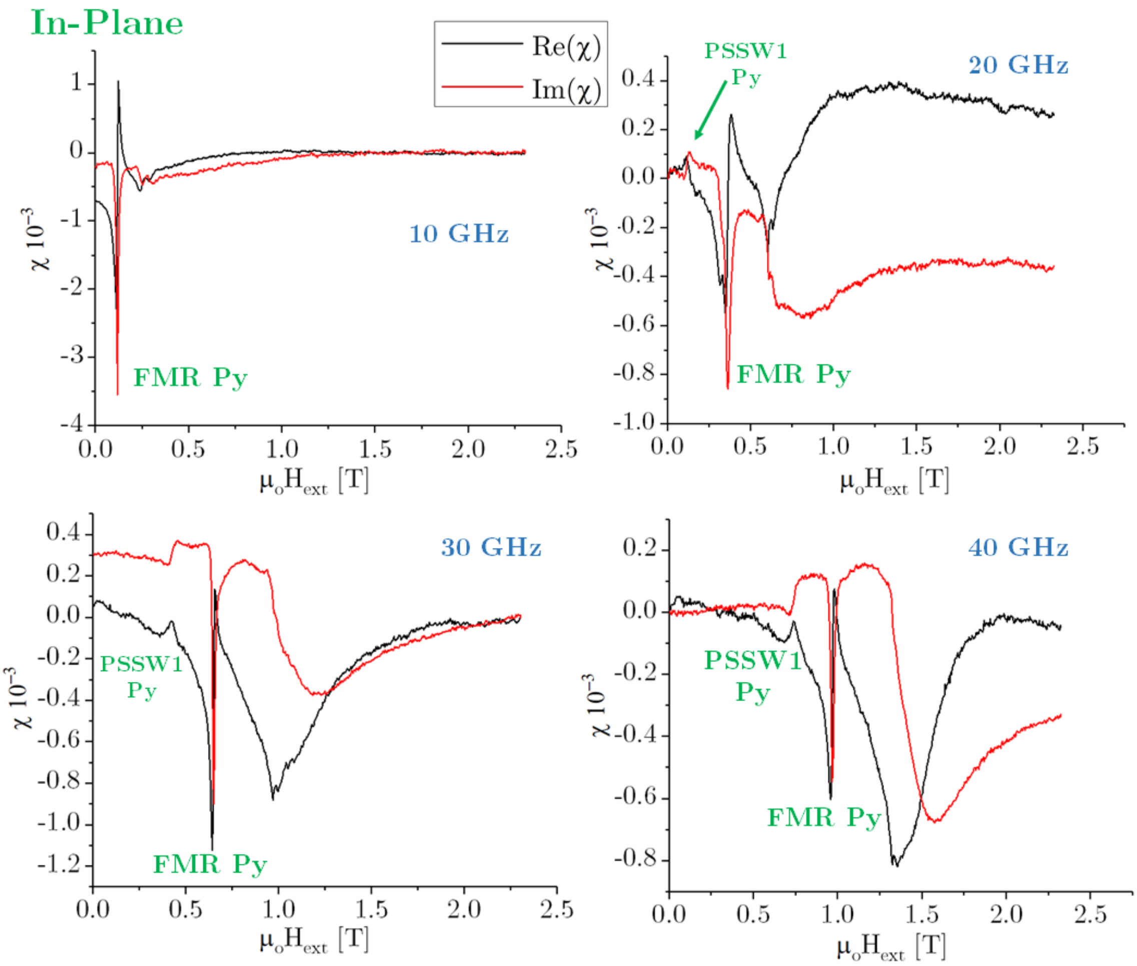

Figure 27: YIG/Py: Resonance profiles for the bilayer in the in-plane configuration.

In Figure 27 three main resonances can be identified: the Py's fundamental mode, Py's PSSW1 (not visible yet at 10 GHz) and another very wide and large amplitude resonance. The resonance peaks for Permalloy are relatively well defined which allows to track their resonance up to high frequencies. The PSSW1 mode starts to be measurable around 15 GHz similarly to the Py single layer. The third resonance profile, which is always at higher field than Py's FMR mode, appears to show an important phase change. This would suggest it is given by eddy currents created at Py, but such behavior was not observed for the single layer. It could be a result of Py response to the magnetic interaction with YIG, more specifically eddy currents created by the magnetic flux that the YIG layer induce in Py. This could give some explanation on the fact that YIG's FMR is not visible. Possibly, YIG's resonace is canceled by Permalloy in order to create an opposite flux which could explain the phase shift of the third resonance. This still would not be able to explain why this resonance peak is so wide and occurs at larger fields than Py. YIG's resonance should be lower in field (see Figure 24). Note all the peaks are affected by the resonance from the substrate, which is very wide. This could change slightly the resonance profiles, but cannot explain the width of the third resonance (see Figure 22).

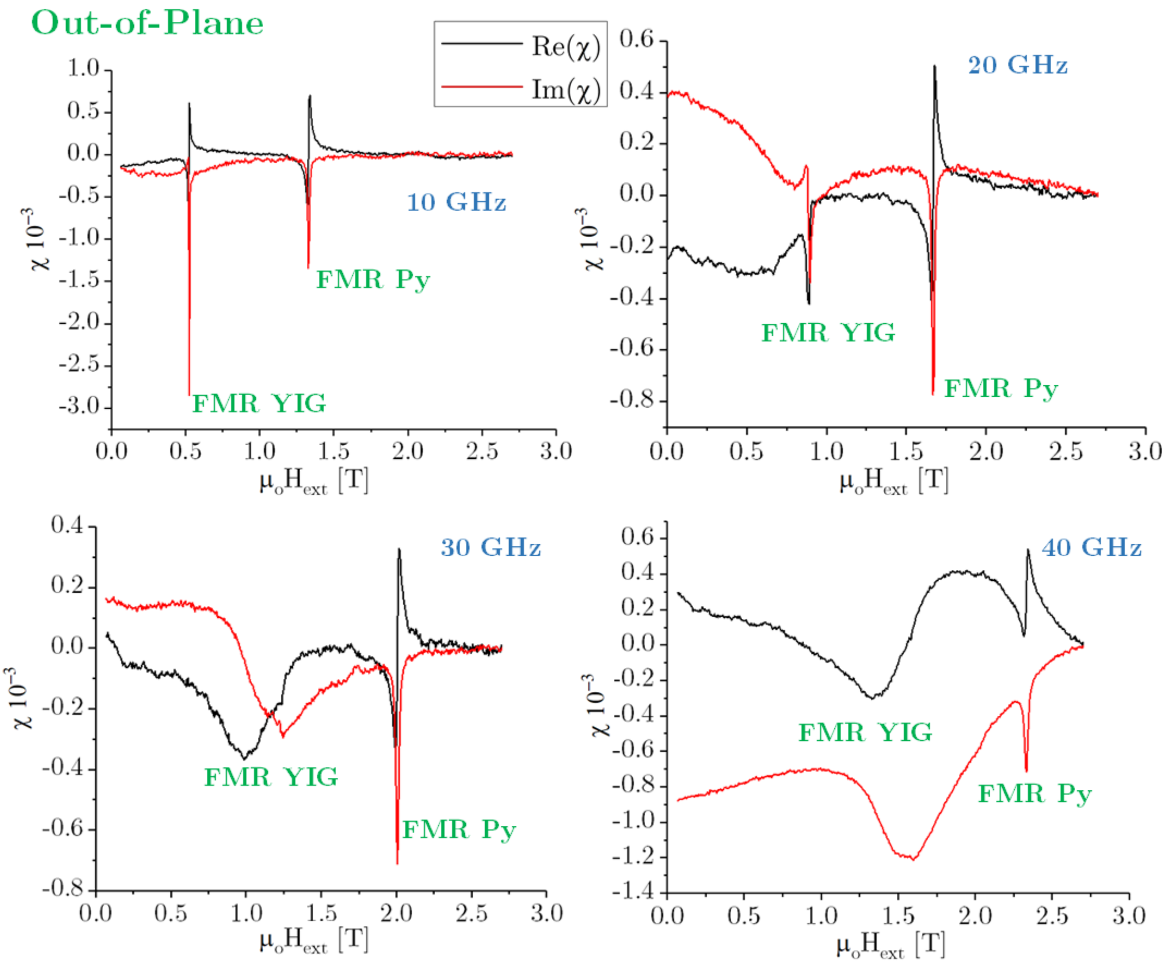

Figure 28: YIG/Py: Resonance profiles for the bilayer in the out-of-plane configuration.

In the case of the out-of-plane configuration there are other peculiarities. YIG's resonance is clearly visible at least in lower frequencies. Two main peaks can be observed in Figure 28, which correspond to Py and YIG respectively. As was expected, YIG's resonance is lower in field than Permalloy's. No PSSW1 mode for Py is measurable, which could be attributed to superposition with YIG's larger resonance profile (PSSW1 has a very small amplitude, see Figure 18). YIG's peak is easily identifiable in the lower resonance spectra, but becomes distorted at higher frequencies where the GGG resonance becomes important. It is unexpected for YIG peak to change so drastically since as was observed for the single layers, GGG's resonance does no affect the profiles of YIG (see Figures 22, 24 and 25). This interaction between the two resonances could explain the lack of YIG FMR mode in-plane and the shape of the wide resonance measured. The in-plane and out-of-plane wide resonances show similar profiles.

A possible coupling between the modes of the two layers is suspected. In the case of the in-plane magnetization the Permalloy's, peaks seem to be slightly modified in comparison to the single layer, and YIG resonance is not identifiable. In the case of out-of-plane magnetization the resonance peaks of Py and YIG seems to be more independent. The fact that there are different pinning conditions for the in-plane and out-of-plane configurations could explain the difference between the two spectra. From equation (84), in the in-plane configuration, the out-of-plane dynamic component of $\vec{M}$ could be pinned , while the in-plane component is free. For the out-of-plane configuration both components are pinned. This would allow different interaction between the layers in the two configurations. The material conditions at the interface could also modify the resonance profiles. Since there is no special treatment between the two layers, some oxidation at the interface could be affecting the measurements.

5.5.2 Dispersion relations and magnetic parameters

In the case of the bilayer, although there exists a lack of peaks, the estimation of the magnetic parameters can still be done.

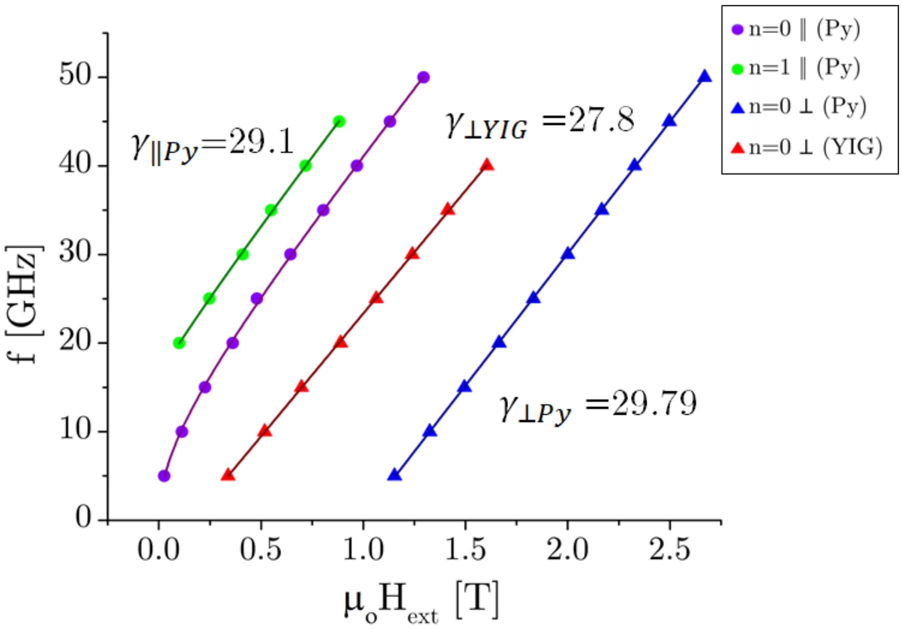

Figure 29: YIG/Py: Fitted dispersion relations for FMR mode in in- and out-of-plane configurations

In this case the Permalloy layer presents a ratio of $\frac{\gamma_{||}}{\gamma_{\perp}} = 0.97$. Once again, no mayor evidence of anisotropy exist in Py; the effective magnetization is very close to the saturation value. A possibly lower surface anisotropy could be present at the top layer of Py. Although, from the estimation, it is not possible to be sure of such reduction.

$\mu_o M_{eff}$ **[mT]**	989 ±3		
$\gamma_{\|\|}$**[GHz**T^{-1}**]**	29.1 ±0.4	$\gamma_{\perp}$**[GHz**T^{-1}**]**	29.79±0.07
$\mu_o H'_{ex}$ **[mT]**	230 ± 10	A^* [$pJ\,m^{-1}$]	15±0.6
$\mu_o H'_S$ **[mT]**	0±50	K_s^* [$mJ\,m^{-2}$]	0.0± 0.8

Table 5: Py layer in YIG/PY: Magnetic parameters (* Estimation)

In the case of the YIG layer the effective magnetization is slightly lower than the saturation magnetization ($\mu_o M_s$=176.0 mT [4]), which would suggest negligible anisotropy. The value found for $\gamma_{\perp}$ is lower than the values obtained for the single layers. This could be caused by the presence of Py at the bottom surface.

$\mu_o M_{eff}$ **[mT]**	161 ±5
$\gamma_{\perp}$**[GHz**T^{-1}**]**	27.8 ±0.1

Table 6: YIG layer in YIG/Py: Magnetic parameters

5.6 Linewidths

The linewidths (see equation (56)) for in- and out-of-plane configurations are presented in Figures 30 and 31 respectively.

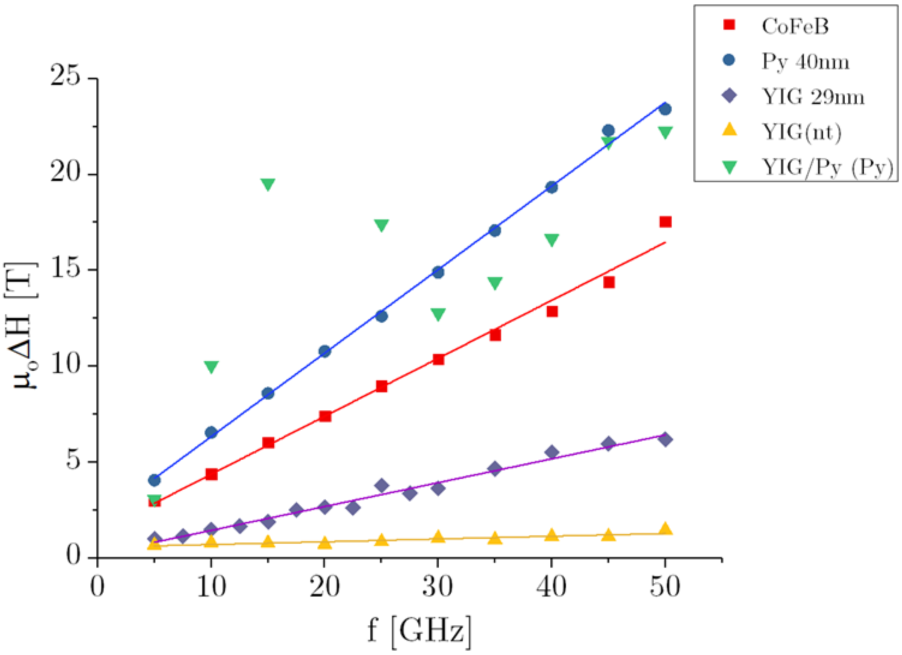

Figure 30: Linewidths for in-plane configuration

No linear fit could be performed for the YIG/Py sample in the in-plane configuration due to a important increase of the linewidth around 15 GHz.

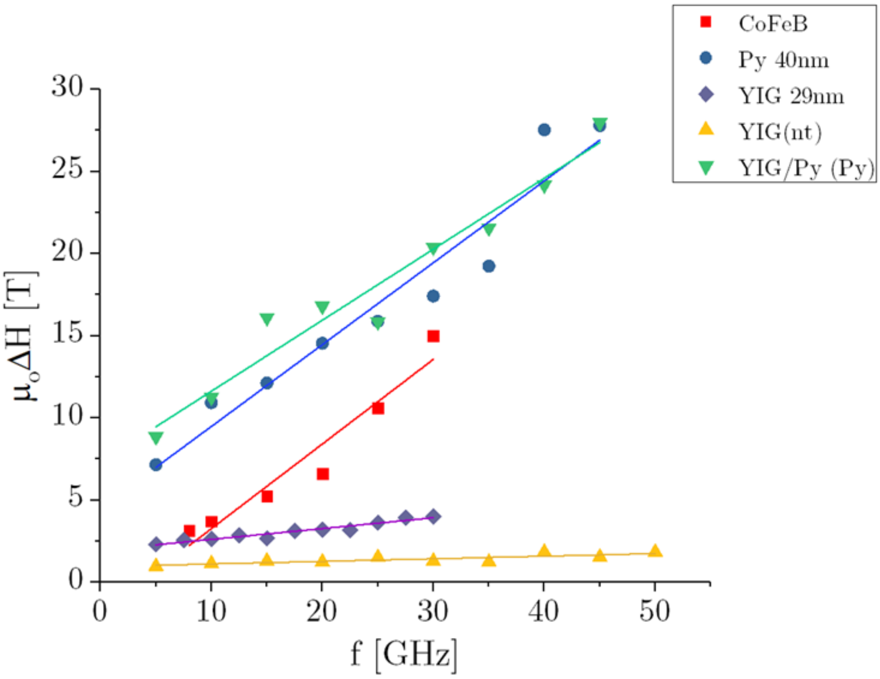

Figure 31: Linewidths for out-of-plane configuration

The obtained damping parameters for in- and out-of-plane are presented in Table **??**.

	CoFeB	**Py 40nm**	**YIG 29nm**	**YIG 18.2nm**	**Py (YIG/Py)**
$\alpha_{\|\|} \cdot 10^{-4}$	43.1±0.3	63±1	17.4±0.7	2.0± 0.3	-
$\mu_o H_{o\|\|}$**[mT]**	1.4±0.3	1.9±0.2	0.2±0.1	0.57 ±0.07	-
$\alpha_{\perp} \cdot 10^{-4}$	77±6	74±7	9.3±0.3	2.2±0.2	59±6
$\mu_o H_{o\perp}$**[mT]**	-2±1	5±1	1.9±0.1	0.9±0.1	8±1

Table 7: Damping parameters and for in- and out-of-plane measurements

From the calculations, there is an increase in α for most of the samples, except for the YIG 29 nm. Comparing the two YIGs, it is clear that YIG AL5007 has a lower damping factor. This can be related to the fact that the second is fabricated by pulsed laser deposition which seems to create a sample with less damping than the magnetron sputtering technique. The increase in α could be directly related to the grain formation in the sputtered sample. The Py in the bilayer has a smaller damping factor than the single layer (Py 40nm), although a comparison between these two should be done carefully due to the large uncertainty. No damping factor for the YIG layer is given since there is not enough well defined peaks to have an accurate estimation.

6 Conclusions

It has been shown that in the case of a simplified study of the uniform dynamics of the magnetization (fundamental mode) a single straightforward theory can be developed to obtain good estimation of both the effective magnetization and eventually anisotropy in the ferromagnetic films. This is enough in many FMR studies where there are limitations in frequency and field range as well as in the detection of the magnetic response.

A more detailed description of the dynamics is necessary given by the spin wave modes theory, which gives an exact dispersion relation for the fundamental as wells as for the non-uniform modes. This, both in the case of non-propagating waves (perpendicular standing spinwaves), and for propagating waves in thin films. Although the theory and derivation of these dispersion relations is tedious, a complete demonstration of the calculation in the most general conditions has been presented in this manuscript which can help the reader to access Kalinikos and Slavin seminal work. The justification of this explicit derivation lies in the fact that each step provides an important insight of the nature of spinwaves in thin films. Something to point out from this derivation is the fact that the internal static field action is not independent of the mode of oscillation of the magnetization. Non-uniform modes have a different effect of the internal field, something that is not consider in the static field approximation for the fundamental mode. The potential of this theory encourage its further development to probe additional features, as it was done here by including an uniaxial surface anisotropy term to the original analysis of Kalinikos and Salvin. This also inspires development of microwave technology to expand the frequency range to probe higher order modes.

The importance of microwave correction analysis has been explained in VNA-FMR technique. This, since the network used for the transmission of the microwave can introduce many alterations to the signal measured by a VNA due to impedance mismatch at different parts of the line. The calibration of the device is not enough to take all of this factors into account. Therefore a series of corrections need to be performed in order to isolate the magnetic response of the material under study which allows a more accurate estimation of the absorbed power by the magnetic resonance.

The results provide precise estimations of the magnetic properties of interest for each studied sample. In the case of CoFeB, the exchange constant was estimated, a uniaxial anisotropy was found to have a contribution to the effective magnetization whit a hard axis perpendicular to the plane. An important difference was found between the damping factors in- and out-of-plane.

The single layer Permalloy was found to have a usual behavior with probable grains in the composition with different properties just visible in the out-of-plane configuration. A good estimation of the saturation magnetization was found together with negligible anisotropy as is common for Py. The difference between the damping factors is small and both values are in agreement with literature.

In the case of the two YIG samples very similar properties were found despite their different fabrication process. As was expected from the lack of shielding due to the insulating nature of YIG, no PSSW1 mode could be measured. This did not allow to estimate the surface anisotropy which is included on the effective magnetization. From this estimation, the 29 nm YIG appears to have a total anisotropy around the value of 34 mT. This film also present measurable inhomogeneities in its structure which suggests some grains of different properties which appear to be non-uniformly distributed. On the other hand, the 18.2 nm thickness YIG does not present important anisotropy since its effective magnetization is in agreement with the tabulated value for M_s. Also, the obtained spectra do not present any visible inhomogeneity which allows to confirm the tendency of grain formation in the magnetron sputtering technique. This grains could be the responsible for larger damping factor in the case of the 29 nm YIG (α=0.0017) in comparison with the 18.2 nm thickness YIG (α=2$\times$10^{-4}). For these two samples a very wide and large amplitude resonance was measured in addition to the YIG peaks, it was attributed to magnetic impurities in the GGG substrate.

In the case of the bilayer, similar results are found between the Py layer and the 40 nm Py reference, although the PSSW1 mode was not observed in the out-of-plane configuration in YIG/Py. This is attributed to a superposition of signals between Py's PSSW1 and YIG's FMR modes (in out-of-plane configuration), since the second has a much higher amplitude. Other surprising feature is the lack of YIG's FMR mode in the in-plane configuration. A complete shielding of the microwave signals is discarded because of the out-of-plane excitation of YIG and the visible wide resonance attributed to the GGG substrate. A possible coupling between the layers could explain the unusual behavior observed in-plane. This is contrasted with the out-of-plane measurements where the peaks of each layer appear well defined. It could be related to the pinning condition on the interface which in the case of in-plane magnetization leads to an elliptical oscillation of the dynamical components of $\vec{M}$, because the in-plane component is free to oscillate, whereas the out-of-plane magnetization have the two dynamical components pined. A estimation of the damping factor for the Py layer could not be obtained because of a unusual broadening of the signal around 15 GHz. The out-of-plane damping factor is reduced in comparison with the Py 40nm. There was not enough data to estimate the damping factor for the YIG layer.

To obtain more confident conclusions about the bilayer system a more detailed study is needed. To have a better understanding of the conditions at the interface, other samples could be prepared by treating the layers in order to reduce any possible oxidation. Also different samples, with varying thickness of the two layers, could be measured in order to probe a possible FMR YIG mode for in-plane magnetization. Since obtaining the pining conditions at the interface is very complicated, a varying angle study (angle between the normal to the film and the magnetization) could shed some light on the effective pining. The spectra is expected to follow some kind of transition between the possibly coupled layers (measured in the in-plane) and the independent resonances (measured out-of-plane). The development of a theory which tackles the surface anisotropy conditions at the interface could be an important addition to Kalinikos and Slavin theory together with a second order treatment where interaction between modes is considered. Since GGG response appears to be a constant, some way of shielding this resonance should be investigated to have better results in CPW-FMR specially in bilayers where its influence becomes more important. More experimental data, in different thickness samples, should be obtained to better understand the difference in γ for in- and out-of-plane measurements.

Appendices

Appendix A: Application of boundary conditions on SWM

Applying boundary conditions on the top surface:

$$\frac{\partial \varPhi_n^p(\xi)}{\partial \xi}|_{\xi=l/2} + d_1^p \varPhi_n^p(l/2) = 0 \tag{148}$$

$$-\kappa_n^p Sin(\kappa_n^p \frac{l}{2}) + d_1^x Cos(\kappa_n^p \frac{l}{2}) + B_n^p \left[\kappa_n^p Cos(\kappa_n^p \frac{l}{2}) + d_1^x Sin(\kappa_n^p \frac{l}{2}) \right] = 0 \tag{149}$$

And applying the condition for the lower surface (sings taken into account already):

$$\frac{\partial \varPhi_n^p(\xi)}{\partial \xi}|_{\xi=-l/2} + d_1^p \varPhi_n^p(-l/2) = 0 \tag{150}$$

$$-\kappa_n^p Sin(\kappa_n^p \frac{l}{2}) + d_2^x Cos(\kappa_n^p \frac{l}{2}) - B_n^p \left[\kappa_n^p Cos(\kappa_n^p \frac{l}{2}) + d_2^x Sin(\kappa_n^p \frac{l}{2}) \right] = 0 \tag{151}$$

Solving for B_n^p in both equations and equating the found expressions leads to:

$$B_n^p = \frac{\kappa_n^p Sin(\kappa_n^p \frac{l}{2}) - d_1^x Cos(\kappa_n^p \frac{l}{2})}{\kappa_n^p Cos(\kappa_n^p \frac{l}{2}) + d_1^x Sin(\kappa_n^p \frac{l}{2})} = \frac{-\kappa_n^p Sin(\kappa_n^p \frac{l}{2}) + d_2^x Cos(\kappa_n^p \frac{l}{2})}{\kappa_n^p Cos(\kappa_n^p \frac{l}{2}) + d_2^x Sin(\kappa_n^p \frac{l}{2})} \tag{152}$$

Multiplying the denominators on both sides

$$\begin{gathered}(\kappa_n^p)^2 Sin(\kappa_n^p \frac{l}{2}) Cos(\kappa_n^p \frac{l}{2}) - d_1^p \kappa_n^p Cos^2(\kappa_n^p \frac{l}{2}) + d_2^p \kappa_n^p Sin^2(\kappa_n^p \frac{l}{2}) - d_1^p d_2^p Sin(\kappa_n^p \frac{l}{2}) Cos(\kappa_n^p \frac{l}{2}) = \\ -(\kappa_n^p)^2 Sin(\kappa_n^p \frac{l}{2}) Cos(\kappa_n^p \frac{l}{2}) + d_2^p \kappa_n^p Cos^2(\kappa_n^p \frac{l}{2}) - d_1^p \kappa_n^p Sin^2(\kappa_n^p \frac{l}{2}) + d_1^p d_2^p Sin(\kappa_n^p \frac{l}{2}) Cos(\kappa_n^p \frac{l}{2})\end{gathered} \tag{153}$$

$$\left[(\kappa_n^p)^2 - d_1^p d_2^p \right] 2 Sin(\kappa_n^p \frac{l}{2}) Cos(\kappa_n^p \frac{l}{2}) = (d_1^p + d_2^p) \kappa_n^p \left[Cos^2(\kappa_n^p \frac{l}{2}) - Sin^2(\kappa_n^p \frac{l}{2}) \right] \tag{154}$$

$$(\kappa_n^p - d_1^p d_2^p) Tan(\kappa_n^p l) = \kappa_n^p (d_1^p + d_2^p) \tag{155}$$

Appendix B: Field equation projected in the SMW base

The coefficients for each operator, given by the projection, are now explicitly calculated. For simplicity $\vec{S}_{n'}(\xi) = \vec{S}^x_{n'}(\xi) + \vec{S}^y_{n'}(\xi)$.

1. $\hat{R}$

Applying the operator $\hat{R}$ (equation 76) to the sum of SWM

$$\sum_{n'=0}^{\infty} \hat{R}\vec{S}_{n'}(\xi) = \sum_{n'=0}^{\infty} \begin{bmatrix} \frac{\omega_H}{\omega_M} - \Lambda^2(\frac{\partial^2}{\partial \xi^2} - k_\zeta^2) & 0 \\ 0 & \frac{\omega_H}{\omega_M} - \Lambda^2(\frac{\partial^2}{\partial \xi^2} - k_\zeta^2) \end{bmatrix} \begin{pmatrix} \Phi^x_{n'}(\xi) \\ \Phi^y_{n'}(\xi) \end{pmatrix} \tag{156}$$

$$\sum_{n'=0}^{\infty} \hat{R}\vec{S}_{n'}(\xi) = \sum_{n'=0}^{\infty} \begin{pmatrix} \left[\frac{\omega_H}{\omega_M}\Phi^x_{n'}(\xi) - \Lambda^2\left(\frac{\partial^2 \Phi^x_{n'}(\xi)}{\partial \xi^2} - k_\zeta^2 \Phi^x_{n'}(\xi)\right)\right] \\ \left[\frac{\omega_H}{\omega_M}\Phi^y_{n'}(\xi) - \Lambda^2\left(\frac{\partial^2 \Phi^y_{n'}(\xi)}{\partial \xi^2} - k_\zeta^2 \Phi^y_{n'}(\xi)\right)\right] \end{pmatrix} \tag{157}$$

$$\sum_{n'=0}^{\infty} \hat{R}\vec{S}_{n'}(\xi) = \sum_{n'=0}^{\infty} \begin{pmatrix} \left[\frac{\omega_H}{\omega_M} + \Lambda^2\left(\left(\kappa^p_{n'}\right)^2 + k_\zeta^2\right)\right]\Phi^x_{n'}(\xi) \\ \left[\frac{\omega_H}{\omega_M} + \Lambda^2\left(\left(\kappa^p_{n'}\right)^2 + k_\zeta^2\right)\right]\Phi^y_{n'}(\xi) \end{pmatrix} \tag{158}$$

$$\sum_{n'=0}^{\infty} \hat{R}\vec{S}_{n'}(\xi) = \sum_{n'=0}^{\infty} R \begin{pmatrix} \Phi^x_{n'}(\xi) \\ \Phi^y_{n'}(\xi) \end{pmatrix} \tag{159}$$

It is important to point out here that the eigen values for the operator $\hat{R}$ are the values R given by:

$$R = \frac{\omega_H}{\omega_M} + \Lambda^2 \left(k^p_{n'}\right)^2 \tag{160}$$

$$\left(k^p_{n'}\right)^2 = \left(\kappa^p_{n'}\right)^2 + k_\zeta^2 \tag{161}$$

Where $\vec{k}^p_{n'}$ is defined as the total wave vector which have contributions of the standing wave vector $\vec{\kappa}^p_{n'}$ and the propagation wave vector $\vec{k}_\zeta$.

Projecting equation (159) on the SWM leads to:

- $\overline{R}^{xx}$

$$\overline{R}^{xx} = \frac{1}{l}\int_{-l/2}^{l/2} \sum_{n=0}^{\infty} \vec{S}^x_n(\xi) \cdot \left[\sum_{n'=0}^{\infty} R\Phi^x_{n'}(\xi)\right] d\xi =$$

$$= \sum_{n=0}^{\infty}\sum_{n'=0}^{\infty} \frac{1}{l}\int_{-l/2}^{l/2} R\Phi^x_n(\xi)\Phi^x_{n'}(\xi) d\xi \tag{162}$$

- $\overline{R}^{xy}$

$$\overline{R}^{xy}=\frac{1}{l}\int\limits_{-l/2}^{l/2}\sum_{n=0}^{\infty}\vec{S}_n^x(\xi)\cdot\left[\sum_{n'=0}^{\infty}R\Phi_{n'}^{y}(\xi)\hat{y}\right]d\xi=0 \tag{163}$$

- $\overline{R}^{yx}$

$$\overline{R}^{yx}=\frac{1}{l}\int\limits_{-l/2}^{l/2}\sum_{n=0}^{\infty}\vec{S}_n^y(\xi)\cdot\left[\sum_{n'=0}^{\infty}R\Phi_{n'}^{x}(\xi)\hat{x}\right]d\xi=0 \tag{164}$$

- $\overline{R}^{yy}$

$$\begin{aligned}\overline{R}^{yy}&=\frac{1}{l}\int\limits_{-l/2}^{l/2}\sum_{n=0}^{\infty}\vec{S}_n^y(\xi)\cdot\left[\sum_{n'=0}^{\infty}R\Phi_{n'}^{y}(\xi)\hat{y}\right]d\xi\\&=\sum_{n=0}^{\infty}\sum_{n'=0}^{\infty}\frac{1}{l}\int\limits_{-l/2}^{l/2}R\Phi_n^y(\xi)\Phi_{n'}^y(\xi)d\xi\end{aligned} \tag{165}$$

Then $\overline{\hat{R}}$ can be written as

$$\overline{\hat{R}}=\sum_{n=0}^{\infty}\sum_{n'=0}^{\infty}\begin{bmatrix}R_{nn'}^{xx} & 0\\ 0 & R_{nn'}^{yy}\end{bmatrix} \tag{166}$$

where the coefficients are given by:

$$R_{nn'}^{pp}=\frac{1}{l}\int\limits_{-l/2}^{l/2}R\Phi_n^p(\xi)\Phi_{n'}^p(\xi)d\xi \tag{167}$$

2. $\hat{T}$

Applying the operator $\hat{T}$ (equation (77)) to the SWM

$$\sum_{n'=0}^{\infty}\hat{T}\vec{S}_{n'}^x(\xi)=\sum_{n'=0}^{\infty}\begin{pmatrix}N^{xx}\Phi_{n'}^x(\xi)\\ \left\{i\frac{\omega}{\omega_M}+N^{yx}\right\}\Phi_{n'}^x(\xi)\end{pmatrix} \tag{168}$$

$$\sum_{n'=0}^{\infty}\hat{T}\vec{S}_{n'}(\xi)=\sum_{n'=0}^{\infty}\begin{pmatrix}\left\{-i\frac{\omega}{\omega_M}+N^{xy}\right\}\Phi_{n'}^y(\xi)\\ N^{yy}\Phi_{n'}^y(\xi)\end{pmatrix} \tag{169}$$

The projection over the SWM leads to:

- $\overline{T}^{xx}$

$$\overline{T}^{xx} = \frac{1}{l}\int\limits_{-l/2}^{l/2} \sum_{n=0}^{\infty} \vec{S}_n^x(\xi) \cdot \sum_{n'=0}^{\infty} \begin{pmatrix} N^{xx}\varPhi_{n'}^x(\xi) \\ \left\{ i\frac{\omega}{\omega_M} + N^{yx} \right\} \varPhi_{n'}^x(\xi) \end{pmatrix} d\xi =$$

$$\sum_{n=0}^{\infty}\sum_{n'=0}^{\infty} \frac{1}{l} \int\limits_{-l/2}^{l/2} \left[N^{xx}\varPhi_n^x(\xi)\varPhi_{n'}^x(\xi) \right] d\xi \qquad (170)$$

- $\overline{T}^{xy}$

$$\overline{T}^{xy} = \frac{1}{l}\int\limits_{-l/2}^{l/2} \sum_{n=0}^{\infty} \vec{S}_n^x(\xi) \cdot \sum_{n'=0}^{\infty} \begin{pmatrix} \left\{ -i\frac{\omega}{\omega_M} + N^{xy} \right\} \varPhi_{n'}^y(\xi) \\ N^{yy}\varPhi_{n'}^y(\xi) \end{pmatrix} d\xi =$$

$$\sum_{n=0}^{\infty}\sum_{n'=0}^{\infty} \frac{1}{l} \int\limits_{-l/2}^{l/2} \left[\left(-i\frac{\omega}{\omega_M} + N^{xy} \right) \varPhi_n^x(\xi)\varPhi_{n'}^y(\xi) \right] d\xi$$

$$\overline{T}^{xy} = \sum_{n=0}^{\infty}\sum_{n'=0}^{\infty} \left[\left(-i\frac{\omega}{\omega_M} \right) \frac{1}{l} \int\limits_{-l/2}^{l/2} \varPhi_n^x(\xi)\varPhi_{n'}^y(\xi) d\xi + \frac{1}{l} \int\limits_{-l/2}^{l/2} N^{xy}\varPhi_n^x(\xi)\varPhi_{n'}^y(\xi) d\xi \right] \qquad (171)$$

- $\overline{T}^{yx}$

$$\overline{T}^{yx} = \frac{1}{l}\int\limits_{-l/2}^{l/2} \sum_{n=0}^{\infty} \vec{S}_n^y(\xi) \cdot \sum_{n'=0}^{\infty} \begin{pmatrix} N^{xx}\varPhi_{n'}^x(\xi) \\ \left\{ i\frac{\omega}{\omega_M} + N^{yx} \right\} \varPhi_{n'}^x(\xi) \end{pmatrix} d\xi =$$

$$\sum_{n=0}^{\infty}\sum_{n'=0}^{\infty} \frac{1}{l} \int\limits_{-l/2}^{l/2} \left[\left\{ i\frac{\omega}{\omega_M} + N^{yx} \right\} \varPhi_n^y(\xi)\varPhi_{n'}^x(\xi) \right] d\xi$$

$$\overline{T}^{yx} = \sum_{n=0}^{\infty}\sum_{n'=0}^{\infty} \left[\left(i\frac{\omega}{\omega_M} \right) \frac{1}{l} \int\limits_{-l/2}^{l/2} \varPhi_n^y(\xi)\varPhi_{n'}^x(\xi) d\xi + \frac{1}{l} \int\limits_{-l/2}^{l/2} N^{yx}\varPhi_n^y(\xi)\varPhi_{n'}^x(\xi) d\xi \right] \qquad (172)$$

- $\overline{T}^{yy}$

$$\overline{T}^{yy} = \frac{1}{l}\int\limits_{-l/2}^{l/2} \sum_{n=0}^{\infty} \vec{S}_n^{y}(\xi) \cdot \sum_{n'=0}^{\infty} \begin{pmatrix} \left\{-i\frac{\omega}{\omega_M} + N^{xy}\right\} \Phi^{y}_{n'}(\xi) \\ N^{yy}\Phi^{y}_{n'}(\xi) \end{pmatrix} d\xi =$$

$$\sum_{n=0}^{\infty}\sum_{n'=0}^{\infty} \frac{1}{l}\int\limits_{-l/2}^{l/2} \left[N^{yy}\Phi^{y}_{n}(\xi)\Phi^{y}_{n'}(\xi)\right] d\xi \tag{173}$$

Then $\overline{\hat{T}}$ can be written as

$$\bar{\hat{T}} = \sum_{n=0}^{\infty}\sum_{n'=0}^{\infty} \begin{bmatrix} N^{xx}\delta_{nn'} & -i\frac{\omega}{\omega_M}\bar{T}^{xy*}_{nn'} + \bar{T}^{xy}_{nn'} \\ i\frac{\omega}{\omega_M}\bar{T}^{yx*}_{nn'} + \bar{T}^{yx}_{nn'} & N^{yy}\delta_{nn'} \end{bmatrix} \begin{pmatrix} m^{x}_{n'} \\ m^{y}_{n'} \end{pmatrix} d\xi \tag{174}$$

Where the coefficients $\bar{T}^{pq*}_{nn'}$ and $\bar{T}^{pq}_{nn'}$ are given by

$$\bar{T}^{pq*}_{nn'} = \frac{1}{l}\int\limits_{-l/2}^{l/2} \Phi^{p}_{n}(\xi)\Phi^{q}_{n'}(\xi) d\xi \tag{175}$$

$$\bar{T}^{pq}_{nn'} = \frac{1}{l}\int\limits_{-l/2}^{l/2} N^{pq}\Phi^{p}_{n}(\xi)\Phi^{q}_{n'}(\xi) d\xi \tag{176}$$

3. $\hat{G}(\xi, \xi')$

Applying the operator $\hat{G}$ (equation (68)) to the SWM

$$\sum_{n'=0}^{\infty} \hat{G}\vec{S}^{x}_{n'}(\xi) = \sum_{n'=0}^{\infty} \int\limits_{-l/2}^{l/2} \begin{pmatrix} \left[-AG_P - iBG_Q - \delta(\xi - \xi')Sin^2\theta\right] \Phi^{x}_{n'}(\xi') \\ \left[-CG_P - iDG_Q\right] \Phi^{x}_{n'}(\xi') \end{pmatrix} d\xi' \tag{177}$$

$$\sum_{n'=0}^{\infty} \hat{G}\vec{S}^{y}_{n'}(\xi) = \sum_{n'=0}^{\infty} \int\limits_{-l/2}^{l/2} \begin{pmatrix} \left[-CG_P - iDG_Q\right] \Phi^{y}_{n'}(\xi') \\ -EG_P\Phi^{y}_{n'}(\xi') \end{pmatrix} d\xi' \tag{178}$$

Where the angular dependence is given by

$$A = Cos^2\theta Cos^2\varphi - Sin^2\theta \tag{179}$$

$$B = Sin2\theta Cos\varphi \tag{180}$$

$$C = Cos\theta Sin\varphi Cos\varphi \tag{181}$$

$$D = Sin\theta Sin\varphi \tag{182}$$

$$E = Sin^2\varphi \tag{183}$$

The projection over the SWM leads to:

- $\overline{G}^{xx}$

$$\overline{G}^{xx} = \frac{1}{l}\int\limits_{-l/2}^{l/2}\sum_{n=0}^{\infty}\vec{S}_n^x(\xi)\cdot\sum_{n'=0}^{\infty}\int\limits_{-l/2}^{l/2}\begin{pmatrix}\left[-AG_P - iBG_Q - \delta(\xi-\xi')Sin^2\theta\right]\mathit{\Phi}_{n'}^x(\xi') \\ \left[-CG_P - iDG_Q\right]\mathit{\Phi}_{n'}^x(\xi')\end{pmatrix}d\xi' d\xi =$$

$$\sum_{n=0}^{\infty}\sum_{n'=0}^{\infty}\frac{1}{l}\int\limits_{-l/2}^{l/2}\int\limits_{-l/2}^{l/2}\left(-AG_P - iBG_Q - \delta(\xi-\xi')Sin^2\theta\right)\mathit{\Phi}_n^x(\xi)\mathit{\Phi}_{n'}^x(\xi')d\xi' d\xi \tag{184}$$

- $\overline{G}^{xy}$

$$\overline{G}^{xy} = \frac{1}{l}\int\limits_{-l/2}^{l/2}\sum_{n=0}^{\infty}\vec{S}_n^x(\xi)\cdot\sum_{n'=0}^{\infty}\int\limits_{-l/2}^{l/2}\begin{pmatrix}\left[-CG_P - iDG_Q\right]\mathit{\Phi}_{n'}^y(\xi') \\ -EG_P\mathit{\Phi}_{n'}^y(\xi')\end{pmatrix}d\xi' d\xi =$$

$$\sum_{n=0}^{\infty}\sum_{n'=0}^{\infty}\frac{1}{l}\int\limits_{-l/2}^{l/2}\int\limits_{-l/2}^{l/2}\left(-CG_P - iDG_Q\right)\mathit{\Phi}_n^x(\xi)\mathit{\Phi}_{n'}^y(\xi')d\xi' d\xi \tag{185}$$

- $\overline{G}^{yx}$

$$\overline{G}^{yx} = \frac{1}{l}\int\limits_{-l/2}^{l/2}\sum_{n=0}^{\infty}\vec{S}_n^y(\xi)\cdot\sum_{n'=0}^{\infty}\int\limits_{-l/2}^{l/2}\begin{pmatrix}\left[-AG_P - iBG_Q - \delta(\xi-\xi')Sin^2\theta\right]\mathit{\Phi}_{n'}^x(\xi') \\ \left[-CG_P - iDG_Q\right]\mathit{\Phi}_{n'}^x(\xi')\end{pmatrix}d\xi' d\xi =$$

$$\sum_{n=0}^{\infty}\sum_{n'=0}^{\infty}\frac{1}{l}\int\limits_{-l/2}^{l/2}\int\limits_{-l/2}^{l/2}\left(-CG_P - iDG_Q\right)\mathit{\Phi}_n^y(\xi)\mathit{\Phi}_{n'}^x(\xi')d\xi' d\xi \tag{186}$$

- $\overline{G}^{yy}$

$$\overline{G}^{yx} = \frac{1}{l}\int\limits_{-l/2}^{l/2} \sum_{n=0}^{\infty} \vec{S}_n^y(\xi) \cdot \sum_{n'=0}^{\infty} \int\limits_{-l/2}^{l/2} \begin{pmatrix} \left[-CG_P - iDG_Q\right] \varPhi^y_{n'}(\xi') \\ -EG_P \varPhi^y_{n'}(\xi') \end{pmatrix} d\xi' d\xi =$$

$$\sum_{n=0}^{\infty}\sum_{n'=0}^{\infty} \frac{1}{l} \int\limits_{-l/2}^{l/2}\int\limits_{-l/2}^{l/2} - EG_P \varPhi^y_n(\xi)\varPhi^y_{n'}(\xi') d\xi' d\xi \tag{187}$$

Then $\overline{\hat{G}}$ can be written as

$$\overline{\hat{G}} = \sum_{n=0}^{\infty}\sum_{n'=0}^{\infty} \begin{bmatrix} -AP^{xx}_{nn'} - iBQ^{xx}_{nn'} - Sin^2\theta\delta_{nn'} & -CP^{xy}_{nn'} - iDQ^{xy}_{nn'} \\ -CP^{yx}_{nn'} - iDQ^{yx}_{nn'} & -EP^{yy}_{nn'} \end{bmatrix} \tag{188}$$

Where the coefficients $P^{pq}_{nn'}$ and $Q^{pq}_{nn'}$ are given by

$$P^{pq}_{nn'} = \frac{1}{l}\int\limits_{-l/2}^{l/2}\int\limits_{-l/2}^{l/2} G_P \varPhi^p_n(\xi)\varPhi^q_{n'}(\xi') d\xi' d\xi \tag{189}$$

$$Q^{pq}_{nn'} = -Q^{qp}_{n'n}\frac{1}{l}\int\limits_{-l/2}^{l/2}\int\limits_{-l/2}^{l/2} G_Q \varPhi^p_n(\xi)\varPhi^q_{n'}(\xi') d\xi' d\xi \tag{190}$$

Note that $Q^{xx}_{nn} = 0$.
Now summing the operators in equation (94) one can obtain

$$\sum_{n=0}^{\infty}\left(\hat{D}_{nn}\vec{m}_n + \sum_{n'\neq n}^{\infty} \hat{J}_{nn'}\vec{m}_{n'}\right) = 0$$

Where

$$\hat{D}_{nn} = \begin{bmatrix} R^{xx}_{nn} + \bar{T}^{xx}_{nn} + AP^{xx}_{nn} + Sin^2\theta & -i\left(\frac{\omega}{\omega_M}\bar{T}^{xy*}_{nn} - DQ^{xy}_{nn}\right) + \bar{T}^{xy}_{nn} + CP^{xy}_{nn} \\ i\left(\frac{\omega}{\omega_M}\bar{T}^{yx*}_{nn} + DQ^{yx}_{nn}\right) + \bar{T}^{yx}_{nn} + CP^{yx}_{nn} & R^{yy}_{nn} + \bar{T}^{yy}_{nn} + EP^{yy}_{nn} \end{bmatrix} \tag{191}$$

$$\hat{J}_{nn'} = \begin{bmatrix} R^{xx}_{nn'} + AP^{xx}_{nn'} + iBQ^{xx}_{nn'} & -i\left(\frac{\omega}{\omega_M}\bar{T}^{xy*}_{nn'} - DQ^{xy}_{nn}\right) + \bar{T}^{xy}_{nn'} + CP^{xy}_{nn'} \\ i\left(\frac{\omega}{\omega_M}\bar{T}^{yx*}_{nn'} + DQ^{yx}_{nn'}\right) + \bar{T}^{yx}_{nn'} + CP^{yx}_{nn'} & R^{yy}_{nn'} + EP^{yy}_{nn'} \end{bmatrix} \tag{192}$$

Appendix C: Anisotropy tensor with bulk and surface uniaxial anisotropies

From the anisotropy energy density equations (64, 67), the following expressions can be calculated for their corresponding fields in the $\xi\eta\zeta$ coordinate system.

$$\vec{H}_k = \frac{2K_1 M^{\xi}}{\mu_o M_s^2}\hat{\xi} \tag{193}$$

$$\vec{H}_S = \begin{cases} \frac{2K_S^{top} M^{\xi}(\xi)}{\mu_o M_s^2}\delta(\xi - l/2)\hat{\xi} & \varepsilon = l/2 \\ \frac{2K_S^{bot} M^{\xi}(\xi)}{\mu_o M_s^2}\delta(\xi + l/2))\hat{\xi} & \varepsilon = -l/2 \end{cases} \tag{194}$$

Therefore, in the $\xi\eta\zeta$ coordinate system, the bulk uniaxial anisotropy tensor can be written as

$$\hat{N}_u^{\xi\eta\zeta} = \begin{bmatrix} -\frac{2K_1}{\mu_o M_s^2} & 0 & 0 \\ 0 & 0 & 0 \\ 0 & 0 & 0 \end{bmatrix} \tag{195}$$

Since the surface anisotropy tensor is just defined at the top and bottom surfaces of the film

$$\hat{N}_s^{\xi\eta\zeta} = \frac{2}{\mu_o M_s^2}\begin{bmatrix} -K_S^{top}\delta(\xi - l/2) - K_S^{bot}\delta(\xi + l/2) & 0 & 0 \\ 0 & 0 & 0 \\ 0 & 0 & 0 \end{bmatrix} \tag{196}$$

Now, the C and C^{-1} matrices are used to calculate the anisotropy tensors in the xyz system,

$$\hat{N}_u^{xyz} = C\hat{N}_u^{\xi\eta\zeta}C^{-1} = -\frac{2K_1}{\mu_o M_s^2}\begin{bmatrix} Sin^2\theta & 0 & Sin\theta Cos\theta \\ 0 & 0 & 0 \\ Sin\theta Cos\theta & 0 & Cos^2\theta \end{bmatrix} \tag{197}$$

$$\hat{N}_s^{xyz} = C\hat{N}_s^{\xi\eta\zeta}C^{-1} = -\frac{2}{\mu_o M_s^2}\left(K_S^{top}\delta(\xi - l/2) + K_S^{bot}\delta(\xi + l/2)\right)\begin{bmatrix} Sin^2\theta & 0 & Sin\theta Cos\theta \\ 0 & 0 & 0 \\ Sin\theta Cos\theta & 0 & Cos^2\theta \end{bmatrix} \tag{198}$$

Then, it is clear that the total two dimensional anisotropy tensor have the form

$$\hat{N}_{A,xy} = \begin{bmatrix} N^{xx} & 0 \\ 0 & 0 \end{bmatrix} \tag{199}$$

$$N^{xx} = -Sin^2\theta\frac{2}{\mu_o M_s^2}\left[K_1 + K_S^{top}\delta(\xi - l/2)\delta(\xi' - l/2) + K_S^{bot}\delta(\xi + l/2)\delta(\xi' + l/2)\right] \tag{200}$$

Recalling equation (176) (see Appendix C), it is clear that the only non-zero component is $\bar{T}^{xx}_{nn}$:

$$\bar{T}^{xx}_{nn} = \frac{1}{l}\int\limits_{-l/2}^{l/2} N^{xx}\Phi^{p}_{n}(\xi)\Phi^{q}_{n}(\xi)d\xi \tag{201}$$

$$\bar{T}^{xx}_{00} = -\frac{1}{l}Sin^2\theta\frac{2}{\mu_o M_s^2}\left\{\int\limits_{-l/2}^{l/2} K_u d\xi + \int\limits_{-l/2}^{l/2} K_S^{top}\delta(\xi - l/2)d\xi + \int\limits_{-l/2}^{l/2} K_S^{bot}\delta(\xi + l/2)d\xi\right\} \tag{202}$$

$$\bar{T}^{xx}_{00} = -Sin^2\theta\frac{2}{\mu_o M_s^2}\left[K_u + \frac{K_S}{l}\right] \tag{203}$$

where the sum of the top and bottom anisotropy constants is denoted by

$$K_S^{top} + K_S^{bot} = K_S \tag{204}$$

If $n \neq 0$

$$\begin{aligned}\bar{T}^{xx}_{nn} = &-\frac{1}{l}Sin^2\theta\frac{2}{\mu_o M_s^2}\left\{\int\limits_{-l/2}^{l/2} K_u\left[\sqrt{2}Cos\left(\kappa^p_n(\xi - l/2)\right)\right]^2 d\xi\right\}\\ &-\frac{1}{l}Sin^2\theta\frac{2}{\mu_o M_s^2}\left\{\int\limits_{-l/2}^{l/2} K_S^{top}\delta(\xi - l/2)\left[\sqrt{2}Cos\left(\kappa^p_n(\xi - l/2)\right)\right]^2 d\xi\right\}\\ &-\frac{1}{l}Sin^2\theta\frac{2}{\mu_o M_s^2}\left\{\int\limits_{-l/2}^{l/2} K_S^{bot}\delta(\xi + l/2)\left[\sqrt{2}Cos\left(\kappa^p_n(\xi - l/2)\right)\right]^2 d\xi\right\}\end{aligned} \tag{205}$$

$$\bar{T}^{xx}_{nn} = -Sin^2\theta\frac{2}{\mu_o M_s^2}\left[K_u + 2\frac{K_S}{l}\right] \tag{206}$$

Appendix D: The internal static field and calculation of the R_{nn}^{pp} coefficients

The internal static field is the static field along the $\hat{z}$ direction in Figure 5 and will be given by equation (17):

$$\vec{H}_i = \vec{H}_{ze} + \vec{H}_{Ex} + \vec{H}_{de} + \vec{H}_{Ku} + \vec{H}_{Ks} \tag{207}$$

The Zeeman term is given just by the external applied field $\vec{H}_{ze} = \vec{H}_{ext}$.

There is no exchange static field because of the differential character of the interaction (equation (5)).

The demagnetizing field is just proportional to the component of $\vec{M}_s$ along the perpendicular direction to the film $\vec{H}_{de} = -Cos\theta \vec{M}_s$ (equation (10)).

The static uniaxial bulk anisotropy $\vec{H}_{Ku} = \frac{2K_1 Cos^2\theta}{\mu_o M_s}\hat{z}$ field can be obtained from applying (197) as an anisotropy tensor.

Finally the static uniaxial surface anisotropy field $\vec{H}_{Ks} = \frac{2Cos^2\theta}{\mu_o M_s}\left(K_S^{top}\delta(\xi - l/2) + K_S^{bot}\delta(\xi + l/2)\right)\hat{z}$ can be obtained from applying(198) as another anisotropy tensor. Note this is the only field that depends on ξ.

Now the static internal field and ω_H are both well defined for equations (160, 167). From equation (167) the coefficients for the modes $n = 0$ and $n = 1$ are given by:

$$R_{nn'}^{pp} = \frac{1}{l}\int_{-l/2}^{l/2} \left[\frac{\omega_H}{\omega_M} + \Lambda^2 \left(k_{n'}^{p}\right)^2\right] d\xi \tag{208}$$

$$R_{00}^{pp} = \frac{1}{l}\int_{-l/2}^{l/2} \frac{\omega_H}{\omega_M} d\xi = \frac{1}{M_s}\left[H_{ext} - Cos\theta M_s + \frac{2K_1 Cos^2\theta}{\mu_o M_s} + \frac{2K_S Cos^2\theta}{\mu_o M_s}\right] \tag{209}$$

$$R_{11}^{pp} = \frac{1}{l}\int_{-l/2}^{l/2} \frac{\omega_H}{\omega_M} d\xi = \frac{1}{M_s}\left[H_{ext} - Cos\theta M_s + \frac{2K_1 Cos^2\theta}{\mu_o M_s} + \frac{4K_S Cos^2\theta}{\mu_o M_s l}\right] + \frac{2A\pi^2 n^2}{\mu_o M_s^2 l^2} \tag{210}$$

Therefore for the in-plane configuration $\theta = \frac{\pi}{2}$:

$$R_{00}^{pp} = \frac{1}{l}\int_{-l/2}^{l/2} \frac{\omega_H}{\omega_M} d\xi = \frac{H_{ext}}{M_s} \tag{211}$$

$$R_{11}^{pp} = \frac{1}{l}\int_{-l/2}^{l/2} \frac{\omega_H}{\omega_M} d\xi = \frac{1}{M_s}\left[H_{ext} + \frac{2A\pi^2 n^2}{\mu_o M_s^2 l^2}\right] \tag{212}$$

And for the out-of-plane configuration $\theta = 0$:

$$R_{00}^{pp} = \frac{1}{l}\int\limits_{-l/2}^{l/2} \frac{\omega_H}{\omega_M} d\xi = \frac{1}{M_s}\left[H_{ext} - M_s + \frac{2K_1}{\mu_o M_s} + \frac{2K_S}{\mu_o M_s}\right] \tag{213}$$

$$R_{11}^{pp} = \frac{1}{l}\int\limits_{-l/2}^{l/2} \frac{\omega_H}{\omega_M} d\xi = \frac{1}{M_s}\left[H_{ext} - M_s + \frac{2K_1}{\mu_o M_s} + \frac{4K_S}{\mu_o M_s l}\right] + \frac{2A\pi^2 n^2}{\mu_o M_s^2 l^2} \tag{214}$$

7 References

References

[1] Lara, A., Moreno, J., Guslienko, K. & Aliev, F. Information processing in patterned magnetic nanostructures with edge spin waves. Scientific Reports 7, Article number: 5597 (2017) doi:10.1038/s41598-017-05737-8.

[2] Jamali, M., Kwon J., Seo S., Lee, K. & Yang H. Spin wave nonreciprocity for logic device applications. Scientific Reports 3, Article number: 3160 (2013) doi:10.1038/srep03160.

[3] Che, P., Zhang, Y., Liu, L., Tu, T., Liao, Z., Yu, D., Vetro, F. Ansermet, J., Zhao, W., Bi, L., Yu, H. Short-Wavelength Spin Waves in Yttrium Iron Garnet Micro-Channels on Silicon. Magnetics Letters IEEE, vol. 7, pp. 1-4, 2016, ISSN 1949-307X.

[4] M. Haidar, M. Ranjbar, M. Balinsky, R. K. Dumas, S. Khartsev, and J. Åkerman. Thickness- and temperature-dependent magnetodynamic properties of yttrium iron garnet thin films. Journal of Applied Physics 117 , 17D119 (2015); doi: 10.1063/1.4914363

[5] Hauser C., Richter T., Homonnay N., Eisenschmidt C., Qaid M., Deniz H., Hesse D., Sawicki M., Ebbinghaus S., Schmidt G. Yttrium Iron Garnet Thin Films with Very Low Damping Obtained by Recrystallization of Amorphous Material. Scientific Reports 6, Article number: 20827 (2016) doi:10.1038/srep20827.

[6] Arnold, H. & Elmen, M. Permalloy, an alloy of remarkable magnetic properties. Journal of the Franklin Institute Volume 195, Issue 5, May 1923, Pages 621-632

[7] K. Kobayashi et al.. Damping Constants for Permalloy Single-Crystal Thin Films. In IEEE Transactions on Magnetics, vol. 45, no. 6, pp. 2541-2544, June 2009. doi: 10.1109/TMAG.2009.2018862

[8] Liu, X., Zhang, W. Carter, M., Xiao, G. Ferromagnetic resonance and damping properties of CoFeB thin films as free layers in MgO-based magnetic tunnel junctions. Journal of Applied Physics 110, 033910 (2011)

[9] Bilzer C. , Devolder T., Kim J., Counil G., and Chappert C. Study of the dynamic magnetic properties of soft CoFeB films. Journal of Applied Physics 100, 053903 (2006); https://doi.org/10.1063/1.2337165

[10] O. Gladii, M. Haidar, Y. Henry, M. Kostylev and M. Bailleul. Frequency nonreciprocity of surface spin wave in permalloy thin films. Physical Review B 93 , 054430 (2016)

[11] C. Bilzer. Microwave susceptibility of thin ferromagnetic films:metrology and insight into magnetization dynamics. Condensed Matter [cond-mat]. Université Paris Sud - Paris XI, 2007. English. <tel-00202827>

[12] B. Kalinikos & A. Slavin. 1986. Theory of dipole-exchange spin wave spectrum for ferromagnetic films with mixed exchange boundary conditions. J. Phys. C: Solid State Phys. 19 (1986) 7013-7033.

[13] A. Hubert & R. Schäfer. Magnetic Domains: The Analysis of Magnetic Microstructures. Springer, Berlin, 1998.

[14] C. Kittel. On the Theory of Ferromagnetic Resonance Absorption. Physical Review, 73(2):155-161, Jan 1948.

[15] V. Vlamick. Thèse de doctorat de l'Université Louis Pasteur: Décalage Doppler d'onde de spin induit par un courant électrique. IPCM, 2008.

[16] A.G. Gurevich & G.A. Melkov. Magnetization, Oscillations and Waves. CRC Press, Boca Raton, 1996.

[17] D. Polder (1949) VIII. On the theory of ferromagnetic resonance, The London, Edinburgh, and Dublin Philosophical Magazine and Journal of Science, 40:300, 99-115, DOI: 10.1080/14786444908561215

[18] T. L. Gilbert, "A phenomenological theory of damping in ferromagnetic materials," IEEE Trans. Magn., vol. 40, no. 6, pp. 3443–3449, Nov. 2004

[19] Agilent Technologies, Inc. Application Note 1287-3: Applying Error Correction to Network Analyzer Measurements. Agilent, U.S.A., 2002.

[20] O. Gladii. 2016. Spin Wave Propagation and its modification by electrical current in Py/Al_2O_3, Py/Pt and Fe/MgO films. Université de Strasbourg.

[21] B. Kalinikos, M. Kostylev, N. Kozhus and A. Slavin. 1990. The dipole-exchange spin wave spectrum for anisotropic ferromagnetic films with mixed exchange boundary conditions. J. Phys. C: Solid State Phys. 2 (1990) 9861-9877.

[22] K. Guslienko & A. Slavin. Magnetostatic Green's functions for the description of spin waves in finite rectangular magnetic dots and stripes. Journal of Magnetism and Magnetic Materials 323 (2011) 2418–2424

[23] Bailleul, M. Shielding of the electromagnetic field of a coplanar waveguide by a metal film: Implications for broadband ferromagnetic resonance measurements. Applied Physics Letters 103, 192405 (2013); doi: 10.1063/1.4829367

[24] N.Smith, D. Markham, D. LaTourette. Magnetoresistive measurement of the exchange constant in varied thickness permalloy films. Journal of Applied Physics 65, 4362 (1989); doi: 10.1063/1.343273

[25] M. Maryško, Influence of GGG substrate on FMR and magnetostatic wave propagation, In Journal of Magnetism and Magnetic Materials, Volume 101, Issues 1–3, 1991, Pages 159-161, ISSN 0304-8853, https://doi.org/10.1016/0304-8853(91)90713-K.